# Biomechanical Characterisation of Single-Cell Mechanics and Cell-to-Material Adhesion Using Fluidic Force Microscopy


PhD Student: Ma Luo

Supervisors: Jinju Chen (Lead supervisor)

Jonathan Higgins

# Abstract

The mechanics of living cells are vital for many of their functions, including mechanotransduction, migration, and differentiation, and changes in cell mechanics are related to disease progression. On the other hand, cell-matrix adhesion is important for the patterning, integrity and homeostasis of tissues, and may provide a target for therapy. Cell mechanics and the adhesion between the cells and matrix are also important for tissue engineering. Therefore, it is important to study cell mechanics and cell-to-material adhesion.

Atomic force microscopy (AFM) has been widely adopted for the mechanical characterisation of many cell types. Very recently, fluidic force microscopy has been developed to enable rapid measurements of cell adhesion. However, the simultaneous characterisation of cell-to-material adhesion and the viscoelastic properties of cell is challenging. This study presents a new approach to the simultaneous determination of these properties for single cells, using fluidic force microscopy to investigate cell mechanics and cell-to-material adhesion and the relationship between them.

The new method was initially developed to study MCF-7 cells grown on tissue culture-treated polystyrene surfaces, in which case the flat punch contact model was used. It was found that the adhesive force and adhesion energy for each cell are correlated. Well-spread cells tend to have stronger adhesion, which may be due to the greater area of contact between cellular adhesion receptors and the surface. However, the viscoelastic properties of MCF-7 cells cultured on the same surface appear to have little dependence on cell shape.

This approach was subsequently adapted to examine how polydimethylsiloxane (PDMS) with different levels of stiffness may affect the cell mechanics and cell-material adhesion of MCF-7 cells and the corresponding cells of the healthy MCF-10A cell line. To further study if cell-material adhesion may be correlated with cell migration rate, the wound healing test (scratching

test) and single-cell tracking were performed. It was found that, as the underlying substrate becomes softer, both types of cells exhibit lower adhesion to the substrate and higher migration speeds. For the MCF-7 cells, the modulus decreased and the relaxation time constant increased while for MCF-10A cells these two parameters did not significantly change.

Furthermore, finite element models were developed to examine the reliability of the flat punch contact model in representing the contact between the atomic force microscope's cantilever and the cell. The simulation results have confirmed that the flat punch contact model provides a reasonably good approximation. In addition, finite element models also reveal the effect of underlying substrate and cell morphology on the apparent cell moduli, which can affect the interpretation of experimental results.

# Acknowledgments

Time flies, I have spent 6 years at Newcastle University since the summer of 2016. Looking back on these 6 years of academic study, there are so many people who have helped me, and I would like to express my gratitude to them.

My sincere and hearty thanks and appreciations go firstly to my supervisor Dr Jinju Chen, whose suggestions and encouragement have given me much insight into doctorate research and life. It has been a great privilege and joy to study under her guidance and supervision. I am as well grateful to my second supervisor, Prof. Jonathan Higgins, for providing me with a lot of experimental and theoretical help related to biomedicine and also providing laboratory and consumables. It is my honour to benefit from my supervisors' personality and diligence, which I will treasure my whole life. My gratitude to them knows no bounds.

I would like to thank Dr Jayathilake Pahala Gedara, Dr Guoyu Fu and Jiabo Wang for sharing a lot of knowledge with me about simulation and answering a number of questions I had. And I also acknowledge mathematical support from my groupmate Jack Dawson.

I am appreciated to Dr Mahsa Azizyan, Dr Mark Levasseur, John Exton, Dr Rebecca Harris and Dr Tyrell Cartwright for helping me with experimental and cell-related training and advice, and the help of Dr David Bulmer, Emma Foster, and Dr Alex Laude in the Newcastle University Bioimaging Facility.

I've had the pleasure of working amongst great fellows in my group, Dr Nehir Kandemir, Dr Saikat Jana, Dr Wenjian Yang, Dr Yunyi Cao, Dr Yuqing Xia, Rui Han, Yufeng Zhu and Zeshen Wang.

I would also thank my friends Huagui Zhang, Rixia Zan, Shengqi Yu and Xiaoyan Zhang for enjoying social time during my doctorate life.

Finally, great thanks go to my family for their unfailing love and unwavering support.

# Publications

1. Luo M, Yang W, Cartwright T N, et al. Simultaneous Measurement of Single-Cell Mechanics and Cell-to-Materials Adhesion Using Fluidic Force Microscopy[J]. Langmuir, 2022, 38(2): 620-628.

2. Yang W*, Luo M*, Gao Y, et al. Mechanosensing model of fibroblast cells adhered on a substrate with varying stiffness and thickness[J]. Journal of the Mechanics and Physics of Solids, 2022: 105137.

3. Yang W, Luo M, Gao Y, et al. Computational modelling to predict mechanosensing of fibroblast cells in response to different material properties[J]. 2021.

# Table of contents

# Chapter 1. Introduction

Cancer is the second leading cause of death in the world and was responsible for 8.8 million deaths in 2015. This means that nearly 1 in 6 deaths is due to cancer. There are about 14 million new cases every year, while this number is expected to rise by about 70% over the next two decades. Therefore it is important to develop methodologies that improve the understanding of disease conditions and the progression of cancer[1-3].

Cancer cells are mutant cells that evolve into tumours by interacting with other factors in the microenvironment such as the extracellular matrix and other cells. Unlike normal cells, cancer cells can proliferate indefinitely and destroy normal cell tissues[4]. At present, tumour diagnosis mainly depends on morphological observations at the cellular and tissue levels. However, the morphological characteristics of normal cells and cancer cells are sometimes similar, which leads to the inaccuracy of this method[5].

It has been revealed that the mechanical properties of cells are essential for a wide range of intracellular biological processes associated with cancerous conditions[6-8]. In addition, recent studies at single-cell scale have shown that the migration and invasion of tumour cells are accompanied by changes in cellular mechanical properties such as deformation and adhesion as well as ultramicro-level morphology[9, 10]. The detection of the mechanical properties of single cells has become an important research direction in cell biology, heralding new possibilities for the diagnosis and treatment of cancer. Therefore, cell biomechanics is an emerging discipline with great potential in the study of cancer.

The mechanical properties of cells include their elasticity and viscosity. Changes in cell elasticity can be used to draw inferences concerning changes in the physiological and pathological processes involving cells. The study of

biomechanics is a promising direction because it is closely related to many biological processes such as those relating to disease[11].

The study of the mechanical properties of cells requires sophisticated instrumentation that can capture very small forces and deformations. In recent decades, the use of advanced equipment and techniques such as atomic force microscopy[12-14], magnetic twisting cytometry with the optical detection of bead movements[15, 16], magnetic tweezers[17, 18], optical tweezers[19, 20], microplate rheometers[21, 22] and particle tracking microrheology[23, 24] have made it possible to detect the mechanical responses and properties of cells.

Among these instruments, the atomic force microscope (AFM) is widely used for the mechanical characterization of the elastic and viscoelastic moduli of living cells, including cancerous cell lines[25]. Whole-cell mechanical properties are often measured using spherical probes[25-28], while pyramid probes have been employed for the determination of spatially dependent mechanical properties across the cell[29-32].

In order to accurately determine mechanical properties, it is essential to adopt appropriate mechanical models regarding the testing protocols regardless of which type of probe is used[25]. Otherwise, significant error can be introduced into the measurement; for example, when the effect of loading on the apparent modulus is ignored[26, 33, 34]. In addition, analytical models need to be modified to take into account the effect of large deformations[26, 34, 35].

Tipless AFM cantilevers have been used to measure the adhesion of cells to substrates. In this approach, the cantilever must be functionalized in order to facilitate adhesion which is strong enough for the cell of interest[36, 37]. However, this method is tedious and time-consuming, and it is challenging to ensure that the adhesion between cells and cantilevers is more robust than that between cells and substrates. For instance, during detachment tests, cells might detach from the cantilever as frequently as from the substrate[38].

Another disadvantage is that, in order to achieve the firm adhesion of cells to the cantilever, it needs to be functionalized biologically or chemically; however, this might alter the state of the cells or the integrin distribution and thus generate biased results[39, 40]. Despite the limitations of the measurement of cell-to-substrate adhesion associated with the AFM, the intrinsic relationship between adhesion and the viscoelasticity of cells has not yet been investigated further.
Recently, a new technique of fluid force microscopy (FluidFM) has been developed, where a microfluidic channel is integrated into the cantilever which incorporates the precise force-controlled positioning of the AFM and therefore enables the rapid attachment of probes to cells. The microfluidic channel is linked to a pressure control system, allowing negative pressure to be applied to the cell via the cantilever. When the cantilever retracts, it produces suction on the cell to detach it from the embedded substrate. Force-displacement curves can be recorded during detachment, and thus the adhesive force and adhesion energy can be determined[41-46]. This technique is beneficial for the measurement of strong adhesion between cells and materials.

In a recent study, FluidFM was used to simultaneously determine a single cell's viscoelastic and adhesion properties. However, the method used for the extraction and analysis of the elastic moduli of the cell relies solely on the analysis of the slope in the curve of cantilever loading force[47]. This slope is indeed relevant to the stiffness of cells, but this does not give an accurate analysis of cell modulus. It has been found that different probe loading rates affect the measured Young's modulus of cells and that higher loading rates result in a higher value[48]. Moreover, one of the characteristics of viscoelastic materials is their sensitivity to loading rate. Therefore, viscoelasticity rather than elasticity can better characterize the mechanical properties of cells.

Therefore, this project aims to develop techniques to rapidly simultaneously measure the viscoelastic properties of cells and their adhesion to substrates.

## Aim and objectives of the project

To addresses the challenges highlighted above, the aim of this study is to use FluidFM and appropriate mechanical modelling to simultaneously determine cell viscoelasticity and cell-to-surface adhesion forces and to reveal how those mechanical properties are affected by the stiffness of underlying substrates.

The key objectives of the present research are to:

(1) Develop testing and data analysis protocols to determine the adhesion and viscoelastic parameters of MCF-7 breast cancer cells.

(2) Investigate the effect of stiffness on the mechanical properties of breast cancer cells MCF-7 and the corresponding healthy cells MCF-10a as well as the correlation between cell-material adhesion and cell migration rate.

(3) Develop finite element (FE) models to assess the robustness of the protocols developed in fulfilling objective 1 above. Based on FE simulations, empirical equations are proposed to extract the viscoelastic properties of cells which can eliminate the effect of cell morphology and the underlying substrate.

# Chapter outline

- **Chapter 4**. Simultaneous measurement of single cell mechanics and cell-to-material adhesion using fluidic force microscopy
- **Chapter 5**. Effect of substrate stiffness on cell mechanics
- **Chapter 6**. Finite element (FE) model verification and calibration

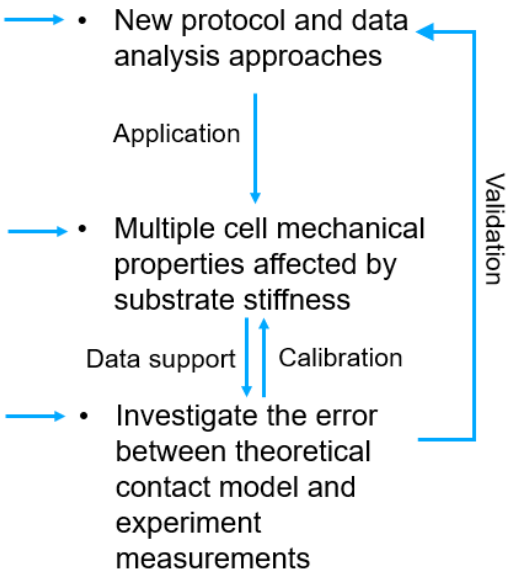

# Chapter 2. Literature Review

The mechanics of living cells are vital for many cell functions, including mechanotransduction[49-51], migration, and differentiation[52]. It is known that changes in cell mechanics are often correlated with disease progression[10, 53-59]. Cell-matrix adhesion is important for the patterning, integrity and homeostasis of tissues, and may provide a target for therapy, for example in cancer metastasis[60]. Cell mechanics and the adhesion between cells and matrix are also important for tissue engineering. Therefore, it is important to study cell mechanics and cell-to-material adhesion.

## 2.1. Mechanical models of the cell

The study of the mechanical properties of cells needs mechanical models. Models proposed so far to explain the mechanics of an individual cell can be divided into two categories of continuum or microstructural models.
Microstructural models include open-cell foams, tensegrity, cable network and integrated cell migration models, among others. Continuum models mainly include two subclasses of elastic/viscoelastic and biphasic models, and the former can be further subdivided into solid, liquid drop, and power-law rheology models.

It is worth noting that the above models have been proposed for one or several aspects of cellular mechanics which are difficult to fully characterize in terms of both functional and structural aspects, and the parameters of a model are dependent on the experimental techniques used. Additionally, since living cells can adapt in a dynamic way to the surrounding environment, there is no single model that can be used to characterize all of the mechanical characteristics of live cells under different circumstances. Therefore, the most feasible

methodology is to choose appropriate models according to the cell line under study and the testing microenvironment[25].

### 2.1.1. Microstructural models

Cells are soft active biological materials, and the cytoskeletal system plays a key role in maintaining the stability of cellular morphology and resistance to external cellular forces[61]. The cytoskeleton consists of a complex network of protein fibres, including actin filaments, microtubules and intermediate filaments which all rapidly undergo polymerization and depolymerization driven by the intracellular environment[62], see Figure 2-1. This process of continuous polymerization and depolymerization can help cells to change their shape and resist external mechanical stimuli[63, 64]. Therefore, the cytoskeleton is key to the mechanical properties of cells, and most microstructural models of cell mechanics are developed based on the cytoskeleton.

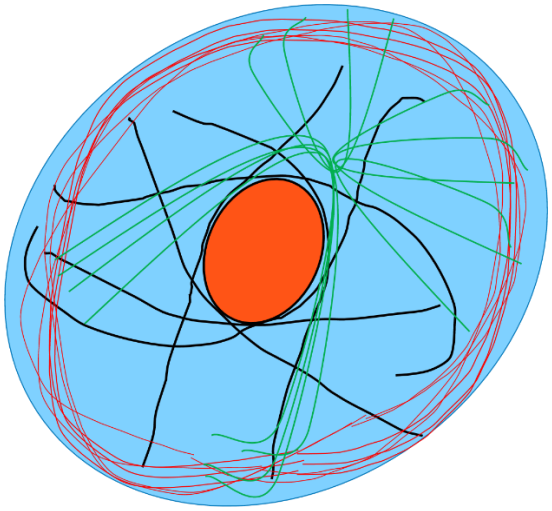

Figure 2-1. Schematic figure of a cell cytoskeleton. The red lines represent actin filaments, which are located in the cortical layer beneath the cell membrane and are associated with cell movement. The black lines represent intermediate filaments, located on the inner side of the nuclear membrane and extending in the cytoplasm of the cell, whose main function is to enhance the mechanical strength and anchoring of the cell. The green lines represent microtubules, which are connected to the centrosome at one end and are associated with organelle positioning, intracellular transport, cell division, etc.

Models of cell mechanics based on the cytoskeleton emphasize its components and the important role of the network structure formed by the cross-linking of the cytoskeleton in resisting external force and producing deformation, such as in open-cell foams, tension integration and cable network models which simplify the complexity of the structure of the cytoskeletal network represented in terms of regular geometry, see Figure 2-2.

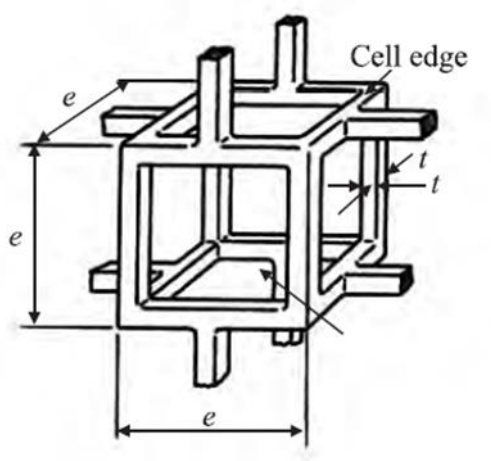


Open-cell Foams Model[65]

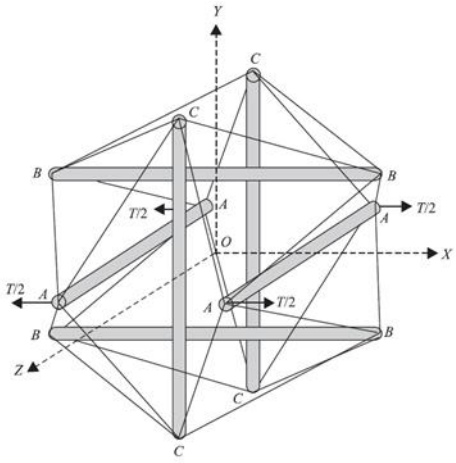


Tensegrity Model[66]

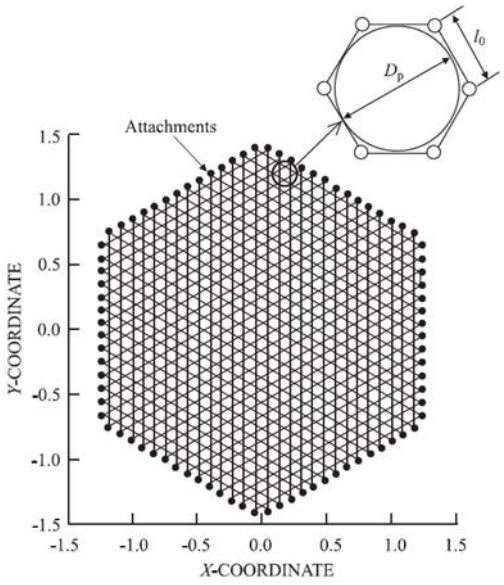


Cable Network Model[67]

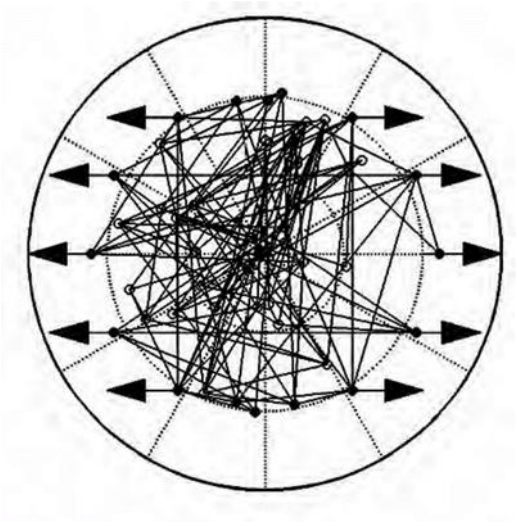

Coarse-grained Model based on Monte Carlo method[68]

Figure 2-2. Different mechanical models of the cell based on the cytoskeleton.

The open-cell foams model predicts that strain hardening during compression is consistent with the strain hardening characteristics of adhesive cells under local pressure. However, the deficiency of this model is that the model is too simple and idealized, and is quite different from the real cytoskeletal structure. Many assumptions are also made in the derivation of the formulae used. In

addition, the viscosity and pre-stressing of the cytoskeleton are not taken into consideration, and so the dependence of cell stiffness on cytoskeletal stress cannot be explained[65].

The concept of tensegrity was first put forward by American architect R. Buckminster Fuller in 1982[69]. In architecture, a tensegrity structure is a self-balanced space system composed of a series of continuous tension bars and discrete compression bars. D.E. Ingber at Harvard University applied this concept to describe the structure of the cytoskeleton. He proposed a tensegrity model in which cellular microfilaments are regarded as tensile components with microtubules as compressive components, and their interaction determines the mechanical properties of the cytoskeleton[66, 70, 71].

The tensegrity model endows the cell model with pre-stressing, which can explain the hardening phenomenon caused by pre-stressing and allows the prediction of the cell's response under external force. However, some size and mechanical parameters in the tensegrity model are not obtained directly from tests, but instead are derived from hypotheses, which prompts doubts about results from the use of the model. In addition, the tensegrity model considers microtubules to be the main compressive components which balance the tension of cell microfilaments, which is still controversial. Recent studies have shown that the importance of microtubules in balancing pre-stressing varies greatly among different types and shapes of cells. Therefore, the tension integration model cannot fully explain the mechanical properties of cells[67].

In the cable network model, the cytoskeleton is simplified as an ideal articulated elastic cable network. The cables in the model represent the microfilaments in the cytoskeleton. It is assumed that the cables are linear elastic, can only bear tension, and are articulated[72].

This model simulates the cell response well using the cell poking test, but the results are quite different from those given by other methods of testing. The model simplifies the cytoskeleton to represent it as a regular network, and treats all of the cables as identical forces. However, the size of real cells in terms of length and radius and mechanical parameters such as modulus of elasticity and the maximum tensile force of the filaments and filament proteins which constitute the network structure of microfilaments vary and should be treated differently. Moreover, the relative density of filaments and filament proteins in cells also directly affect their elastic properties.

In recent years, a coarse-grained model based on the Monte Carlo method and the Brownian dynamics of Taeyoon Kim has been proposed by John Kang *et al*[68]. Here, a regular and fixed topological structure of the cell is no longer assumed, and the model is established by randomly creating filaments. At the same time, more consideration has been given to the microstructure of the cytoskeleton. This makes the models more complex and varied in geometry, which is closer to the real structure of the cytoskeleton.

Kang *et al*. proposed a cellular network model based on coarse-grained Monte Carlo approach to simulate the response of cellular microfilament networks under cyclic stretching. In this model, internal force is generated through the tension of peripheral nodes, and the position of internal nodes and micro-wire stress are determined by equilibrium iteration. The depolymerization and regeneration of microfilaments are then simulated by the substitution of microfilaments. The responses of cells under uniaxial cyclic stretching can thus be effectively simulated. A phenomenon of microfilaments becoming rearranged perpendicular to the direction of stretching was obtained which is consistent with experimental observations.

### 2.1.2.Continuum models

Although cells have heterogeneous internal structures, and the microstructural model represents the mechanical support of the microfilaments and microtubules and intermediate filament skeletons beneath the cell membrane as well as the functioning of the cytoskeleton as a complex network, continuum models have been widely used in many studies. These assume that the cell consists of homogeneous continuities[73], for the following main reasons.

The solution of large-scale microstructural models requires a large amount of computation, which leads to limitations on the size of problems that can be explored. However, continuum models can easily and more straightforwardly predict the mechanical properties of cells at the cellular scale[74]. In addition, a continuum model of the cell can give information about the distribution of stress and strain within the cell. This in turn can be used to determine the stresses (and their distribution) applied to the cytoskeleton and subcellular organelles, hence allowing microstructural models to be developed that take in to account the cytoskeleton and organelles[75].

**Elastic/viscoelastic models**

Elastic/viscoelastic models mainly include solid, liquid drop, and power-law rheology models. A solid model usually assumes that the whole cell is an elastic or viscoelastic solid with no apparent cortex. By not considering the role of the membrane, the solid model greatly reduces the number of mechanical parameters in the model and thus greatly simplifies the analysis of experimental data. In terms of the material model used, solid models of the cell can be divided into linear elastic solid and viscoelastic solid models.

A linear elastic solid model ignores the viscosity of the cell and uses a representation of a simple spring to describe the mechanical properties of the cell. A typical application of this model is in the study of the deformation of endothelial cells in micropipette under negative pressure using the micropipette aspiration technique (MAT)[76]. Although the cell can be approximated as an incompressible linear-elastic half-space when the width of the micropipette's aperture is much smaller than the cell's diameter, in most cases the linear-elastic model is not sufficient to describe the mechanical behaviour of the cell. Li *et al*. from C.T. Lim's team measured the mechanical properties of various breast cancer cell lines by controlling temperature and atomic force microscopy (AFM) loading indentation depth, using the same diameter of spherical tip[56]. They found that, under the same conditions, different loading rates of the probes affected the measured Young's modulus, where the higher the loading rate, the higher the Young's modulus of the cells.

Since one of the characteristics of viscoelastic materials is their sensitivity to loading, the theory of viscoelasticity was introduced into research on the mechanical properties of cells. Viscoelastic solid models take into account both the viscosity and elasticity of cells, and a specific series-parallel pattern between different springs and viscous pots is used to describe cell deformation[77, 78].

The theory of linear viscoelasticity based on the spring viscous pot model was adopted first, since a simple Maxwell or Kelvin model could be used to extract the mechanical parameters representing cell viscosity and elasticity. Based on this, several studies have investigated the relationship between cellular viscoelastic parameters and cell biology[79, 80].

Because the cytoskeleton is composed of a complex network of polymers whose chains vary in length and composition and values of stiffness that vary with length, the local structure of cells composed of such chains will have a

range of different characteristic relaxation times. However, a simple Maxwell or Kelvin model cannot fit experimental data for all relaxation times[81]. Therefore, Prony series models have been developed that achieve a better fit to experimental results and are now widely used[82, 83]. The Maxwell, Kelvin and Prony series models are discussed in detail in Chapter 3.

The liquid drop model can be used to simulate large cell deformations and was first used by Yeung and Evans to simulate the process of cell aspiration into microtubules[84].

This model usually treats a cell as a continuous cortex with solid-like elasticity with a liquid-like core in order to characterize the dual solid-liquid properties of a cell. The cortex has an outward tension which maintains the shape of the cell, and the properties of the core liquid can be characterized in terms of viscosity. Yeung and Evans defined the cell as a highly viscous spherical droplet surrounded by a continuous elastic cortex which has an outward tension. They used micropipette aspiration to measure the apparent viscosity of granular blood cells at $(2.1 \pm 0.1) \times 10^2 Pa \cdot s$ and cortical tension at $0.0035 Pa$. These results are in good agreement with those of previous research, and it was concluded that the cell should be seen as a droplet with a viscous fluid core and an continuous elastic cortex[85].

Solid and droplet models are mainly derived from transient loading conditions. However, real cells are usually subjected to dynamic external forces in a specific physiological environment. In dynamic tests on cells using magnetic tweezer cytometry (MTC) and AFM, there is a weak power relationship between the dynamic storage modulus and the oscillation frequency of adherent cells. The loss modulus shows a similar power relationship at low frequencies and a

significant Newtonian viscosity effect at high frequencies, but this power law dynamic behaviour cannot be described using spring-sticky pot models[86, 87]. Later, Fabry *et al*. proposed that power-law rheology models could describe this rheological behaviour of cells[15], and these models have been used to characterize the dynamic mechanical responses of a wide range of adherent cells[88, 89].

**Biphasic models**

The solid, liquid drop, and power-law rheology models described above all consider cells as single-phase materials. However, the composition of mammalian cells is very complex. The cell membrane forms the interface between the cell and the environment and is composed of lipid bilayer molecules. In addition, cells also contain nuclei, organelles and cytoskeletons suspended or embedded in cytoplasmic fluid, and so the cell contains both solids and liquid-phase fluids.

Based on this, biphasic models treat the cell as a two-phase structure composed of solid-phase and liquid-phase materials. The former are assumed to be linearly elastic whereas the latter are non-viscous and able to diffuse through the solid-phase material. This model has been widely used to study the mechanical properties of musculoskeletal cells, and especially individual chondrocytes and their interaction with the extracellular matrix[90, 91].

However, the biphasic model neglects the fluid barrier role of the cell membrane, and so further adjustments are needed to take its role into consideration.

## 2.2. Finite element analysis and ABAQUS

Finite element analysis (FEA) is a method of numerical analysis, the principles of which are described as follows. The physical laws for space- and time-dependent problems are usually described by partial differential equations (PDEs). For the vast majority of geometries and problems faced, it may not be possible to derive an analytical solution to these partial differential equations. However, it is possible to divide the structure or object under study into a number of cells, and then to extract their characteristics in order to build a set of equations describing each small cell using numerical model equations that approximate these partial differential equations. Boundary conditions are subsequently applied where neighbouring cells share nodes so as to establish connections with other cells. The combination of the equations for all of the small units results in a very large system of joint equations which can be solved numerically to obtain the state of the object under study at a particular step. At this point, the unknowns in the initial set of equations have been changed because the results of the first calculation have been determined, and iteration back to the set of equations gives the state of the object at the next step[92].

In this study, the models developed were built using Abaqus software. Abaqus was developed by the American HSK Company and acquired by the French firm Dassault Systèmes in 2005. It is one of the most advanced large-scale general nonlinear finite element analysis software suites in the world today. The software can perform static and dynamic analyses of complex structures and can handle very large problems such as the simulation of highly nonlinear effects relating to structures and materials. It is easy to use and has high calculation accuracy.

Finite element analysis is widely used in cell mechanics studies to validate and calibrate cell models. The core concept is to use numerical methods to calculate the mechanical responses of a cellular mechanics model under complex conditions such as cellular deformation or the force-displacement curves of nanoindentation. The cellular mechanics responses generated by the models can then be compared with those obtained experimentally from real cells.

By comparing simulation and experiment, on the one hand, finite element simulations can verify the applicability of a theoretical mechanical model of the cell under specific experimental conditions. On the other hand, a series of results can be obtained by running simulations with different parameters, and then an inverse analysis of the parameters of the cellular mechanical model could be achieved by finding the results which most closely match those from experiments.

Ng *et al*. investigated the nanomechanical properties of individual chondrocytes and their pericellular matrix using the AFM and Hertzian contact models[93]. Given the discrepancy between the apparent modulus calculated using a Hertzian model under non-ideal conditions and the actual modulus, an FE model was used for the simulation of experiments for different mechanical parameters. The actual mechanical properties of the cells were then estimated by comparing the force-indentation curves that were closest to the experimental results.

Kang and coworkers used the eight-chain hyperelastic model developed by Arruda and Boyce[94] to analyze the mechanical properties of lung microvascular endothelial cells, taking into consideration the effect of their finite thickness with large cell deformation[95]. By comparing the results of FE simulation and AFM experiments using the Hertzian and eight-chain models, it was found that the latter predicted the mechanical response of endothelial cells

better than the conventional Hertzian model. The accuracy of the eight-chain model was also demonstrated at indentation depths greater than 100 nm.

Nguyen and Gu proposed an experimental method to measure the strength of cell-matrix adhesion[96]. The cartilage attached to the matrix was pushed apart laterally using the AFM cantilever to break the cell-matrix junction, and then the cantilever force curve was employed to quantify the cell-matrix adhesion strength. They used an FE model based on a porohyperelastic mechanical model to simulate the above experimental protocol, and obtained force-displacement curves similar to those from experiments, demonstrating that the PHE model is a useful and accurate model for the simulation of cell adhesion behaviour and can explain intracellular fluid-solid interactions.

In addition, an FEA model allows the mechanical properties of subcellular structures to be calculated inversely without destroying the integrity of living cells.

For example, Caille *et al*. used a hyperelastic FE model with different parameters to simulate the deformation of round and spread endothelium cells with nuclei separated from the cells subjected to compression between glass microplates[38] By comparing the parameters that most closely approximated the force-deformation curves of the cells in experiments, endothelium cells were calculated to have a modulus of 500 Pa for the cytoplasm, 5000 Pa for the nucleus within the cell, and 8000 Pa for the isolated nucleus.

Using a linear elastic FE model, Ofek *et al*. compared published experimental data in simulations of several combinations of cytoplasmic and nuclear Poisson's ratios and found that chondrocytes with a nucleus stiffness of 1.4 times the cytoplasmic value fit the experimental data best[97]. This calculation is significantly lower than the previously reported nucleus-to-cytoplasm stiffness ratio for isolated cells, revealing that when the nucleus is *in situ* it may

behave differently from when isolated. This is consistent with the findings of previous research.

Meanwhile, Chen *et al*. calculated the moduli of the nucleus and cytoplasm of isolated chondrocytes cultured within three-dimensional hydrogels by comparison with experimental data using an FE model of linear elasticity and hyperelasticity[51].

## 2.3. Mechanical characterization of the cell

With progress in the development of biophysical and nanotechnological tools, measurement methods can now mechanically probe cells at piconewton forces and displacement resolutions at nanometre scales, neither of which were previously achievable. Current methods used to measure the mechanical properties of single cells include magnetic tweezers, optical tweezers, single particle tracking, micropipette aspiration, microfluidics and atomic force microscopy.

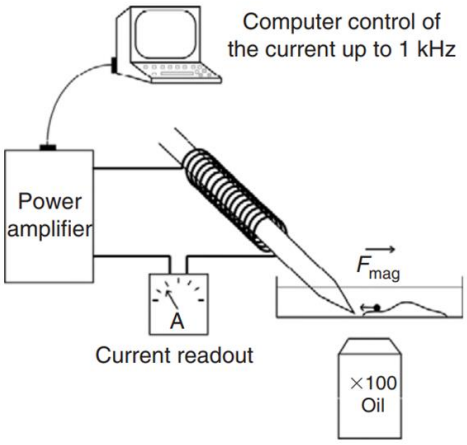


Magnetic tweezers[98]

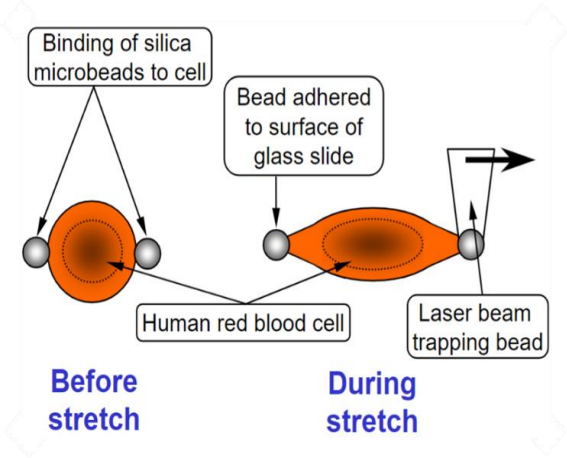


Optical tweezers[99]

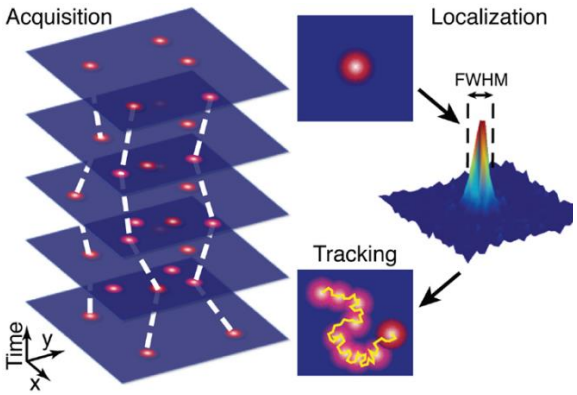


Single particle tracking[100]

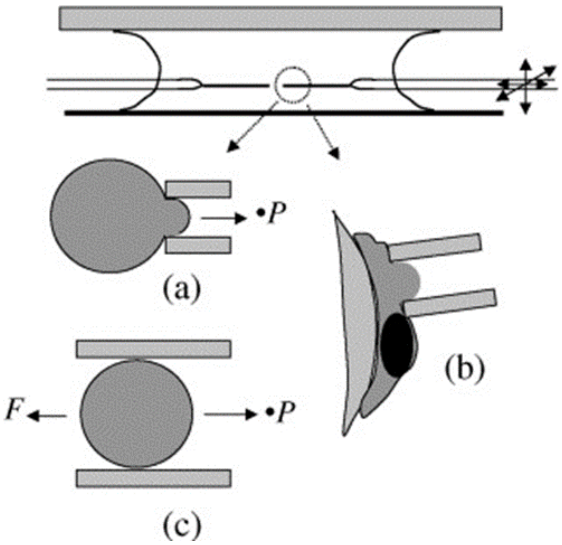


Micropipette aspiration[101]

Figure 2-3. Schematic diagram of widely used techniques for the characterization of the mechanical properties of cells.

### 2.3.1. Magnetic tweezers

Magnetic tweezers are used to analyze the elastic modulus or viscoelasticity of a cell by attaching one or several magnetic beads to the cell surface or allowing them to enter the cell, and then recording the cell deformation and the rotational angular strain and strain rate of the beads in response to the magnetic field of a magnetized coil[98].

Emmanuelle *et al*. characterized the elastic modulus of human alveolar epithelial cells *in vitro*[102]. Meanwhile, Zhang *et al*. coupled magnetic torque cell technology with confocal fluorescence microscopy, which allows for hyper-resolution imaging and the quantitative analysis of structural or physiological changes in the same cell[103].

An advantage of magnetic tweezers over other techniques in measuring the mechanical properties of cells is that magnetic beads within multiple cells can be observed and measured simultaneously, greatly increasing the efficiency of measurement. However, because it is difficult to control the location of magnetic beads, this method is prone to cause the deformation of cell membranes[104].

### 2.3.2. Optical tweezers

Optical tweezers are a device that can produce force to move small transparent objects through a highly focused laser beam, and the order of magnitude is usually of the order of piconewtons. The area holding the object is also called an optical trap, and the corresponding technology is called optical trapping. This technology can be used to move cells or virus particles, pinch cells into shapes, or cool atoms. Because the force of optical tweezers can act directly on cells or even smaller targets, their application in biology has become increasingly extensive[105].

Optical tweezers can be used to manipulate nano- or micron-sized dielectric particles by focusing the force generated by a laser beam. A highly focused laser beam is usually obtained by passing the laser through a microscope's objective lens. There is a very strong electric field gradient in the narrowest part of the focused laser beam, and dielectric particles are attracted to the region with the highest electric field gradient which is at the centre of the beam. At the same time, the electric field also exerts force on the particles in the direction of beam propagation. This can be understood in terms of the conservation of momentum. The dielectric particles in the beam absorb and scatter photons, and corresponding changes in momentum will occur. If the particle is not on the beam waist due to the influence of the light intensity gradient, it will be pulled towards the area of strongest light intensity by uneven force in all directions. Optical tweezers are very accurate devices that can move submicron particles to sub-nanometre distances. Therefore, they are often used to study and manipulate DNA, proteins, enzymes, and even individual molecules[99, 106].

In quantitative scientific measurements, dielectric particles usually do not move far from the centre of the beam. When the distance between the particle and the beam's centre is very small, the force on the particle is proportional to this distance. Therefore, the system's characteristics are similar to those of an ordinary spring system and obey Hooke's law.

### 2.3.3. Single particle tracking

Single particle tracking (SPT) is a powerful tool in microscopy. It allows the movement of a single fluorescent labelled particle (which may be a molecule, vesicle, virus ion or other molecular complex) in culture medium or living cells, and information about its dynamic behaviour over time can be obtained.

Single particle trajectories can help scientists better understand the positions, paths and interactions of molecules in highly dynamic or long-term imaging systems. After data acquisition, an image processing algorithm is used to determine the position of the tracked particles with nanometre-scale accuracy. Trajectories can also be extracted from time series with resolution up to microsecond level.

Single particle tracking method can be also used to measure the mechanical properties of cells. Fluorescent particles are injected into a cell and particle displacement is measured using the fluctuation-dissipation theorem to calculate the mechanical properties of the cell. However, this method can only obtain the mechanical properties of a local area of the cell, and the injection of fluorescent particles may cause changes in cell function and the cytoskeleton[21].

Single particle tracking has been used to study a wide range of biological processes, including the movement of molecules such as proteins or DNA in the cytoplasm and nucleus, of vesicles or virus particles in the cytoplasm or medium, and of lipids and proteins within or across cell compartments, as well as the absorption of external substances such as factors in gene or drug delivery. Single particle trajectories can also reveal structural and functional relationships in complex systems and help in the generation of two-dimensional or three-dimensional location maps of such systems[107, 108].

### 2.3.4. Micropipette aspiration

The micropipette aspiration technique (MAT) is an important research method used to study the deformation and adhesion behaviour of individual cells. When cells are sucked through microtubes, parts of them are drawn into the tubes, changing the value of negative pressure. The amount of cell deformation in the

microtubes can then be obtained, and the relationship between pressure and cell deformation variables is used to determine the elasticity coefficient of cells. The main experimental equipment consists of a glass micropipette, a micro-manipulator and an inverted microscope, with a pressure control system and a CCD camera for data and image recording[109].

The microtubule sucking assay technique was first used by Mitchison *et al*. to study the viscoelastic properties of five types of unfertilized sea urchin oocytes[109]. Sung *et al*. measured cell-cell adhesion force using microtubule aspiration[49] Their method employed the suction pressure of the microtubule to aspirate cells, and when the suction pressure increased to a certain value the cells separated. Due to the relationship between suction pressure and the magnitude of adhesion force between the cells, the value of the latter variable could be obtained by calculation.

The combination of microtubule aspiration techniques with other experimental equipment allows the testing of cellular characteristics under different experimental conditions. For example, in combination with a parallel plate flow chamber, bovine aortic endothelial cells exposed to a stable shear stress environment can be measured[110]. In combination with microfluidics, multiple cells can be measured in parallel. This significantly improves the efficiency of experiments and allows the analysis of the time-varying properties of cellular viscoelasticity, and it is also possible to test for changes in cellular viscoelasticity in the presence of different drugs[111].

### 2.3.5. Atomic force microscopy (AFM)

Since its invention by Binnig *et al*. in 1986, AFM has been used increasingly widely in the detection and processing of micro- and nano-structures. As a tool for the analysis of surface information with high resolution and straightforward sampling requirements, AFM has become a suitable research tool in the field

of micro-nano-processing and biomedical integration. An important application of AFM in tumour detection is to differentiate between tumour and normal cells by measuring their mechanical properties[10, 112], because the process of cell carcinogenesis is often accompanied by changes in structure such as in skeletal protein rearrangement, mechanical properties such as Young's modulus and stiffness, gene expression, and signalling pathways[6]

Compared with magnetic bead distortion and optical tweezers, AFM has the advantages of simple sample preparation, no labelling requirements, and no risk of damage to cells. Therefore, it is the most widely used tool in the measurement of the mechanical properties of single cells[113].

#### 2.3.5.1. Studies of cell elasticity and viscoelasticity based on AFM

AFM can be used to measure the Young's modulus of living cells *in situ*. A sample of the sample is scanned by a tip mounted on an elastic micro cantilever, and a laser beam irradiating the back of the cantilever beam is reflected to a four-quadrant photodetector used to sense the interaction force between the tip and the sample surface. The Young's modulus can then be measured by controlling the tip of the needle to obtain a force curve perpendicular to the surface of the sample[10].

The process of cell carcinogenesis is often accompanied by changes in structure, such as skeletal protein rearrangement, mechanical properties such as Young's modulus and hardness, gene expression, and signalling pathways[8]. An important application of AFM in tumour detection is to differentiate between tumour cells and normal cells by measuring their mechanical properties[10, 112].

In 1999, Lekka *et al*. measured the Young's modulus of Hu456, T24, and BC3726 tumour cells and normal Hu609 and HCV29 human bladder epithelial cells under physiological conditions using AFM[114]. It was found that the Young's modulus of the normal bladder cells at about 10 kPa was about 10 times that of bladder cancer cells (about 1 kPa).

In 2009, Li *et al*. measured the elastic modulus of MCF-7 breast cancer cells and normal MCF-10A breast cells using spherical probes, which also proved that the Young's modulus of the normal cells was larger than that of the cancer cells[115]. It was further found that the Young's modulus of the cells measured increased with probe loading speed but decreased with increasing temperature. These measurements indicate that the Young's modulus of cancer cells is smaller than that of normal cells, and that the Young's modulus of cells can be used to distinguish cancer cells from normal cells. The decrease in Young's modulus may be related to the migration and invasion of cancerous cells.

In 2012, Lekka *et al*. measured Young's modulus of MCF-7 and T47D breast cancer cells, PC-3, LNCaP and Du145 prostate cancer cells, and normal 184A breast cells and PZHPV-7 prostate cancer cells[116]. The moduli of the prostate cancer cells were 1.95±0.47 kPa, 0.45±0.21 kPa, and 1.36±0.42 kPa respectively, while the modulus of elasticity of the normal cells was 3.09±0.84 kPa. Meanwhile, the Young's modulus of the breast cancer and normal breast cells 184A were 1.24±0.46 kPa, 1.20±0.28 kPa, and 2.26±0.56 kPa respectively. The Young's modulus of the cancer cells was also smaller than that of normal cells.

If the viscosity of the cytoplasm is considered, the elastic model does not adequately represent this property of cells. For example, researchers have found that various values of Young's modulus can be obtained for the same

cells, environment and cantilever under different loading rates[48, 115]. Wang *et al*. demonstrated that the Young's modulus of a cell increases as loading rate increases over a certain range, beyond which it tends to maintain a stable value[117].

Hence, the viscoelastic model can be applied to describe the cell's mechanical behaviour, according to which researchers can represent the subcellular structures in investigating the cell and its pathological mechanisms more clearly.

A series of studies of cell viscoelasticity have been conducted by M. Li *et al*. They used AFM to accomplish nanoindentation and analysed the stress relaxation property of cells, and demonstrated that relaxation times can be auxiliary parameters in the identification of healthy and cancer cells[118-120].

#### 2.3.5.2. Studies of cell adhesion based on AFM

The AFM single-cell force spectroscopy (SCFC) technique modifies living cells on probes and can be used to quantify the level of adhesion between cells and various matrices[121]. In 2014, Maciaszek *et al*. used the AFM-SCFS technique to detect the adhesion between human red blood cells and endothelial adhesion proteins[122]. The interaction force between the human erythrocyte and laminin was about 1.03nN due to the adhesion of the laminin to a single human erythrocyte on the probe cantilever and interaction with laminin adhering to the substrate. It was confirmed that cyclic adenosine monophosphate could affect the interaction between human erythrocyte and endothelial adhesion protein, thus facilitating a new method for the development of erythrocyte surface adhesion receptor drugs at the level of a single cell.

Omidvar *et al*. used the AFM-SCFS technique to study the adhesion between cells in three cancerous breast lines (MCF-7, T47D and MDA-MB-231)[123].

The results showed that adhesion between the cancerous cells was significantly reduced, and the Young's modulus decreased according to cytoskeleton reorganization, which may be an important factor leading to the metastasis of cancer cells.

In 2016, Alverto *et al*. adhered MCF-7 cells to a probe tip and observed their interaction with the bacterial cell surface protein SbpA and fibronectin FN-20. The results showed that the interaction force between MCF-7 and SbpA was very weak due to the non-specific binding involved. The dissociation curve of MCF-7 and FN-20 had an obvious adhesion peak, and the adhesion force was about 20nN[124].

The application of SCFS technology based on AFM in cell biology, and especially in tumour detection and treatment, is expanding. If changes in the adhesion behaviour of cancer cells can be measured under drug stimulation, this will be helpful in the development of new methods for the evaluation of the efficacy of anti-tumour drugs[125].

#### 2.3.5.3. Fluidic force microscopy (FluidFM)

The measurement of cell adhesion based on AFM focuses only on pulling the cell away from the surface, but the deformation of the cell cannot be monitored. In this approach, the cantilever must be functionalized in order to facilitate strong enough adhesion to the cell of interest[36, 37]. However, this method is tedious and time-consuming. Furthermore, it is difficult to guarantee that cell-cantilever adhesion is stronger than cell-substrate adhesion. For example, during detachment tests, cells may detach from the cantilever as often as from the substrate[38]. Another disadvantage is that, in order to achieve the firm adhesion of cells to the cantilever, it needs to be functionalized biologically or

chemically which may thus alter the state of the cells or the integrin distribution and provide biased results[39, 40]. Due to the limitations of AFM in the measurement of cell-to-substrate adhesion, the intrinsic relationship between the adhesion and viscoelasticity of cells could not be investigated further using this technique.

More recently, the new technique of fluidic force microscopy (FluidFM) has been developed which enables the rapid attachment of a probe to cells, and this is used in combination with the accurate force-controlled positioning of AFM [41-46]. In this case, a micro-sized channel is integrated into an AFM cantilever and connected via channels in the AFM chip holder, thereby creating a continuous and closed fluidic channel that can be filled with fluid such as deionized water. An aperture in the AFM tip at the end of the cantilever allows liquids to be dispensed locally. Negative pressure can be applied to the cell to attach it to the cantilever, the retraction of which can then detach the cell from the surface (see Figure 2-4). Force feedback is ensured by a standard AFM laser detection system that measures the deflection of the cantilever and the force applied by the tip to the sample during the process of approach and detachment. Force-displacement curves can be recorded during detachment, and therefore the adhesive force and energy can be determined. This technique is particularly useful in the measurement of strong adhesion between cells and materials[46].

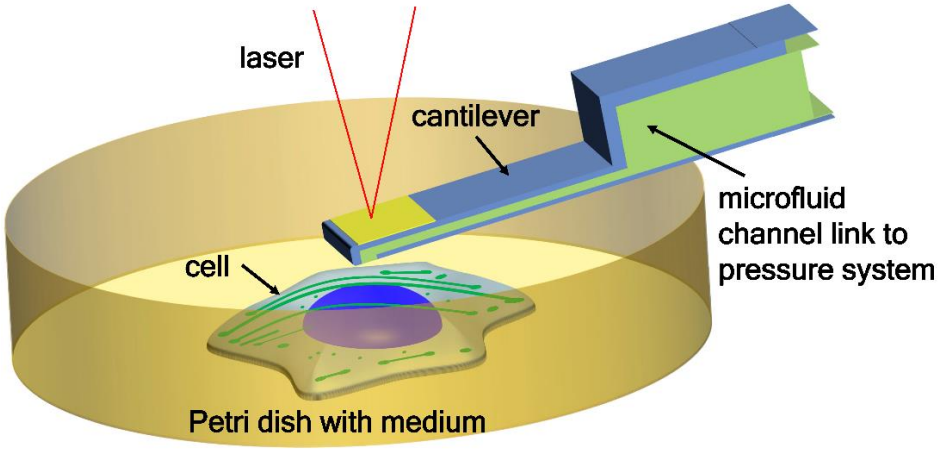


Figure 2-4. Schematic diagram of FluidFM for cell mechanics and cell adhesion measurements. During liquid dispensing, the cell and substrate can be simultaneously observed with an optical microscope, either through the transparent probe holder or the low clearance Petri dish.

This study uses AFM-based FluidFM as the major experimental equipment, and the detailed working principles of AFM and FluidFM are given in Chapter 3.

# Chapter 3. General methodology

## 3.1. Mechanism of AFM

The AFM is different from a conventional optical microscope in having no lenses, light resource, or eyepiece. The core component is a cantilever which has a tip on one side and is fixed on the other side. When the cantilever moves close to or makes contact with the sample surface, the atoms or molecules on the cantilever tip and sample will interact by attractive or repulsive force, and the cantilever can measure these very small forces at pN magnitude; hence the name of the device. The basic principle in the measurement of small interaction force is that the force can be converted into the deflection of the cantilever, which follows Hooke's Law.

Then, the deflection is detected by a laser beam and a detector using the optical lever principle, which can amplify a small change in the bending angle of the cantilever to a measurably large deflection in the position of the reflected spot. Most AFMs use a photodiode that is made of four quadrants, so that the laser spot position can be calculated in two directions. The vertical deflection (measuring the interaction force) can be calculated by comparing the amount of signal from the 'top' and 'bottom' halves of the detector. The lateral twisting of the cantilever can also be calculated by comparing the 'left' and 'right' halves of the detector.

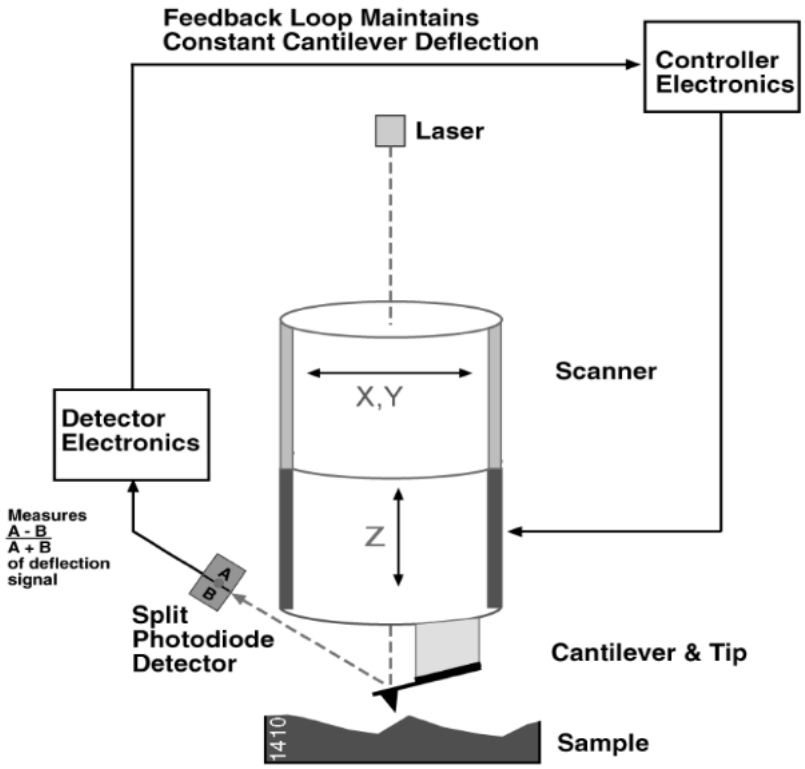


Figure 3-1. Schematic diagram of AFM[126]. First the cantilever contacts the sample and bends slightly in response to the interaction forces. The small bend is then amplified by the movement of the laser reflection point and is recorded by the detector as an electrical signal, which can be further converted into a calculation of the force through the cantilever spring constant and deflection sensitivity. At the same time, the controller sends another set of electrical signals to the piezoelectric ceramic to control the displacement of the cantilever, which is recorded for data analysis. There is also a feedback loop between the detector and the controller to control the cantilever deflection.

Translated with www.DeepL.com/Translator (free version)

The interaction between the sample and cantilever tip leads to a deflection of the cantilever. As the cantilever deflects, the angle of reflection of the laser beam changes, and then the spot of the reflected laser beam falls on a different part of the detector. The detector can compare the difference and calculate the

deflection of the cantilever. Finally, the interaction force between cantilever tip and sample can be obtained according to Hooke's Law if the spring constant of the cantilever is known.

**AFM cantilever spring constant calibration**

The method used to calibrate the spring constant of a cantilever is thermal noise measurement, which is based on simple harmonic oscillator equations as in equation 3.01.

We can obtain the values of $f_0$ and *Q* of the peaks by measuring the thermal noise spectra of the unloaded AFM cantilever and fitting the response of this simple harmonic oscillator with an added white noise floor.

$$A^2(f) = \eta^2 + {A_{DC}}^2 \frac{{f_0}^4}{(f^2 - {f_0}^2)^2 + \frac{{f_0}^2 f^2}{Q^2}} \qquad (3.01)$$

where $A_{DC}$ is the D.C. amplitude, $\eta$ is the white noise background, $f_0$ is the resonance frequency, and *Q* is a quality factor.

Then, using the values of $f_0$ and *Q* obtained for the peaks, the normal spring constant of an AFM cantilever can be determined using the Thermal noise method[127].

When the cantilever is moved, its displacement will also be recorded alongside time and force. By utilizing these data, the AFM can both image the morphology of the sample and analyze its mechanical properties.

The imaging function of the AFM may employ contact, intermit-contact (tapping), or non-contact models.

In experiments, we found that for the same nominal spring constant cantilever, the actual spring constant after correction would vary by up to 50% from the nominal value. For the same cantilever, the calibrated spring constant can also vary by up to 20% each time. Therefore, in this study, we need to eliminate the errors due to each cantilever spring constant calibration.

Firstly, for each experiment the cantilever spring constant was calibrated 100 times and then averaged. Although the values from a single calibration can vary by up to 20%, the calibration values from a large number of repetitions are normally distributed, so that the average of the calibration values is closer to the actual spring constant.

Secondly, two spring constant depended on parameters, the adhesion force and the instantaneous modulus, are combined in a ratio parameter k which eliminates the cantilever spring constant dependence, see Figure 3-2. We found that even though the spring constants varied considerably between cantilevers, after eliminating the spring constant dependence, there were no significant differences in the other parameters under the same conditions. The systematic error caused by the spring constant difference in the calculation can therefore be considered negligible.

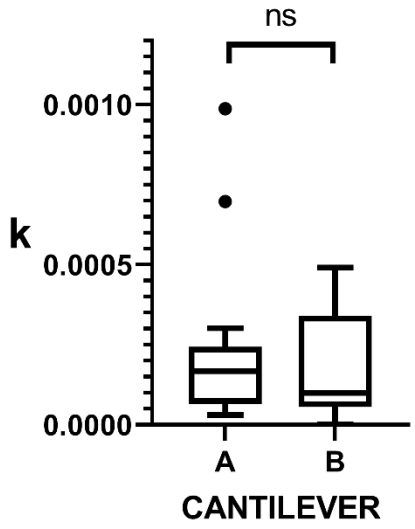


Figure 3-2. Comparation of k for MCF-7 cells on 1:10 PDMS substrates from 2 different cantilevers, and no significant difference was found (p = 0.465).

## 3.2. Analytical models

### 3.2.1. Linear elastic model

The elastic model is the simplest model that has been used, and it regards the cell as an isotropic solid material for which strain is proportional to stress and this ratio is noted as Young's modulus, E:

$$\sigma = E\varepsilon \tag{3.2}$$

This is an instantaneous equilibrium which does not consider the time effect when the cell is under loading, and therefore it cannot describe the cell's mechanical properties sufficiently. However, if the load is applied at a relatively slow or fast speed, then elastic models are reasonable for the analysis of cell mechanics. At relatively small deformation, a simple linear elastic model may be used to find the Young's modulus of the cell. Research shows that this simple elastic model can still contribute to investigations of aspects of cell mechanics such as the stiffness ratio of the nucleus compared to the cytoplasm[97].

When using AFM indentation experimentation to characterize the Young's modulus, E, of cells, probes with various geometries will have different contact models.

When stress-strain equations are converted into force-displacement equations, a parameter called the shear modulus, G, is used. The relationship between the shear modulus G and Young's modulus E is shown in Equation 3.03:

$$E = 2G(1 + v) \tag{3.03}$$

**Flat punch[128]**

$$P = \frac{4GR}{1-\nu}\delta \tag{3.04}$$

where P is the force, R is the radius of the contact area, v is Poisson's ratio, and $\delta$ is the depth of indentation.

In the flat punch contact model, the force is proportional to the depth of compression. The flat punch indenter is a flat bottom cylinder, while in our study, we expand the flat punch into the shape of an irregular flat bottom and replace the bottom surface with a circle of equal area to calculate the effective R. The feasibility of this equivalent replacement will be discussed later.

### 3.2.2. Viscoelastic model

A viscoelastic model can be defined as a combination of spring units and dashpot units, as shown in Figure 3-3. The spring units represent cell elasticity while dashpot units represent cell viscosity.

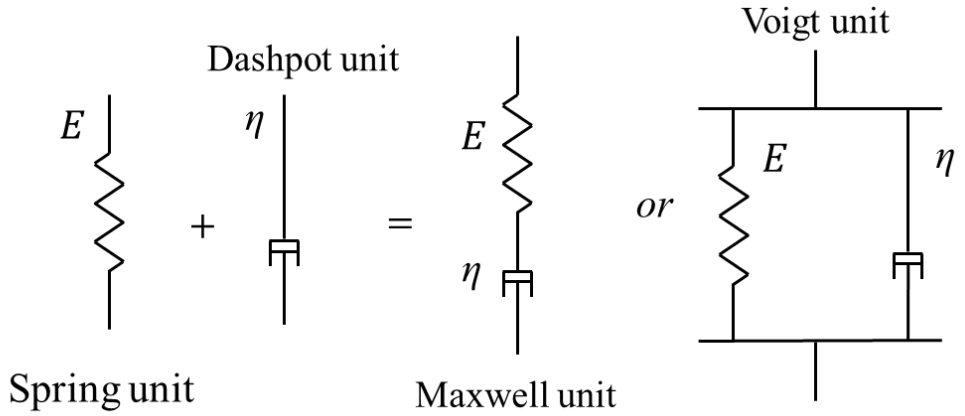


Figure 3-3. Schematics of spring, dashpot and Maxwell unit model obtained with the two basic units in cascade; and the Voigt model obtained with the two basic units in parallel.

For the spring unit,

$$\sigma = E\varepsilon \tag{3.05}$$

and for the dashpot unit,

$$\sigma = \eta \frac{d\varepsilon}{dt} \tag{3.06}$$

where $\sigma$ is the stress, $\varepsilon$ is the strain, E is the elastic modulus of the cell, and $\eta$ is the viscous coefficient.

The analysis of the viscoelastic property is used to characterize the values of the $\eta$ or $E$ parameters for a certain viscoelastic model with a specific configuration of spring and dashpot units. Here we discuss the Maxwell, Voigt and Prony Series models mentioned in Chapter 2.

**Maxwell model**

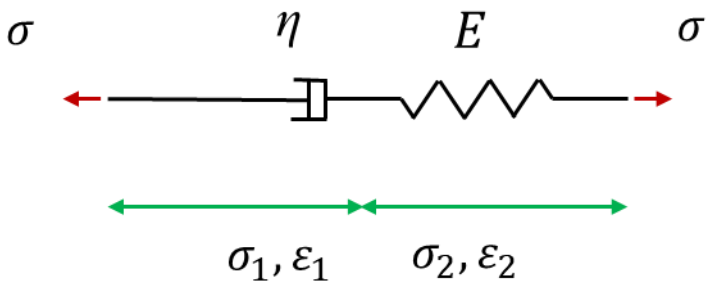


Figure 3-4. Schematic diagram of the Maxwell model

A Maxwell model consists of a spring and a dashpot in series, where $\sigma_1$ and $\varepsilon_1$ are the stress and strain for the spring and $\sigma_2$ and $\varepsilon_2$ are the stress and strain for the dashpot.

Because the spring and the dashpot are connected in series, we have:

$$\sigma = \sigma_1 = \sigma_2 \tag{3.07}$$

$$\varepsilon = \varepsilon_1 + \varepsilon_2 \tag{3.08}$$

Substituting Equations 3.05 and 3.06 into Equations 3.07 and 3.08 gives:

$$\sigma + \frac{\eta}{E}\dot{\sigma} = \eta\dot{\varepsilon} \tag{3.09}$$

For convenience in characterizing the parameters, the stress relaxation and creep behaviour are determined in experiments.

**Stress relaxation**

Stress relaxation occurs when a constant strain is maintained and the resulting stress takes time to react. When a constant strain $\varepsilon_0$ is applied immediately when $t = 0$, and because $\varepsilon = \varepsilon_0,\ \dot{\varepsilon} = 0$, Equation 3.09 becomes:

$$\sigma = -\frac{\eta}{E}\dot{\sigma} \tag{3.10}$$

Solving the differential Equation 3.10, we get:

$$\sigma(t) = \sigma_0 \exp\left(-\frac{t}{\tau}\right) \tag{3.11}$$

Here $\tau$ is the relaxation time, $\tau = \eta/E.\ \sigma_0$ is the instantaneous stress at $t = 0,\ \sigma_0 = E\varepsilon_0$.

**Creep**

Creep is loading a constant stress to the sample, making the react over time. When a constant stress $\sigma_0$ is applied immediately at $t = 0$, and because $\sigma = \sigma_0,\ \dot{\sigma} = 0$, Equation 3.09 becomes:

$$\dot{\varepsilon} = \sigma_0/\eta \tag{3.12}$$

Equation 3.12 shows that the strain increases linearly with time without a limitation. When the stress is removed, the strain of the dashpot will not recover. Therefore, the Maxwell viscoelastic model cannot be used to predict creep behaviour accurately.

**Voigt model**

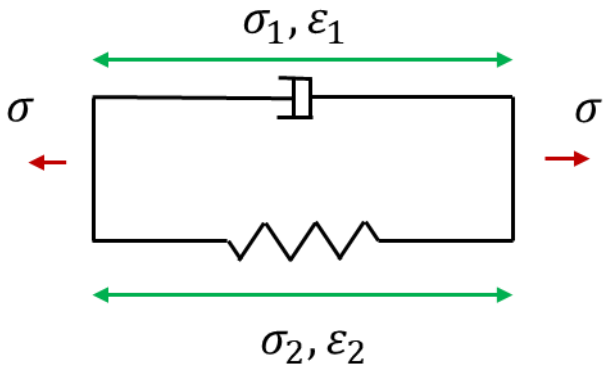


Figure 3-5. Schematic diagram of the Voigt model

A Voigt model consists of a spring and dashpot in parallel, where $\sigma_1$ and $\varepsilon_1$ are the stress and strain for the spring, while $\sigma_2$ and $\varepsilon_2$ are the stress and strain for the dashpot.

Similar to the Maxwell model, we can derive the relationship of $\sigma$ and $\varepsilon$ as follows:

$$\sigma = E\varepsilon + \eta\dot{\varepsilon} \tag{3.13}$$

**Stress relaxation**

$$\sigma = E\varepsilon_0 \tag{3.14}$$

Equation 3.14 indicates that stress relaxation does not take place when the strain applied is constant. Therefore, the Kelvin-Voigt model cannot accurately predict stress relaxation behaviour in a viscoelastic model.

**Creep**

$$\varepsilon = \frac{\sigma_0}{E}(1 - \exp(-t/\tau)) \tag{3.15}$$

In Equations 3.11 and 3.15, $\eta$ and $E$ are displayed in the form of $\tau = \eta/E$. Therefore, in practical characterizations of the viscoelastic property, relaxation times $\tau$ are widely used as a basic parameter to describe the viscoelasticity of a cell.

**Prony series model**

The Prony series model, also known as the general Maxwell model, consists of a spring in parallel with several Maxwell models described in the previous section, as shown in Figure 3-6. Here, the individual springs are called equilibrium arms and the Maxwell models are called Maxwell arms.

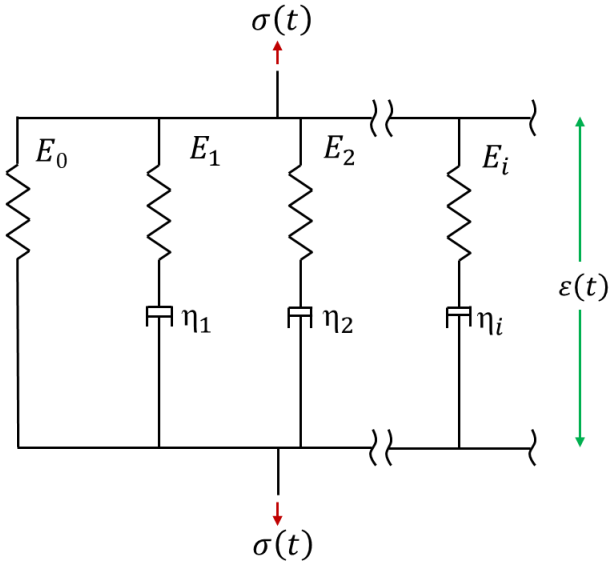


Figure 3-6. Schematic diagram of the Prony series model

In a Prony series,

$$\sigma = \sigma_0 + \sigma_1 + \cdots + \sigma_i \tag{3.2}$$

Substituting Equations 3.11 into Equation 3.2, the relaxation for a step loading at t=0 will be:

$$\sigma(t) = \sigma_0 + \sigma_1 \exp\left(-\frac{t}{\tau_1}\right) + \cdots + \sigma_i \exp\left(-\frac{t}{\tau_i}\right) \qquad (3.21)$$

Most studies have utilized stress relaxation to obtain the viscoelastic properties of the cell by assuming step loading[129, 130]. However, in practice, the loading time in an indentation test is not infinitely small. Therefore, in order to apply the Prony series viscoelastic model to relaxation in the indentation test, we need to derive a stress-strain relationship which takes into consideration a finite loading time of $t_1$, as in the plot of indenter displacement versus time in Figure 3-7.

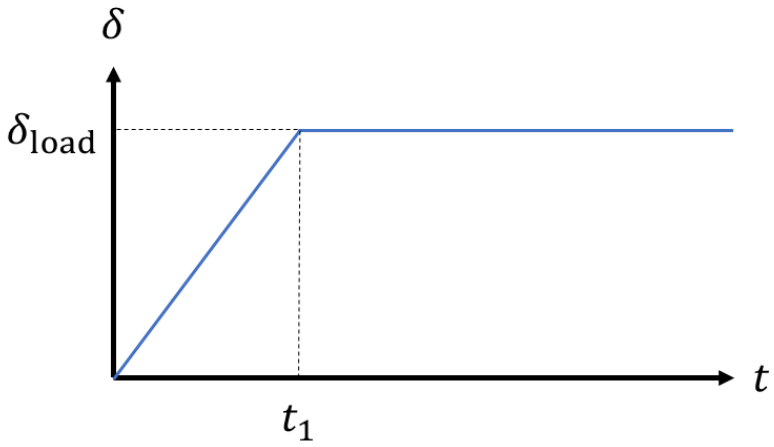


Figure 3-7. Schematic representation of indenter loading over time. During the 0 to $t_1$ period, the indenter is pressed downwards into the sample at a constant rate, and then its position is held constant when the specified depth $\delta_{load}$ is reached.

Considering a finite loading time, the stress and strain of Maxwell arms $i$ will be a function of time, $t$, and Equation 3.09 can be translated as:

$$\frac{d\sigma_i(t)}{dt} + \frac{E_i}{\eta_i} \cdot \sigma_i(t) = E_i \cdot \frac{d\varepsilon(t)}{dt} \qquad (3.22)$$

Multiplication by the integrating factor $e^{\left(E_i t/\eta_i\right)}$ and simplification of the equation gives:

$$\frac{d}{dt}\left(e^{\left(E_i t/\eta_i\right)} \cdot \sigma_i(t)\right) = E_i \cdot e^{\left(E_i t/\eta_i\right)} \cdot \frac{d\varepsilon(t)}{dt} \tag{3.23}$$

Integrating both sides over the interval $[-\infty,\ t']$:

$$\int_{-\infty}^{t'} \frac{d}{dt}\left(e^{\left(E_i t/\eta_i\right)} \cdot \sigma_i(t)\right) dt = \int_{-\infty}^{t'} E_i \cdot e^{\left(E_i t/\eta_i\right)} \cdot \frac{d\varepsilon(t)}{dt} dt \tag{3.24}$$

Solving Equation 3.24:

$$\sigma_i(t') = \int_{-\infty}^{t'} E_i \cdot e^{\left(E_i(t-t')/\eta_i\right)} \cdot \frac{d\varepsilon(t)}{dt} dt \tag{3.25}$$

Substituting Equations 3.05 and 3.25 into Equation 3.2 and changing the notation of $t$ and $t'$ for a better format gives a generalized stress-time equation for a Prony series:

$$\sigma(t) = E \cdot \varepsilon(t) + \sum_{i=0}^{n} \int_{-\infty}^{t} E_i \cdot e^{\left(E_i(t'-t)/\eta_i\right)} \cdot \frac{d\varepsilon(t')}{dt'} dt' \tag{3.26}$$

When using AFM indentation testing to measure the viscoelastic property of cells, as with the methods for the elastic property, it is necessary to use different contact models for different probes in order to transform the stress-strain model into a force-displacement model. In this study, we adopted the principle described by Chen and Lu[26], in which the Prony series viscoelastic model

(Equation 3.26) and flat punch contact model (Equation 3.04) are combined to analyze the stress relaxation curve:

$$F(t) = \frac{2R}{1-v^2} \cdot \left( E \cdot \delta(t) + \sum_{i=0}^{n} \int_{-\infty}^{t} E_i \cdot e^{\left(E_i(t'-t)/\eta_i\right)} \cdot \frac{d\delta(t')}{dt'} dt' \right) \quad (3.27)$$

During the relaxation period, $t_1 < t$, the integral part of Equation 28 can be segmented as $[-\infty, t_1]$ and $[t_1, t]$.

$$F(t) = \frac{2R}{1-v^2} \cdot \left( \begin{array}{l} E \cdot \{\delta(t=-\infty) + \delta(t=0) + \delta(t=t_1)\} \\ + \sum_{i=0}^{n} \left\{ \begin{array}{l} \int_{-\infty}^{0} E_i \cdot e^{\left(E_i(t'-t)/\eta_i\right)} \cdot 0 \, dt' \\ + \int_{0}^{t_1} E_i \cdot e^{\left(E_i(t'-t)/\eta_i\right)} \cdot \frac{\delta_{load}}{t_1} dt' \\ + \int_{t_1}^{t} E_i \cdot e^{\left(E_i(t'-t)/\eta_i\right)} \cdot 0 \, dt' \end{array} \right. \end{array} \right)$$

$$= \frac{2R}{1-v^2} \cdot \left( E \cdot \delta(t=t_1) + \sum_{i=0}^{n} \left\{ 0 + \int_{0}^{t_1} E_i \cdot e^{\left(E_i(t'-t)/\eta_i\right)} \cdot \frac{\delta_{load}}{t_1} dt' + 0 \right\} \right)$$

From the above equation, we obtain the force-time relationship for the flat punch indenter based on the Prony series model during the relaxation period:

$$F(t) = \frac{2R \cdot \delta_{load} \cdot E_{t=0}}{1-v^2} \cdot \left( g_\infty + \sum_{i=0}^{n} g_i \cdot \frac{\tau_i}{t_1} \cdot e^{(-t/\tau_i)} \left\{ e^{(t_1/\tau_i)} - 1 \right\} \right) \quad (3.28)$$

In this study, five parameters are adopted for the Prony series, which consists of 2 Maxwell arms, $i = 2$:

$$F(t) = \frac{2R\delta}{1-v^2} E_0 \left\{ g_\infty + g_1 \frac{\tau_1}{t_1} exp\left(\frac{-t}{\tau_1}\right)\left[exp\left(\frac{t_1}{\tau_1}\right) - 1\right] + g_2 \frac{\tau_2}{t_1} exp\left(\frac{-t}{\tau_2}\right)\left[exp\left(\frac{t_1}{\tau_2}\right) - 1\right]\right\} \quad (3.29)$$

where $g_\infty$ is the normalized equilibrium modulus, $g_i$ is a material-related constant, and $E_0$ is the instantaneous elastic modulus. Living cells like MCF-7 are likely to be essentially incompressible[131], and so we assume that ν = 0.5.

The modulus and viscosity at each Maxwell arm can be determined by:

$$E_i = E_0 g_i \quad (3.3)$$

$$\eta_i = E_i \tau_i \quad (3.31)$$

The equilibrium modulus $E_\infty$, also determined as the Young's modulus of the cell, is given by:

$$E_\infty = E_0 g_\infty \quad (3.32)$$

These models have been demonstrated to describe well the time-dependent behaviour of different cells[132-135].

## 3.3. Viscoelastic properties and adhesion characterization using FluidFM

All experiments for the measurement of cell elasticity/viscoelasticity and cell adhesion forces were performed using the Flex FPM system (Nanosurf, Germany) which combines AFM and FluidFM technology (Cytosurge AG, Switzerland). The system was mounted on an Axio Observer Z1 inverted microscope (Carl Zeiss, Germany) fitted with 20x NA0.4 phase 2 DIC lens and a piezoelectric stage of 100 µm retraction range.

The length and width of FluidFM cantilevers (Cytosurge AG, Switzerland) were 200 µm and 36 µm respectively, with a spring constant of 2 N/m. In general, the choice of cantilever spring constant may affect the determination of relaxation modulus based on finite element modelling and dimensional analysis[136]. A relatively large stiffness constant was chosen in order to accommodate the large adhesive force between cells and the material surface and to enable the true equilibrium modulus to be obtained[136].

The cantilever aperture was 8 µm (as shown in the scanning electron microscope image of the cantilever in Figure S1 in the Supporting Information). Using the Cell Adhesion 100 µm workflow in Cytosurge software, approach-pause-grab operations were carried out for each cell.

Figure 3-8 displays the typical schematic for the cell sucking process. The hollow cantilever approached cells until a set point of 200mV was reached (where force equals 30-50 nN, depending on the different spring constants and deflection sensitivities of cantilevers used). The cantilever was held still for 2-3 seconds because it was found that cantilever vibrations may occur after this time. Then a negative pressure of 800 mbar was applied to the micropipette using the pressure controller in the FluidFM probe to attach the cell to the cantilever, and the piezo stage-cantilever system was then used to retract the cantilever and pull the cell off the surface. Finally, a positive fluid pressure was

applied through the cantilever to release the cell from the cantilever. Only isolated cells were measured so as to avoid cell-cell interactions.

(a) (b) (c) (d)

Figure 3-8. Schematic of cell sucking process using FluidFM: (a) cantilever approaches the cell; (b) end of approach stage, where the cantilever rests on the cell for 2-3 seconds and then negative pressure is applied via the microfluidics system; (c) the cell is moved away from the surface by the cantilever; (d) positive fluid pressure releases the cell.

Cells should be kept in the same environment as the incubator throughout the experiments to maintain cell viability (37°C, 5% CO2, 95% relative humidity). However, the environment chamber was out of order during the experiments, the cells were cooling down to room temperature after they were taken out from the incubator. Therefore, all measurement experiments were performed within two hours of the cells being taken out of the incubator.

Statistical analysis of the data from the first 45 minutes of experimentation and the last 45 minutes of experimentation for MCF-7 cells on 1:10 PDMS substrates showed that the adhesion capacity of the cells decreased with time on average, but this difference was not significant. While the instantaneous and equilibrium modulus kept similar in the two group. See Table 3-1.

Therefore, although the measurement experiment did not maintain the incubator environment, the environmental impact can still be considered as an acceptable level for the data measured within two hours.

Table 3-1. Cell adhesion and moduli difference over time.

| | First 45 minutes n=15 | Last 45 minutes n=18 | *P* value |
|---|---|---|---|
| Adhesive force F (nN) | 72 ± 49 | 48 ± 28 | 0.11 |
| Adhesion energy W (pJ) | 0.58 ± 0.45 | 0.42 ± 0.34 | 0.25 |
| Equilibrium modulus $E_\infty$ (Pa) | 174 ± 78 | 184 ± 130 | 0.66 |
| Instantaneous modulus $E_0$ (kPa) | 2364 ± 780 | 2215 ± 1100 | 0.78 |
| Projected area (μm$^2$) | 586 ± 250 | 655 ± 360 | 0.54 |

### 3.3.1. Characterization of viscoelastic properties

Cells were deformed when the probe reached the set point. In theory, the force-displacement curve during this approach segment can be used to estimate the elastic modulus of the cell. However, the contact area and geometry between the cell and the cantilever was not constant during this period, which meant that was not feasible to calculate the elastic modulus of cell.

During the 3 s pause, the cell exhibited stress relaxation (while the cantilever remained stationary). The pattern of stress relaxation was utilized to obtain a rough estimation of the cell's viscoelastic properties because its contact area remained approximately constant as observed *in situ* and could be estimated through the transparent cantilever (see Figure 3-9).

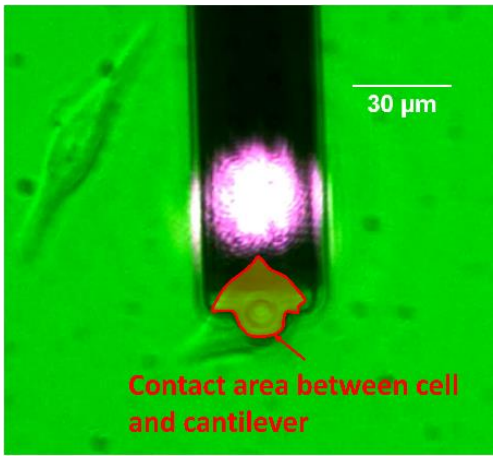


Figure 3-9. Representative image of the contact area between the cell and cantilever.

The displacement of the cantilever and the forces exerted on it were recorded during the process shown in Figure 3-8. A typical force/displacement-time curve for an indentation-pulling test is shown in Figure 3-10.

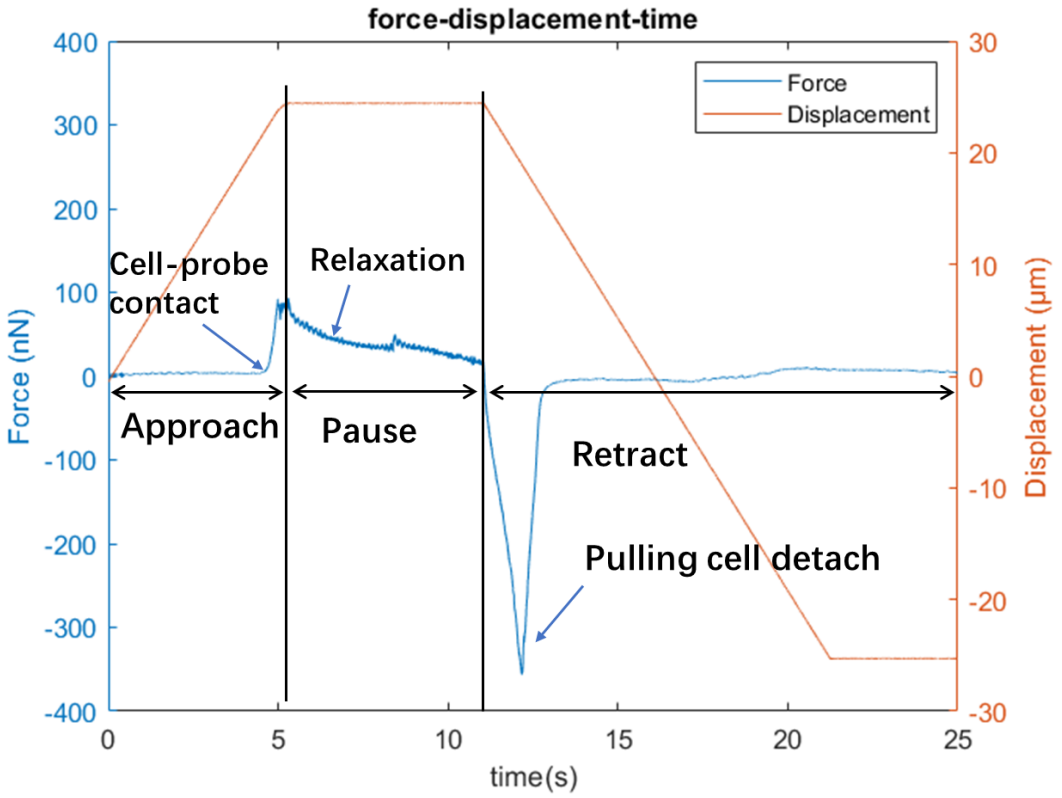


Figure 3-10. Force/displacement-time curves for an indentation-pulling test. The blue curve is the force on the cantilever and the orange curve is the displacement of the cantilever.

In the approach period, the cantilever moves downwards at a fixed rate until it touches the cell and is subjected to an upward force (y-axis in the positive direction) reaching the set point and then stopping, corresponding to Figure 3.7a. The pause period of the cantilever corresponds to Figure 3.7b, where the cell relaxation is recorded. After a pause of a few seconds, negative pressure is applied to the cell through the cantilever, and the cantilever retracts pulling the cell up and separating it from the surface, subjected to a downward force (y-axis in the negative direction). This corresponds to Figure 3.7c.

The stress relaxation curve for the pause period is shown in Figure 3.6. An in-house MATLAB (MathWorks, USA) code was written to perform the curve fitting

based on Equation 3.29, which enabled the determination of $E_0, g_\infty, g_1, g_2, \tau_1,$ and $\tau_2$. In order to avoid the issues caused by cantilever vibration at longer times (3-30s), curve fitting was done for the first 2-3 s of the stress relaxation curve. Then, all of the other viscoelastic parameters can be determined from Equations 3.3-3.32.

### 3.3.2. Characterization of cell-substrate adhesion

A force-displacement graph can be derived from Figure 3-10 by linking force and displacement at the same time point, as in Figure 3-11.

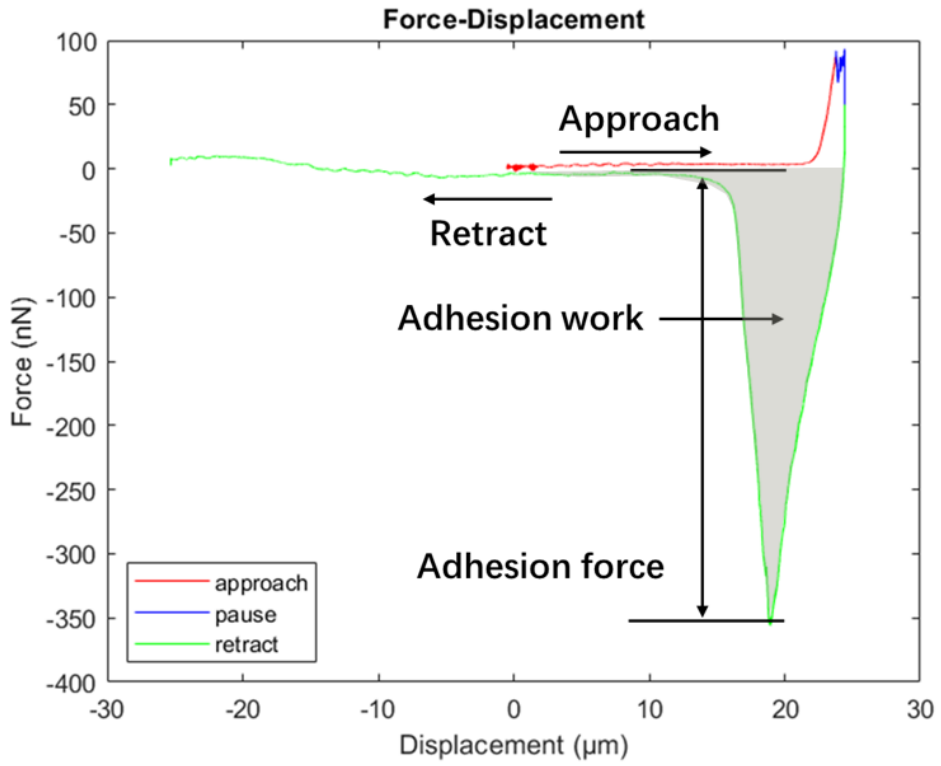


Figure 3-11. Force-displacement curves for an indentation-pulling test. The red curve represents the approach period, the blue curve represents the pause period and the green curve represents the retraction period. The grey area is the adhesion work for the cell detaching from the surface.

Based on the detachment curve, the adhesive force between cell and substrate could be easily determined. The adhesion work for detachment could also be determined by integrating the force-displacement curve during the detachment test.

Therefore, the force-displacement curves obtained during the whole process and the transparency of the cantilever enabled us to simultaneously measure both cell mechanics and cell-to-material adhesion variables.

## 3.4. Confocal imaging

To determine the areas of surface contact, cells were stained with 5 µM CellTracker™ Green BODIPY™ Dye (Thermofisher, UK) for 30 min before imaging. Imaging was performed using a Nikon A1R confocal microscope with a Plan Apo VC 60x Oil, NA1.4, immersion objective. Green BODIPY™ Dye was excited at a wavelength of 522 nm, a 595/50 nm emission filter was applied, and a z-step size of 0.4 µm was used. Using ImageJ (National Institutes of Health, USA) [137], the projection area of each cell was calculated from a manually-thresholded sum intensity projection of the entire z-stack. The contact area of each cell with the substrate was calculated similarly but using only the 5 z-slices nearest to the material surface.

The mechanism of the staining of live cells with CellTracker™ Green BODIPY® and CellTracker™ Orange CMRA was as follows. They did not initially produce a fluorescent signal and could pass through the cell membrane. After entering the cell, the dyes were converted into fluorescent molecules and the new molecules could no longer cross the cell membrane and were therefore retained in the cytoplasm. The cytoplasm's overall shape in the cell can thus be revealed by the fluorescent signal.

The stained living cells were also fixed as long-term samples for future research. A comparison of the 3D structures before and after fixation showed that the fixed samples which can be preserved for long periods of time are morphologically indistinguishable from living cells and are suitable for future study.

To image focal adhesions, cells were fixed for 10 min with 4% paraformaldehyde in phosphate-buffered saline (PBS), washed twice in PBS,

and then permeabilized for 5 min with 0.1% Triton X-100 in PBS (PBS-T). After washing twice in PBS, cells were incubated for 1 h in 5% BSA in PBS-T at room temperature, and then with rabbit anti-Vinculin (Cell Signaling Technology #13901S) and mouse anti-a-tubulin antibodies (Sigma T5168) at 37°C in 5% BSA in PBS-T. After washing twice with PBS-T, the cells were incubated for 1 h with fluorophore-conjugated anti-rabbit IgG Alexa Fluor®488 (Invitrogen A32731), anti-mouse IgG-Alexa Fluor®594 (Invitrogen, A-32744) and Alexa Fluor®647 Phalloidin (to label actin; Cell Signaling Technology #8940S) at 37°C in 5% BSA in PBS-T. After washing twice with PBS-T, and then once with milliQ H2O, samples were mounted using ProLong™ Glass Antifade Mountant with NucBlue® (Invitrogen P36981). Images were captured on an upright Nikon A1+ confocal microscope with Plan Apo 60x Oil IS DIC N2, NA 1.4.

# Chapter 4. Simultaneous measurement of single cell mechanics and cell-to-material adhesion using fluidic force microscopy

## 4.1. Introduction

In previous chapters, the importance of cell mechanics has been introduced. The cytoskeleton is the main source of cell stiffness, and its elasticity can resist the deformation forces caused by extracellular mechanical events impinging upon cells. Force on the cell membrane is sensed by the cytoskeleton, and can upregulate the formation of focal adhesions, altering cell-to-matrix adhesion [138, 139]. Measuring the adhesion and stiffness of the same cell allows characterization of this mechanotransduction mechanism. Viscoelastic cell deformation is often intertwined with cell adhesion during the process of the detachment of cells. Both viscoelastic properties and cell-to-material adhesion play roles in determining how cells migrate in response to mechanical stimuli. The capability to simultaneously determine the viscoelastic properties and adhesion of a single cell can facilitate an understanding of the correlation between these factors and how they collectively affect cell migration. However, this has not been achieved previously because the tipless-cantilever-based technique focuses only on pulling the cell away from the surface, and cell deformation cannot be monitored. Furthermore, the tipless cantilever requires a sufficiently long contact time between the functionalized cantilever and the cell to form a strong bond, which might affect the cell mechanics because the cell is now bonded to two solid surfaces.

Although a recent study used FluidFM in an effort to simultaneously determine the viscoelastic and adhesion properties of a single cell, its method to extract

and analysis elastic moduli was merely based on the analysis of the detachment curve. It was assumed that the slope of the detachment curve reflected cell stiffness[47]. This slope is indeed relevant to the stiffness of cells, but does not give an accurate analysis of cell modulus. It has been found that different probe loading rates affect the measured Young's modulus of cells and that higher loading rates result in a higher modulus[48]. Moreover, one of the characteristics of viscoelastic materials is their sensitivity to loading rate.

Therefore, the use of viscoelasticity rather than elasticity can better characterize the mechanical properties of cells.

In this study, FluidFM was used to simultaneously measure cell viscoelasticity and cell-to-surface adhesion forces, thus allowing a better understanding of the mechanics of cell heterogeneity. The AFM-based FluidFM system sits on a vibration-resistant platform and is enclosed in a bespoke environmental isolation chamber. MCF-7 cells were utilized because they are well-studied human breast cancer cells with abundant biophysical data available for comparison. A better understanding of the mechanical properties of breast cancer cells is also likely to contribute to the design of improved treatments for breast cancer, which has the second highest incidence of all cancers in women worldwide and is the fourth most common cause of cancer mortality[140]. The technique developed here could also be adopted to measure the mechanical properties and adhesion of core/shell particles for use in semiconductors[141], catalysts[142], solar cells[143], drug delivery[144] and biotechnology[145] as well as typical biomaterials like cellulose[146].

Figure 4-1. AFM-based FluidFM system consisting of an AFM, inverted microscope, pressure controller, vibration-resistant platform, and environmental isolation chamber.

## 4.2. Material and methods

The general experimental protocols for FluidFM and confocal fluorescence images and data analysis methods have been described in Chapter 3, and therefore this section restricts itself to elements of the procedures which have not yet been detailed.

### 4.2.1. Cell culture

MCF-7 cells were cultured in DMEM (Dulbecco's Modified Eagle Medium, Sigma Aldrich) with 10% FBS (Fetal Bovine Serum, Sigma Aldrich) and 1% Penicillin-Streptomycin (Thermo Fisher Scientific) in T75 flasks (Thermo Fisher Scientific) at 37°C and 5% $CO_2$ in an incubator at 95% relative humidity. Cells were split when they grew to 80% confluence. For confocal microscopy, nanoindentation and adhesion experiments, cells were seeded and cultured in tissue culture-treated polystyrene Petri dishes (μ-Dish, 50 mm with ibiTreat surface, Ibidi) for 2 days at 37°C, 5% $CO_2$, 95% relative humidity. These dishes enabled cell adherence and proliferation on the surface without additional surface coating. They also have the low clearance required for FluidFM.

### 4.2.2. Cell cycle arrest

The cell cycle is the process of cell division from the completion of one division to the end of the next division, and is divided into the interphase and metaphase. The interphase is divided into the prophase (G1), S phase (S phase) and late phase (G2). MCF-7 cells cultured *in vitro* in the same vessel do not have synchronised cycles, and cell cycle arrest technology allows cells in different phases to be synchronised around a certain point of the cell cycle.

Inhibitors of DNA synthesis reversibly inhibit DNA synthesis without affecting the functioning of cells at other phases, blocking cell populations in the S phase or at the G/S junction. 5-fluorodeoxyuracil, hydroxyurea, cytarabine, aminopterin and high concentrations of thymidine can all inhibit DNA synthesis and be used to synchronize cells[147, 148]. High concentrations of thymidine are less toxic to S-phase cells and are therefore commonly used to induce cell synchronization by TDR double blockade[148], which is also used in this study.

The principle of the use of the double thymidine block to synchronise the cell cycle is shown in Figure 4-2.

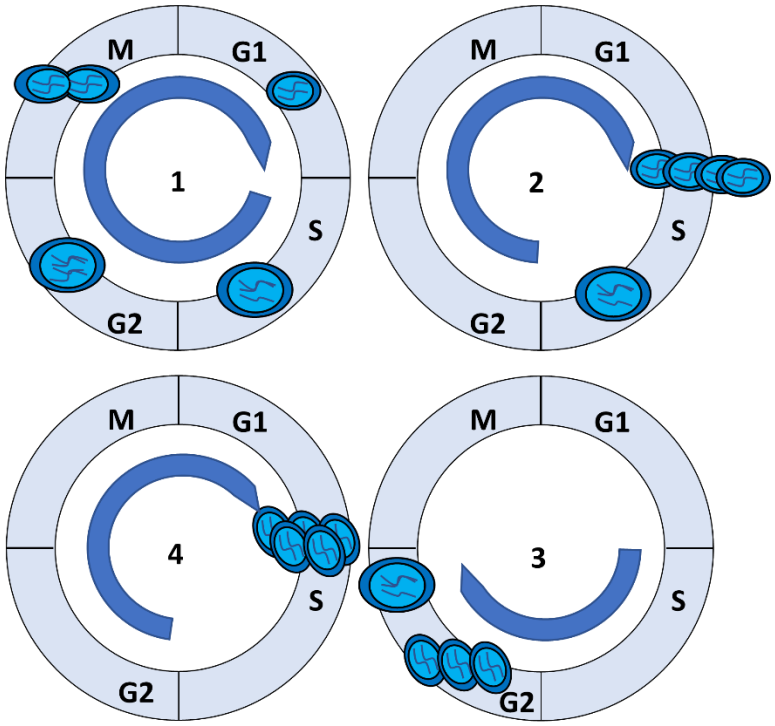


Figure 4-2. Schematic diagram of the double thymidine block principle: 1, cells are randomly distributed in different cycles; 2, after the first addition of high concentrations of thymidine, cells are cultured for at least the G2+M+G1 cell cycle time so as to keep all cells at the G1/S phase junction or in the S phase; 3, cells are released from the first thymidine block and then incubated for slightly longer than the S phase to ensure that all cells come out of the S phase; 4, the second dose of high concentrations of thymidine is added to the culture medium and all cells stay at the G1/S phase boundary.

This method was used to determine the relationship between cell cycle and cell morphology by blocking most cells in S-phase and comparing the changes in the number of well-spread cells observed under the microscope. Then in the experiments, the cell cycle can be determined by observing the cell morphology. Technical details will be described in the following section.

## 4.3. Results and discussion

### 4.3.1. Cell morphology determination

MCF-7 cells plated on tissue culture-treated polystyrene were observed to have different morphologies (for example; round, spindle-like, and spread shapes, as shown in the appendix Figure S 4). Cells with different morphologies were classified in two categories according to their thickness: thicker cells of above 10 μm (mainly round or spindle-like shapes), and flat cells below 10 μm (with a well-spread flying-saucer shape).

Firstly, the 3D morphology of the cells was obtained by analysing confocal microscopy images as described in Chapter 3.4.

Immunofluorescence microscopy revealed that round and spindle-shaped cells had notably fewer detectable focal adhesions containing vinculin than well-spread flat cells (Figure 4-3a). Both the contact area between each cell and the surface (in yellow in Figure 4-3 b and c), and the total projection area for each cell (in green in Figure 4-3 b and c) were determined. The average projection area of thick cells was 430 ± 210 $\mu m^2$, while it was 740 ± 380 $\mu m^2$ for the thinner cells. The average contact areas of the two types were 230 ± 110 $\mu m^2$ and 680 ± 390 $\mu m^2$ respectively. There were significant differences in the projection area ($p = 0.028$) and the contact area ($p = 0.005$) between the two categories of cell. The spreading ratios (the contact area over the projection area) of the thick and thinner cells were 0.55 ± 0.20 and 0.90 ± 0.07 respectively. The difference in spreading ratio was statistically significant ($p = 0.001$).

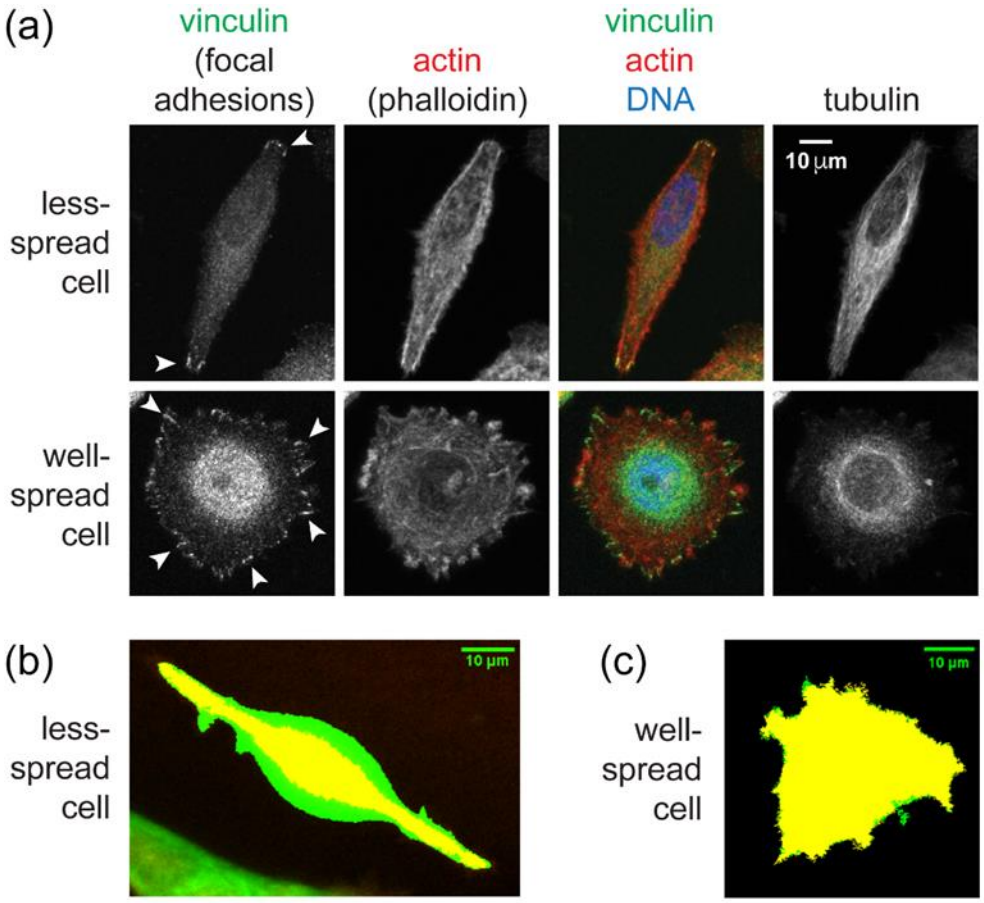


Figure 4-3. Representative confocal images of different MCF-7 cell morphologies: (a) less-spread and well-spread cells were stained for vinculin to reveal focal adhesions (green; some examples indicated with arrows), phalloidin to reveal actin (red), and Hoechst 33342 to show DNA (blue) and a-tubulin (grey); (b) a thick less-spread cell and (c) a thinner well-spread cell stained with CellTracker Green BODIPY™ dye to determine the projection area (green) and contact area (yellow).

In addition, it has been found that the phase of the cell cycle correlates with its morphology and mechanical properties such as modulus and viscosity[149, 150]. The cell cycle arrest method was therefore used to fix the cells in a certain phase to determine if there was a correlation between the cycle and morphology of MCF-7 cells.

After using a double thymidine block to fix the cell in the S phase, PI-stained cells were detected by flow cytometry and then MODFIT software (Roble Ridge Software, USA) was used to analyse the cycle distribution of the cells. The results are shown in Figure 4-4.

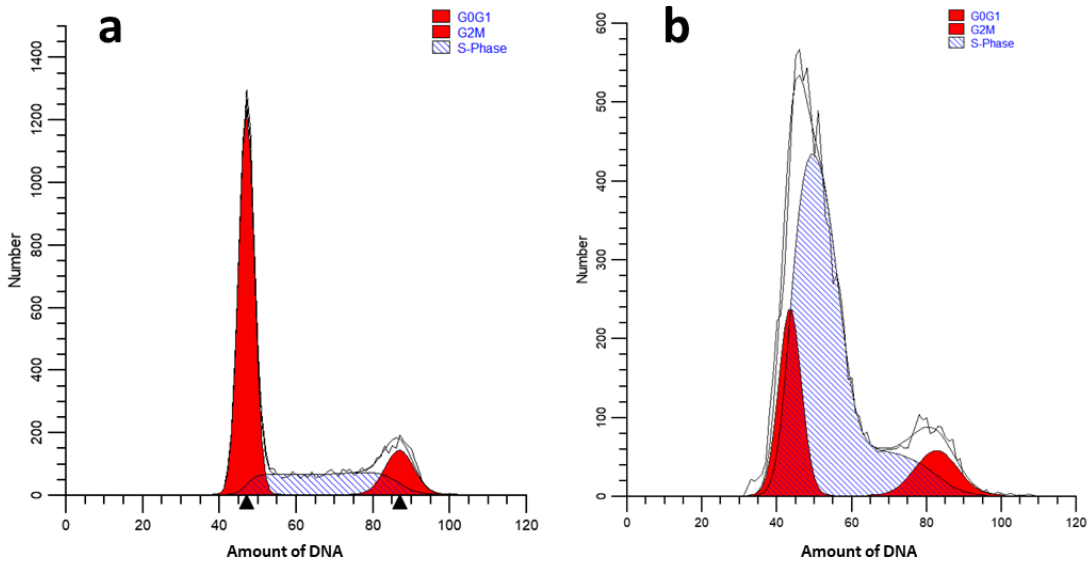


Figure 4-4. Cycle distribution of MCF-7 cells: (a) before and (b) after cell cycle arrest using the double thymidine block method. The first larger red peak refers to the G0/G1 phase and the blue shaded area represents the S phase related to the well-spread cells. The second smaller red peak refers to the G2/M phase of MCF-7 cells related to the less-spread cells.

The DNA of the cells is labelled with PI (Propidium iodide) and can be excited to release red fluorescence. The flow cytometer detects the relative fluorescence intensity of each cell and thus calculates the amount of DNA in the cell. Because the amount of DNA in cells in the G2/M phase is twice as much as in the G1 phase, and the amount of DNA in the S phase is between the G2/M and G1 phases, MODFIT can calculate the number of cells belonging to each cycle by fitting the data.

Cell cycle arrest based on the double thymidine block results in the percentage of S-phase cells increasing from 22-25% to 72-74% and the percentage of M/G2-phase cells decreasing from 10-13% to 7-8%.

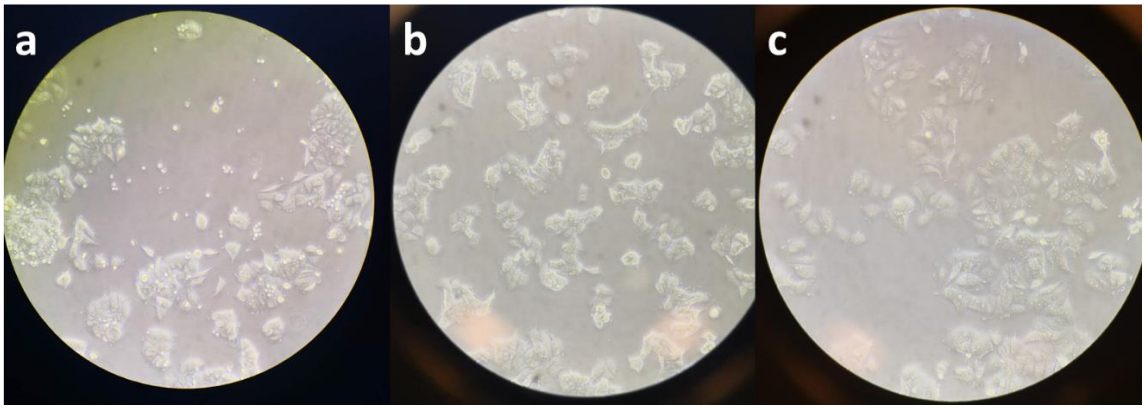


Figure 4-5. Changes in cell morphology observed with a microscope: (a) morphology of cells in the untreated state, with round and spindle-shaped cells visible; (b) morphology of the cells after the first thymidine block, with an increase in cell volume and a decrease in the number of round and spindle-shaped cells; (c) morphology of cells after the second thymidine block with fewer round and spindle shaped cells visible.

By comparing the changes in cell morphology and cell cycle distribution before and after fixation of the cell cycle, the morphological state was correlated with the cell cycle of MCF-7 cells and supplemented the classification of cell morphologies.

In the following sections, thick cells are referred to as less-spread while thinner cells are termed well-spread cells.

### 4.3.2. Simultaneous measurement of cell adhesion and viscoelasticity

The viscoelastic and adhesion properties of 29 less-spread and 18 well-spread MCF-7 cells were then simultaneously determined using FluidFM. Figure 4-6 displays representative force-displacement curves of less-spread and well-spread cells during stress relaxation. The stress relaxation curves were fitted well using Equation 3.29 with R > 0.99 in all cases.

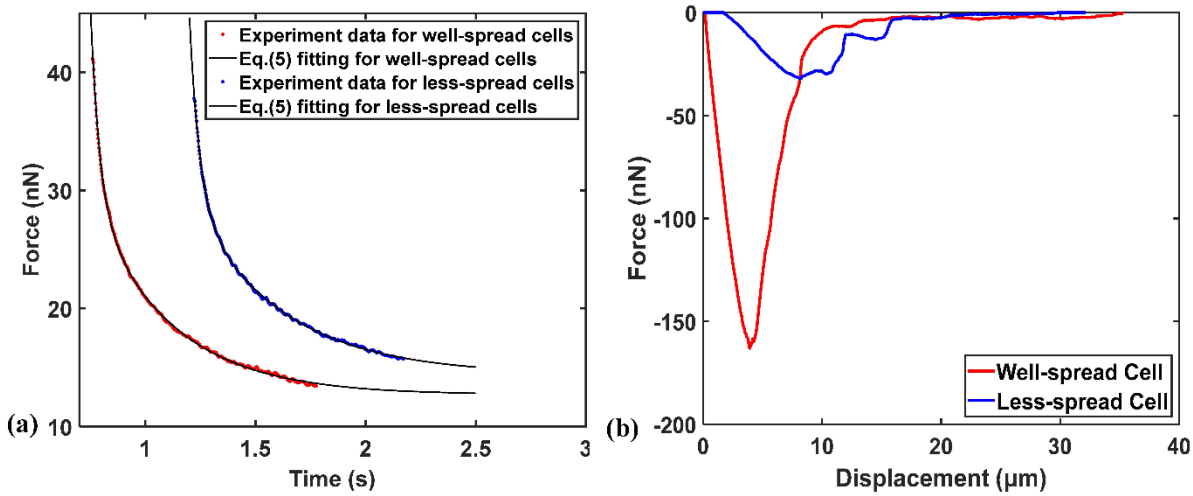


Figure 4-6. Representative curves for: (a) stress relaxation when cantilever is resting on the cell at the end of the approach stage; and (b) the subsequent detachment curves of less-spread and well-spread cells.

Table 4-1 summarizes the key mechanical properties (e.g. viscoelastic properties, the adhesion force and adhesion work) of MCF-7 cells with different spreading ratios. The approach to data analysis used played a very important role here. If cells were assumed to be purely elastic, the mean apparent cell moduli (determined by the loading slope) of the MCF-7 cells were 0.56 kPa and 1.2 kPa for less-spread cells and well-spread cells respectively. In other published work, the Young's moduli of MCF-7 cells were determined by fitting the loading curve with the Hertz model for a spherical probe[80]. However, cells

exhibit viscoelastic characteristics and loading rates are not infinitely small. Therefore, the apparent value determined in this way can dramatically overestimate the Young's modulus[151]. In this study, we only compared the elastic moduli results with those of published studies which adopted appropriate viscoelastic models and considered the effect of the indenter loading rate.

Significant differences between S and W cells for each parameter were analysed using independent t-tests. Levene's Test was first used to test Equality of Variances to determine whether Equal variances were assumed and then the corresponding p-value was selected.

Table 4-1. Summary of key mechanical properties of MCF-7 cells with different spreading ratios.

| | Less-spread cell (n=28) | Well-spread cell (n=19) | *p* value of difference |
|---|---|---|---|
| Instantaneous modulus $E_0$ (kPa) | 1.91 ± 0.71 | 2.12 ± 0.45 | $p = 0.29$ |
| Equilibrium modulus $E_\infty$ (kPa) | 0.21 ± 0.11 | 0.21 ± 0.10 | $p = 0.84$ |
| Time constant $\tau_1$ (s) | 0.10 ± 0.04 | 0.06 ± 0.02 | $p = 0.00044$ |
| Maxwell arm modulus $E_1$ (kPa) | 1.56 ± 0.62 | 1.67 ± 0.47 | $p = 0.57$ |
| Viscosity coefficient $\eta_1$ (Pa·s) | 152 ± 88 | 103 ± 51 | $p = 0.023$ |
| Time constant $\tau_2$ (s) | 0.61 ± 0.27 | 0.55 ± 0.15 | $p = 0.29$ |
| Maxwell arm modulus $E_2$ (kPa) | 0.13 ± 0.06 | 0.24 ± 0.076 | $p = 0.000004$ |
| Viscosity coefficient $\eta_2$ (Pa·s) | 81 ± 48 | 133 ± 50 | $p = 0.0017$ |
| Adhesive force F (nN) | 50.2 ± 40 | 230 ± 290 | $p = 0.0028$ |
| Adhesion energy W (pJ) | 0.37 ± 0.26 | 1.86± 2.9 | $p = 0.057$ |
| Max adhesion force displacement (μm) | 11.45 ± 3.9 | 11.02 ± 7.2 | $p = 0.80$ |
| Full detachment displacement (μm) | 22.14 ± 11 | 20.62 ± 8 | $p = 0.62$ |

#### 4.3.2.1. Viscoelastic properties of MCF-7 cells

Values of equilibrium and instantaneous moduli were obtained of approximately 0.2 kPa and 2 kPa respectively. For well-spread cells, the thin layer effect could be significant at relatively large deformations when using pyramid or spherical indenters[35]. However, in the present study, a flat punch indenter was used and the thin layer effect is not expected to be significant for the thickness/contact radius ratios and indentation depth/thickness ratio relevant here, as is consistent with computational modelling[152-154]. Therefore, a thin layer model similar to that used previously [35] was not considered.

Notably, these moduli were not significantly different between well-spread cells and less-spread cells ($p$ = 0.836 and 0.285 for the equilibrium and instantaneous moduli respectively). The Young's moduli determined here corresponded well with reported values for MCF-7 cells determined using AFM methods and also taking the loading effect into account; for example, Young's (equilibrium) moduli of 0.2-0.5 kPa, [155] and Young's moduli and instantaneous moduli of 0.26 $\pm$ 0.1 kPa and 1.2 $\pm$ 0.4 kPa respectively[151]. The results were also consistent with the Young's moduli (~0.4 kPa) of MCF-7 cells cultured on Petri dishes for 1 day measured using optical tweezers[156], and when utilizing oscillation-induced deformation tests where results between 0.2-0.3 kPa were obtained for MCF-7 cells with different morphologies[157].

The time constants $\tau_1$ and $\tau_2$ reflect the time that cells need to relax after a deformation and are important parameters used to characterize the viscosity properties of cells which are influenced mainly by cytoplasm and actin networks[118, 158]. The difference between values of $\tau_1$ for less-spread and well-spread cells was statistically significant ($p$ = 0.00044), while there was no significant difference in their values of $\tau_2$ ($p$ = 0.29). The maximum time

constants ($\tau_2$) determined here (approximately 0.6 s) were consistent with previously obtained values of 1 s which were based on curve fitting to the results of creep tests using the Kelvin-Voigt model[80]. Values of $\eta_1$ and $\eta_2$ reflect the viscosity of cells and have been defined above in Section 3.2.2. It was found that $\eta_1$ is higher for less-spread cells than well-spread cells, while $\eta_2$ is higher for well-spread cells than less-spread cells. Other studies have shown that $\boldsymbol{\eta_2}$ is often significantly higher than $\eta_1$ [82], as found here for well-spread cells. It has been suggested that the different components of viscosity may be associated with the viscosity of the cytoplasm and cytoskeleton[158]. In this study, overall viscosity (the combination of $\eta_1$ and $\boldsymbol{\eta_2}$) is statistically significantly larger in less-spread than well-spread cells ($p$ = 0.044). This may be attributed to the cytoskeletal organization of less-spread cells. Indeed, it has often been found that round cells (e.g. pre-mitosis) appear to be more viscous compared to well-spread cells in other cell cycle phases[150, 157].

Cell viscosity is important because it can also be a mechanical biomarker for disease progression. For example, Alperen N *et al*. measured mouse ovarian surface epithelial cells using AFM, and found that the viscosity of cells in the early stages of disease progression decreased significantly from $144.7 \pm 100\ \mathrm{Pa \cdot s}$ to $50.74 \pm 30\ \mathrm{Pa \cdot s}$ when reaching the later stages of disease progression[159].

#### 4.3.2.2. Adhesion of MCF-7 to the substrate

The measured adhesion forces of MCF-7 cells on the Petri dish are summarized in Table 1. Previously, it has been found that, for a given type of cell placed on different surfaces, the pulling distance required to detach a cell is longer on surfaces allowing stronger adhesive force. In this case, the work of adhesion was found to be proportional to adhesive force. For example, when cells attached to flat and pillar quartz surfaces, the average adhesion force of cells on the pillar surfaces was found to be half that of the cells on flat surfaces, while the work of adhesion on former surface was about one-third of the latter[160].

Pearson's correlation tests revealed a very strong relationship between adhesion energy and force, with a correlation coefficient = 0.976 ($p$ = 1.8E-29; see Figure 4-7). Meanwhile, there was no correlation between adhesion and the instantaneous or equilibrium moduli, and the correlation between adhesion and viscosity was not statistically significant. However, there was a significant correlation between adhesion force or energy and the viscous modulus (which is a function of the fitting parameter of $g_1$ and $g_2$ as specified in Equation 3.29; $p$ = 0.006 and 0.009 for adhesion force; $p$ = 0.072 and 0.039 for adhesion work). Although there were no significant differences in instantaneous or equilibrium moduli or time constants between less-spread and well-spread MCF-7 cells, the differences between the adhesion force or energy ($p$ = 0.003 and 0.009) and the viscosity coefficients $\eta_1$ and $\eta_2$ were statistically significant ($p$ = 0.023 and 0.0017).

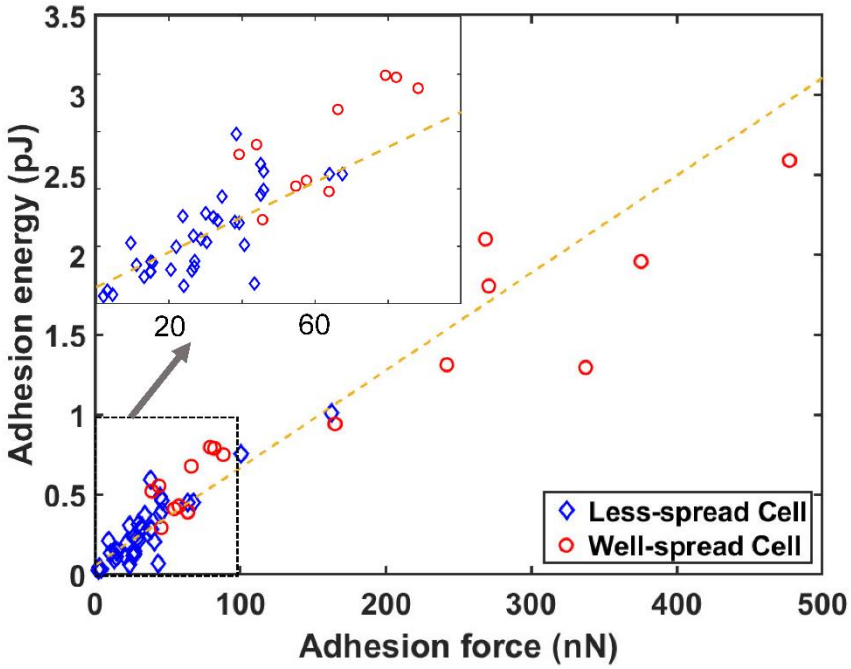


Figure 4-7. Plot of adhesion energy against adhesive force for less-spread cells and well-spread cells. In general, adhesion energy is proportional to adhesive force.

When adhesion energy was plotted against adhesive force, as shown in Figure 4-7, adhesion was found to be proportional to adhesive force for cells of both morphologies. This is consistent with the values of detachment distance presented in Table 1, which were almost the same for less-spread and well-spread cells. For the former, the adhesive force and adhesion energy were weaker compared to their well-spread counterparts. As shown in Table 1, the adhesive force and work of adhesion for less-spread cells were about 5 times less than those for well-spread cells, while the contact areas of less-spread cells were 3 times lower than their well-spread counterparts. This is most likely due to the lower number of cell receptors (integrins, for example) engaged in contact between the cell and substrate[80, 161, 162], which is consistent with the reduced numbers of focal adhesions detected in less-spread cells (see Figure 3.2). Indeed, the overall detachment force is the sum of the cohesive forces of discrete cell receptor-to-surface bonds. In general, based on thermodynamic modelling, the abundance of integrin-ligand bonds is

proportional to the total area of focal adhesions[163, 164], and focal adhesion area often correlates with the area of cell contact with the substrate[165]. Computational modelling also suggests stronger adhesion when focal adhesions are more abundant[166]. Therefore, higher cell contact area is likely to involve higher adhesive force.

In the detachment curves, small drops in force sometimes occurred before the whole cell detached from the surface (see Figure S2), which is probably associated with discrete detachment events prior to whole cell detachment[46]. This may be due to the contraction and detachment of membrane regions containing mature focal adhesions (see Figure S 3 in the appendix). In general, these local detachment forces are of the order of 10 nN, which is similar to the findings of other cell detachment research into mature adhesion states using FluidFM[46]. It should be noted that these forces are 2-3 orders of magnitude higher than those observed for the rupture of the thin cell membrane tethers formed during short-term interactions between cells, or between cells and cantilevers[167, 168].

## 4.4. Conclusions

In summary, this chapter shows that the simultaneous determination of both viscoelastic properties and adhesion of the same cell can be achieved with stress relaxation tests and subsequent pulling tests using fluidic force microscopy. The transparent cantilever enabled us to measure the contact area between cell and cantilever when determining the viscoelastic properties of cells. With appropriate mechanical models that take into account the finite ramping time, we have found that MCF-7 cells on tissue culture-treated polystyrene dishes have Young's moduli of about 0.4 kPa regardless of their spreading ratios. The viscoelastic properties of MCF-7 cells determined here are consistent with findings from AFM nanoindentation using spherical probes.

Although the Young's modulus (equilibrium elastic modulus) and instantaneous elastic modulus were found to be independent of cell shape on the same surface, the viscosity of cells was to a small extent dependent on cell shape. The adhesive force and energy were strongly correlated with the cell spreading ratio. This suggests that even fairly extensive differences in the morphology of cells and their cytoskeletons do not necessarily have a major effect on their elastic properties if the cells are attached to the same surface.

This experimental method and analytical approach could represent a powerful tool for the establishment of quantitative correlations among different physical characteristics of numerous cell types in normal or diseased states, as well as in elucidating the underpinning biological and pathological implications.

This unique capability to measure viscoelastic properties and the adhesion to a material of a single cell is important for the understanding of cell heterogeneity. We have also demonstrated that pulling tests using fluidic force microscopy can detect multiple discrete events that may be associated with the detachment of distinct focal adhesion-containing structures.

# Chapter 5. Effect of substrate stiffness on cell mechanics

## 5.1. Introduction

As mentioned previously in Chapter 4, cell stiffness, viscoelasticity and adhesion to the substrate are correlated and are strongly linked to the cytoskeleton. Meanwhile, numerous studies have shown that the characteristics of a cell's external environment affect its mechanical properties. Cells can also sense the mechanical properties of the external environment, such as the stiffness of the substrate on which they are growing, and are able to change accordingly.

In previous work on the physical measurement of cell mechanics it has been found that the commonly used tipless cantilever cannot generate a strong adhesive force between the cell and the cantilever. Other methods use the chemical functionalization of the cantilever tip, but its chemical composition will alter the cell's mechanical properties, resulting in confusion about the cause of changes in cell mechanics. To directly and simultaneously measure the mechanical properties of cells, including viscoelasticity and adhesion, the new FluidFM technology offers a promising tool for these studies. This could help in the development of a better understanding of how cells change their viscoelastic properties and cell-material adhesion in response to substrates of different stiffness, and what role these responses play in determining how cells change their ability to migrate. It could also help in understanding how these variables are interrelated and how they combine to affect cell migration.

Polydimethylsiloxane (PDMS) has features of chemical stability, low biotoxicity, and physiological inertness, and so it is used in a wide range of medical devices

and materials such as breast implants and catheters[169-171]. It also has good light transmission, and its stiffness is simple to control. Therefore, PDMS was chosen in this study as the substrate material for cell growth. However, the surface energy of directly-cured PDMS is relatively low and the substance is highly hydrophobic, which affects its polar interactions with cell membrane proteins (for example, in hydrogen bonding) and thus it is not conducive to adherent cell growth. Therefore, a hydrophilic modification of the PDMS surface is required to make it more suitable as a substrate material for cell growth.

The wound healing test is a simple method used to determine the movement of cells. It also known as the scratching test because it measures cell migration by scratching a monolayer of cells and then periodically capturing images with a time-lapse microscope to observe the extent to which the gap narrows. There are many advantages to the scratching test. For example, it is relatively inexpensive and simple to operate and allows for real-time measurements. In addition, it can be easily adapted to different test conditions. However, a major limitation is that it is difficult to control the width of the manual scratch and maintain a consistent size, and various factors can affect the measurement results such as the aggregation of cells at the edge of the scratch. Not only that, but scratching can easily damage the surface structure of the substrate if the force used is too high, whereas insufficient force may not remove the cells from the scratched area (see Appendix, Figure S1)

Because the scratching test has many interfering factors, single cell tracing was used to gather the raw data for the cell migration analysis in this research. The experimental procedure employed is similar to that of the scratch assay, except that a lower confluence of cells is cultured on the surface of the PDMS and the ability of the cells to move is then measured by tracking the movement trajectory of each cell rather than assessing the overall recovery of the scratch.

Based on the method developed in Chapter 4, the work reported below simultaneously measures the adhesion and viscoelasticity of MCF-7 cells and MCF-10A cells grown on PDMS with different levels of stiffness using FluidFM. In addition to the characterization of cell adhesion and its relationship with viscoelasticity in the study of the mechanisms of mechanotransduction, the sensing by and responses of cells to aspects of their external environment so as to alter their mechanical properties and migration ability were also investigated, focusing in this case on the stiffness of the surface on which they are grown.

## 5.2. Material and methods

The general experimental protocols for FluidFM and confocal fluorescence images and data analysis methods have been described in Chapter 3, and therefore this section restricts itself to elements of the procedures which have not yet been detailed.

### 5.2.1. PDMS substrate preparation and characterisation

The SYLGARD 184 Elastomer Kit (Dow Corning Corporation, Midland, MI) was used to make substrates with different levels of stiffness for cells to grow on. The kit contains 2 parts, a pre-polymer base and the crosslinker curing agent. The base polymer contains the following ingredients: Dimethyl siloxane, dimethylivinyl terminated; Dimethylvinylated and trimethylated silica; Tetra (trimethoxysiloxy) silane; and Ethyl benzene.

The curing agent contains: Dimethyl, methylhydrogen siloxane; Dimethyl siloxane, dimethylvinyl terminated; Dimethylvinylated and trimethylated silica; Tetramethyl tetravinyl cyclotetra siloxane; and Ethyl benzene.
When the two parts are mixed, the curing agent cross-links the polymeric matrix, producing PDMS which will cure from liquid to solid above room temperature. The ratio of base to curing agent, curing time, and curing temperature all contribute to determining the stiffness of the PDMS. In this study, three groups of PDMS were made with different curing agent-to-base ratios (weight/weight) of 1:10, 1:25, and 1:40. These values were chosen because they result in an appropriate range of PDMS stiffness levels, and further details are provided in subsequent sections in this chapter.

The two-part solutions were mixed adequately and then placed in a vacuum chamber (Serven, Rocker 600, UK) for 30 minutes to eliminate air bubbles in the mixtures. Although PDMS is inherently transparent, tiny air bubbles are difficult to remove completely during the curing process, and so the level of transparency which results is still affected to some extent. The FluidFM system uses an inverted microscope, and the light path needs to pass through the entire PDMS layer, and so the layer produced must not be too thick. On the other hand, if the layer is too thin the apparent stiffness of the PDMS surface will be affected by the Petri dish base. Therefore, the thickness of the PDMS needs to be controlled to between 100-200 μm. A measured volume of the mixed solution was injected into the Petri dish (μ-Dish, 50 mm with ibiTreat surface, Ibidi) or a 12-well plate (Sarstedt, Germany) with a syringe so that a layer between 100-200 μm thick was formed at the bottom of the container. The Petri dishes and 12-well plates coated with PDMS were then cured in an incubator at 37°C for 24 hours.

After polymerisation, the Petri dishes were placed in a UV/ozone cleaner (ProCleaner™ Plus, Bioforce Nanosciences, USA) for periods of either 0.5, 1, 1.5, 2, or 3 hours. An in-house goniometer (see Figure 5-1) was set up to measure the static water contact angle of the PDMS samples using a 10 µl needle gauge, and a 4 µl water droplet was placed on the dry PDMS surface using a micropipette. The droplet was left to stabilise for 1 minute, and then photographed using a macro camera so that the contact angle could be measured using the aforementioned software. Because the hydrophilicity of the PDMS surface increases very little after more than 2 hours of treatment time, the PDMS treated for 2 hours was used to culture the cells in this study.

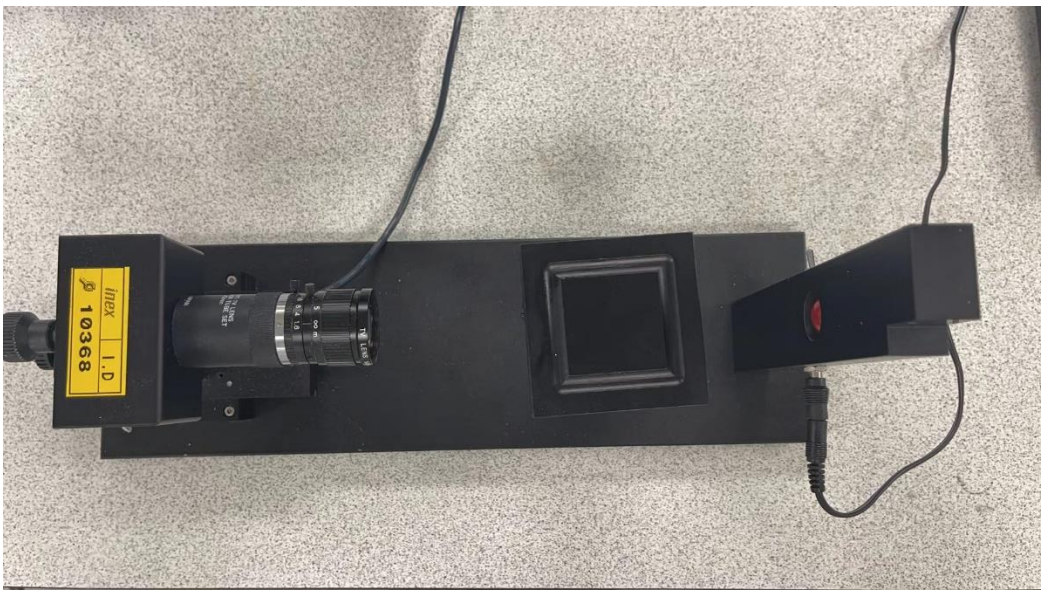


Figure 5-1. In-house goniometer used to measure the static water contact angle of PDMS. The unit consists of a camera on the left, a sample table in the middle and a background light control panel on the right. The camera can be precisely adjusted by knobs for small displacements.

### 5.2.2.Cell culture

MCF-7 and MCF-10A cells (provided by the Northern Institute for Cancer Research, NICR) were cultured in DMEM (Dulbecco's Modified Eagle Medium, Sigma Aldrich) with 10% FBS (Fetal Bovine Serum, Sigma Aldrich) and 1% Penicillin-Streptomycin (Thermo Fisher Scientific) in T75 flasks (Thermo Fisher Scientific) at 37°C and 5% $CO_2$ in an incubator at 95% relative humidity. Cells were split when they grew to 80% confluence. Before the nanoindentation and adhesion experiments, the cells were seeded and cultured in the prepared PDMS-coated Petri dishes (μ-dish 50mm low, iBidi) for 2 days at 37°C, 5% $CO_2$ and 95% relative humidity. These dishes have the low clearance required for the FluidFM working distance.
For the scratching migration test, MCF-7 cells were cultured in the prepared PDMS surface and grew to 80%-90% confluence.

### 5.2.3.3D cell morphology imaging using a confocal microscope

Due to the influence of the PDMS, the A1R with an inverted microscope above the surface was unable to obtain 3D fluorescence images of sufficiently good quality. Therefore, for cells grown on the PDMS, an A1 device with an upright microscope was used in for the confocal fluorescence imaging of cells.

As with A1R confocal imaging, in order to determine contact area, thickness and other 3D information of the cells, they were stained with 5 μM CellTracker™ Green BODIPY™ Dye and CellTracker™ Orange CMRA™ Dye (Thermofisher, UK) for 30 min before imaging separately. Imaging was performed using a Nikon A1 confocal microscope with an NIR Apo 40x 0.80W DIC N2 objective lens. The Green BODIPY™ Dye was excited at a wavelength of 522 nm and a

525/50 nm emission filter was applied, and for the CellTracker™ Orange CMRA Dye with excitation/emission spectra at 541/565 nm a 595/50 filter was used. It was found that the fluorescent molecules produced by the CellTracker™ Green™ Dye deposited a thin layer on the surface of PDMS. This did not occur with the CellTracker™ Orange CMRA Dye, which was therefore used to stain the cells on PDMS. According to Nyquist theory, the resolution was 0.17 μm/pixel, and the z-axis was set at 0.85 μm per step.

### 5.2.4. FluidFM measurement

The protocol of FluidFM for the measurement of stiffness, viscoelasticity, and adhesion for both types of cells on different PDMS surfaces was introduced in Chapter 3. It was noted that the upper surface height (z-coordinate) of the transparent PDMS substrate needs to be determined in order to avoid the probe hitting the upper surface and damaging it during a manual approach.

### 5.2.5. Cell migration measurement

The migration ability of MCF-7 cells was tested using both the scratching test (wound healing test) and the single cell tracking method.

For the scratch test, cells were grown to 80-90% confluence on the PDMS surface, and then a band zone free of cells was scratched in the middle with a 20 μl micropipette tip. The scratched samples were transferred to a Nikon TIE (Nikon, Japanese) for 24-hour time-lapse photography at 10-minute intervals using a Plan Fluor 10x Ph1 DLL lens and in an environment maintained at 37 ℃, 5% $CO_2$, and 95% relative humidity. To prevent the microscope focus missing the cell due to any drift of the Petri dish stage during time-lapse photography,

the focus of the photograph was set at the plane where the cell was located and at distances of ±12 and 24 μm from it. The time-lapse images were analysed using ImageJ. The average distance that the cells had moved was calculated by dividing a newly covered area by the length of the scratch in the field of view (see Figure 5-2).

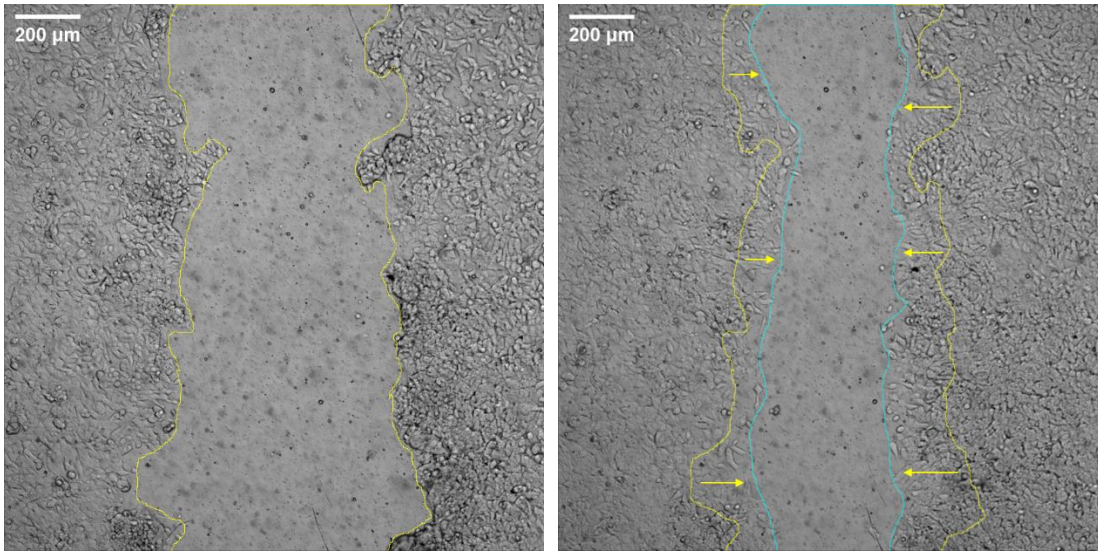


Figure 5-2. Schematic representation of calculated cell migration. The diagram on the left shows a cell scratch at 0 hours, with the edges of the scratch traced in yellow. The diagram on the right shows the cell scratch at 6 hours, with the edge of the cell scratch after moving traced in blue. The area enclosed by the yellow and blue lines was measured and then divided by the length of the image to obtain the average distance the cells had moved. Three petri dishes are performed scratch tests for each data point. For every scratch sample, 5 images are taken, and the time interval is 10 minutes.

For single cell tracking, cells were split and transferred to PDMS substrates in 10% confluence and were then cultured for 2 days, which is consistent with the culturing time for cell attachment to the substrate in the FluidFM experiments. Then the sample was placed in the TIE for 24-hour time-lapse imaging with the same settings as used in the scratching test. The time-lapse images were also analysed using ImageJ, with the orientation of the selected cell marked in every

image, the distance travelled by the cells measured and then divided by the time elapsed to obtain the speed of cell movement.

For both migration tests, 12 well plates (Nunc™ Cell-Culture Treated Multidishes, Thermo Fisher Scientific) were used to improve the efficiency of measurement. The TIE device stage can support 4 x 35mm Petri dishes or a standard size of well plate at the same time, which means that using the 12 well plates in TIE is 3 times faster than using Petri dishes. The migration speeds for cells on the PDMS of the same ratio in the 12-well plate and Petri dishes were compared, and the statistical analysis found no significant difference in cell movement velocities on the same PDMS surface in different containers ($p = 0.123$). Therefore, 12 well plates were used for the time-lapse migration measurements using the TIE device.

For the MCF-10A line, only the single cell tracking method was applied to determine the migration ability of the cells due to the problems with the scratching mentioned above.

ImageJ software was used to analyse cell migration. The raw microscope image was first processed to enhance the contrast, and then the grey scale was inverted so that the cells were light and the background dark. This allowed the TrackMate plug-in [172] to identify the cells and then analyse their path (see Figure 5-3). The core working principle of the TrackMate plug-in is that various superimposed filter algorithms are applied to the time-lapse images to capture the target in each frame, and then the same targets between frames are identified according to a thresholding algorithm to determine if they are moving, and finally the coordinates of the same target in each frame are concatenated to form a trajectory[172]. A LoG (Laplacian of Gauss) detector and simple LAP (Linear Assignment Problem) tracker were used in the TrackMate plug-in, with

an estimated diameter of 65 μm, 10 thresholds, and 120 linking max distance, 50 gap-closing max distance, and 5 gap-closing max frame gap. The linking max distance is the maximum distance that a cell is allowed to move between each frame, and if cells between two frames exceed this distance they are determined to be different cells. The gap-closing parameter is used to compensate for the fact that, in some frames, the recognition algorithm does not correctly identify the cells, and the max distance and max frame gap are thresholds for determining whether or not a cell that reappears at a nearby location after it has disappeared is the original cell. If either of these two thresholds is exceeded, it will be considered to be a new cell.

The mean migration speed is calculated by dividing the displacement of the cell between each frame by the time between frames to obtain the velocity of the cell moving between those two frames, and then averaging the movement velocity over the entire motion trajectory.

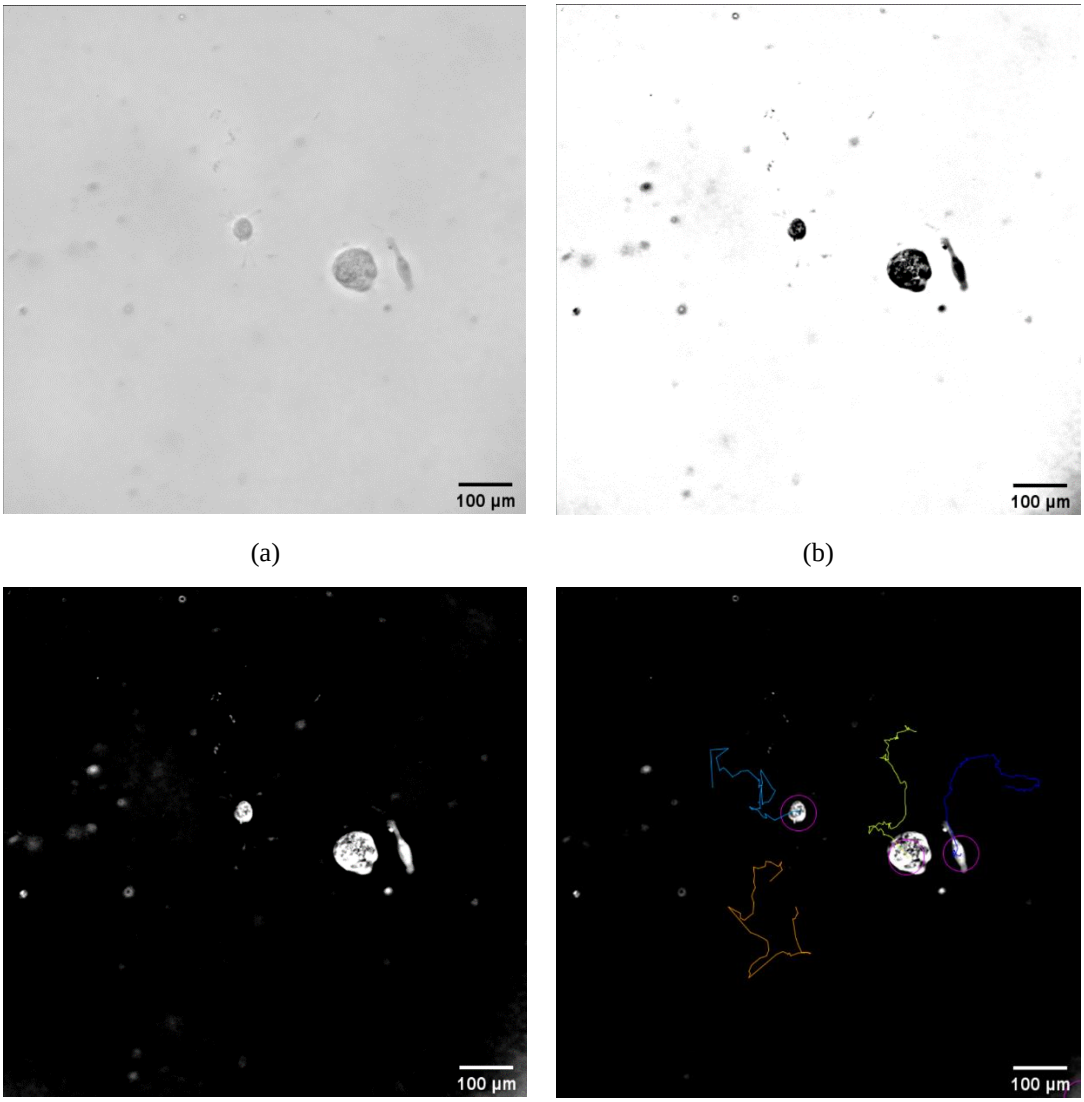


(a) (b)

(c) (d)

Figure 5-3. Analysis of cell migration capacity with ImageJ: (a) original image; (b) image after contrast enhancement; (c) inverting the grey scale of the b-map; (d) tracking cells using the TrackMate plug-in in ImageJ.

## 5.3. Results and Discussion

### 5.3.1. PDMS substrate preparation

The stiffness of PDMS can be controlled according to the proportion of curing agent used. Indentation-relaxation experiments were carried out with 5mm radius flat punch indenter for different PDMS samples and analysed in the same way as cell viscoelasticity, using a Prony series model with one Maxwell arm (Equivalent to the Standard linear solid model) to fit the force curve for the relaxation phase (see Figure 5-4). The calculated results are shown in Figure 5-5

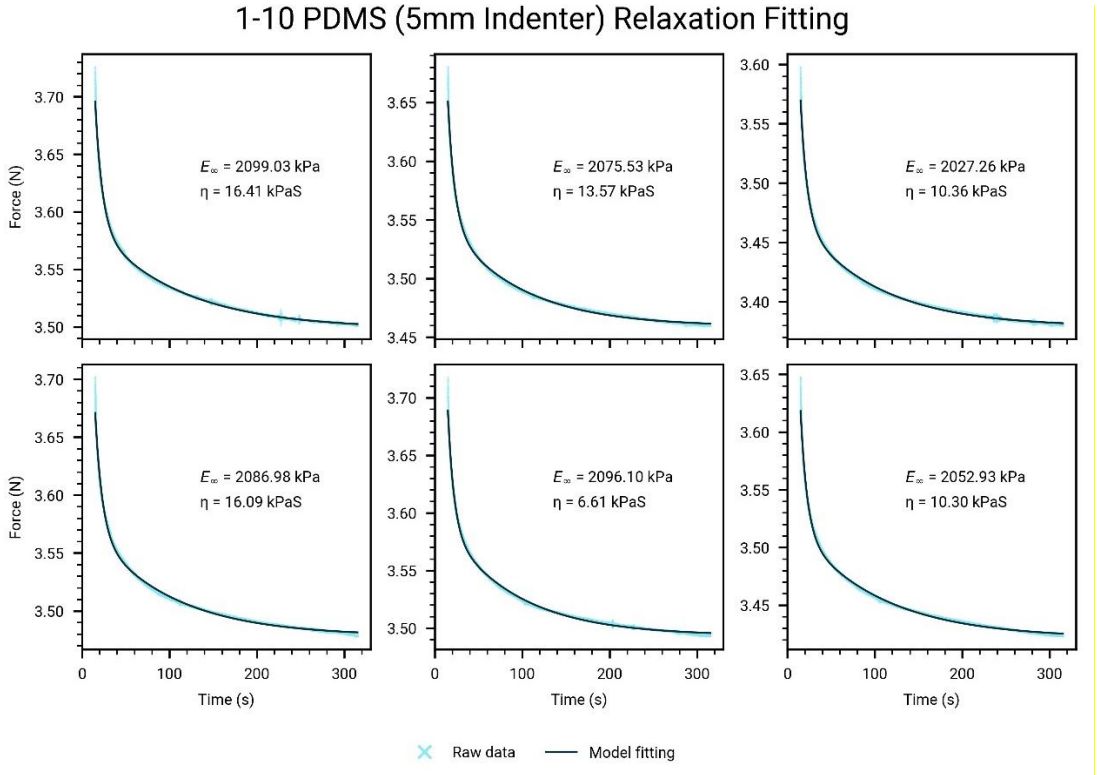


Figure 5-4. Viscoelastic properties characterized by fitting relaxation force curve based on one Maxwell arm Prony series. Six measurements are represented in the diagram. It is shown that the Prony series of one Maxwell arm fits the measurement data well.

The average equilibrium modulus of 1:10 PDMS is 2073 kPa, while the instantaneous modulus is 2119 kPa. The ratio of the equilibrium to

instantaneous moduli is 0.979, and so it can be assumed that 1:10 PDMS is an elastic material[173, 174].

The average elastic modulus of 1:40 PDMS is much smaller than that of 1:10 PDMS, with the equilibrium modulus and the instantaneous modulus being 104.5 kPa and 108.6 kPa respectively which is only 1/20th of that of 1:10 PDMS. In contrast, the ratio of the equilibrium to instantaneous moduli for 1:40 PDMS is 0.962, similar to the case with 1:10 PDMS, so that it can also be regarded as an elastic material. Taking into account the differences in curing temperature and curing time, the various ratios of PDMS modulus of elasticity found in this work are consistent with the findings in other published studies[175, 176].

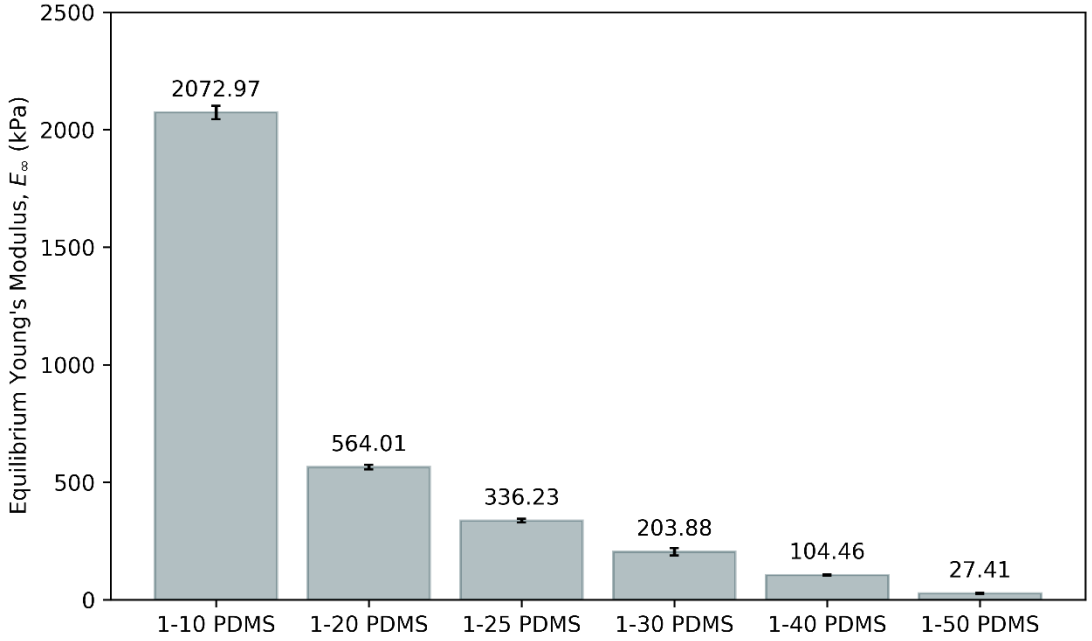


Figure 5-5. Equilibrium modulus of different PDMS samples (n=10).

### 5.3.2. PDMS substrate hydrophilicity and cell attachment improvement using UV ozone treatment

The prepared PDMS samples were treated with the UV Ozone unit for 0.5, 1, 1.5, 2, 2.5 or 3 hours, and their static water contact angles were then measured. Static contact angle with the same treatment time showed no significant difference for different ratios of the PDMS substrates. The results were averaged over 5 tests at each time point. Representative data and images for 1:10 PDMS are shown in Figure 5-6 and Figure 5-7.

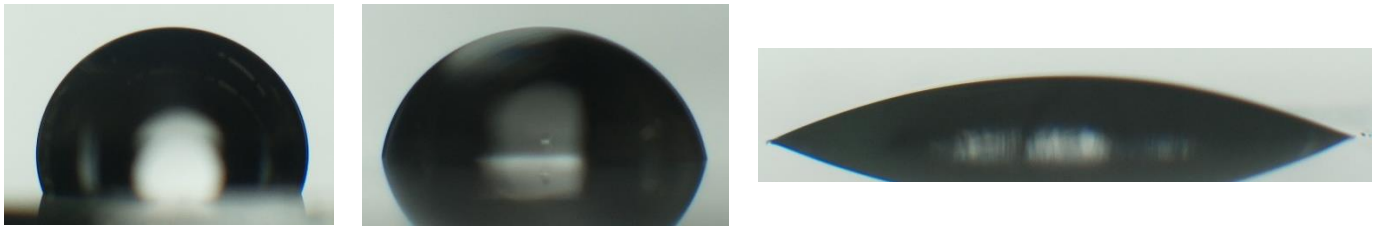

No treatment 1 hour treatment 2 hours treatment

Figure 5-6. Droplet on 1:10 PDMS surfaces for different UV-ozone treatment times. The pictures show that the contact angle of the droplets becomes smaller as the PDMS treatment time increases.

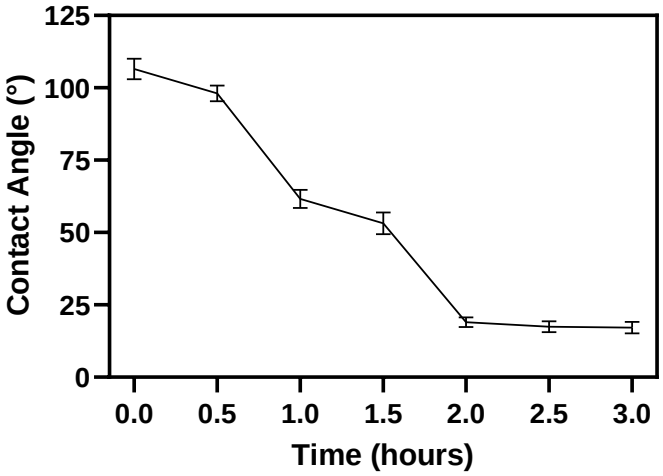


Figure 5-7. Changes in contact angle of 1:10 PDMS surfaces after UV-ozone treatment (n=5). Before 2 hours, the contact angle becomes smaller as the PDMS treatment time increases. But after 2 hours, the contact angle remains constant.

Under ozone UV treatment, the contact angle of the PDMS surface gradually decreased with time. After two hours of treatment, the surface contact angle had decreased from an initial 106° to 20°, showing good hydrophilicity. Longer treatment time resulted in no significant further decrease in contact angle, which remained at around 20°.

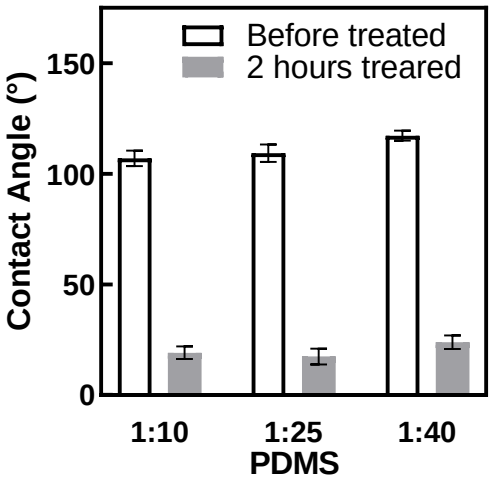


Figure 5-8. Static contact angle of UV/OZONE for treated and untreated PDMS surfaces (n=5).

When the PDMS samples are irradiated by UV/ozone, the Si-C bond on the surface is broken by the UV light resulting in the generation of free radicals, while the UV also causes the oxygen in the air to be converted to ozone, and the strong oxygenation of ozone accelerates the decomposition of organic substances on the PDMS surface, generating more carboxyl and hydroxyl groups. At the same time, Si-OH is produced in large quantities within a short period of time, and this Si-OH undergoes a dehydration reaction resulting in the conversion of the main CH3-Si-O- structure in PDMS to a -O-Si-O- reticulation, resulting in the formation of a thin layer of nearly glassy SiOx ($1 < x < 2$)[177].

When the UV/ozone treatment time exceeded 2h, the contact angle gradually stabilised at around 30°. It can be assumed that the UV/ozone treatment over a long period of time results in the production of more Si-OH on the PDMS surface, which consumes more hydroxyl groups and therefore the surface hydroxyl density gradually increases more slowly and becomes more constant. On the other hand, as the treatment time lengthens, the thin layer of SiOx produced on the surface prevents the ozone from penetrating the PDMS and also blocks some of the UV light, making the reaction unsustainable. In addition, the glass-like structure of the UV/ozone-treated PDMS surface greatly reduces the migration of molecules with hydrophobic groups from the interior to the surface and molecules with hydrophilic groups from the surface to the interior of the PDMS, allowing the surface hydrophilicity to be maintained for a long period of time[178]. In this study, PDMS treated with UV/ozone for two hours and left at room temperature for two days still maintained a high hydrophilicity and the static contact angle increased to a maximum of 117% of the initial value. The hydrophilicity decreased noticeably from the third day onwards, and by one week the static contact angle had become twice the initial value, approximately equal to that of the one-hour treated PDMS. The cells were incubated on the

PDMS substrates for two days in this study, and therefore, a 2-hour treated PDMS was used in conducting the experiment.

The improved hydrophilicity of the PDMS surface makes it easier for extracellular matrix (ECM) to adhere to the PDMS surface and thus facilitates cell adhesion and growth. It can be seen from Figure 5-9 and Figure 5-10 that cell attachment on the UV-ozone- treated PDMS was much better than on the untreated samples.

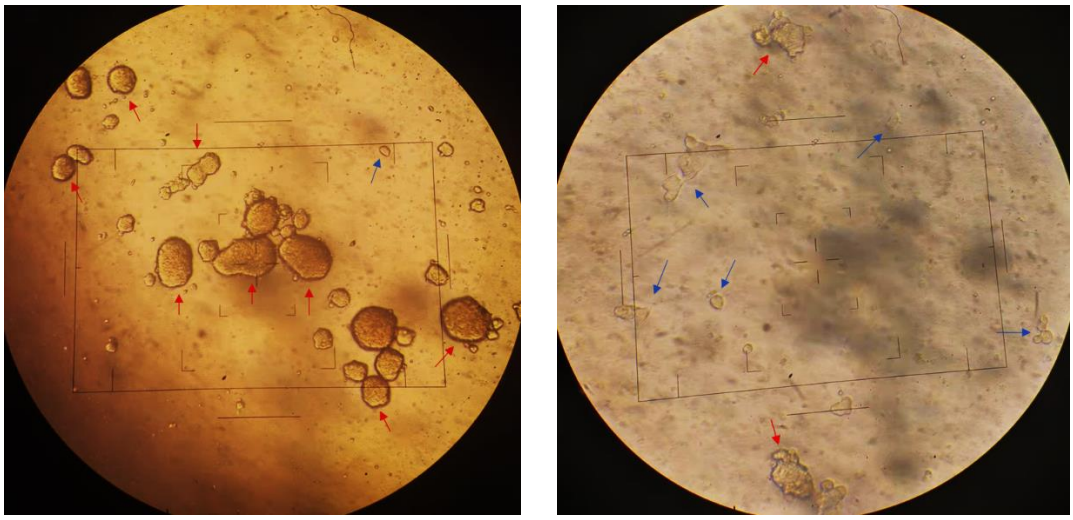

Figure 5-9. Comparison of MCF-7 cell attachment on non-treated (left) and treated (right) 1:10 PDMS surface. The scale boxes in the images are 600x400 μm. Blue arrows mark attached cells while red arrows indicate suspended cell aggregation due to unsuccessful attachment. On the treated PDMS surface, only a small percentage of cells were unable to attach to the substrate, whereas on the untreated PDMS surface only a very small number of cells were able to attach.

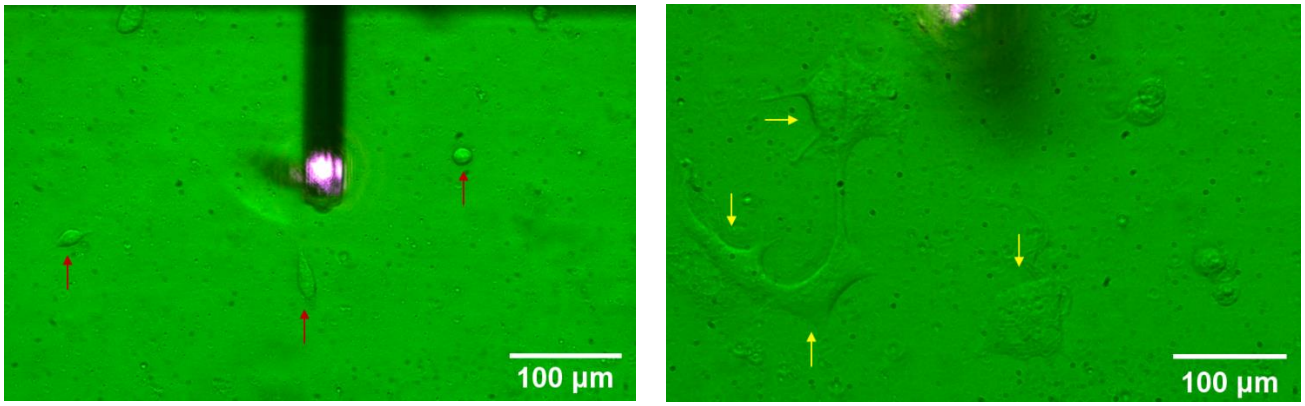


Figure 5-10. Difference in MCF-7 cell morphology on the non-treated (left) and treated (right) PDMS surface. Only a few less-spread cells (red arrows) attach to the non-treated PDMS surface, while well-spread cells (yellow arrows) are common on the treated PDMS surface.

### 5.3.3. Differences in morphology of cells on different PDMS surfaces

At first, the same method was used as in the previous chapter to perform the confocal imaging of cells on PDMS. However, because the A1R device uses an inverted microscope and the additional layer of PDMS substrate between the cells and the objective lens has a negligible impact on the optical path, the images obtained are not of sufficient quality to enable valid data analysis. At the same time, it was found that the previously used CellTracker™ Green BODIPY™ aggregated on the PDMS surface, appearing as a fluorescent layer close to the PDMS surface in the imaging as shown in Figure 5-11. Therefore, the dye used for live cell staining was changed to CellTracker™ Orange CMRA™. The reason for the attraction of the Green BODIPY™ to the PDMS surface when this does not occur with the Orange CMRA™ remains unclear.

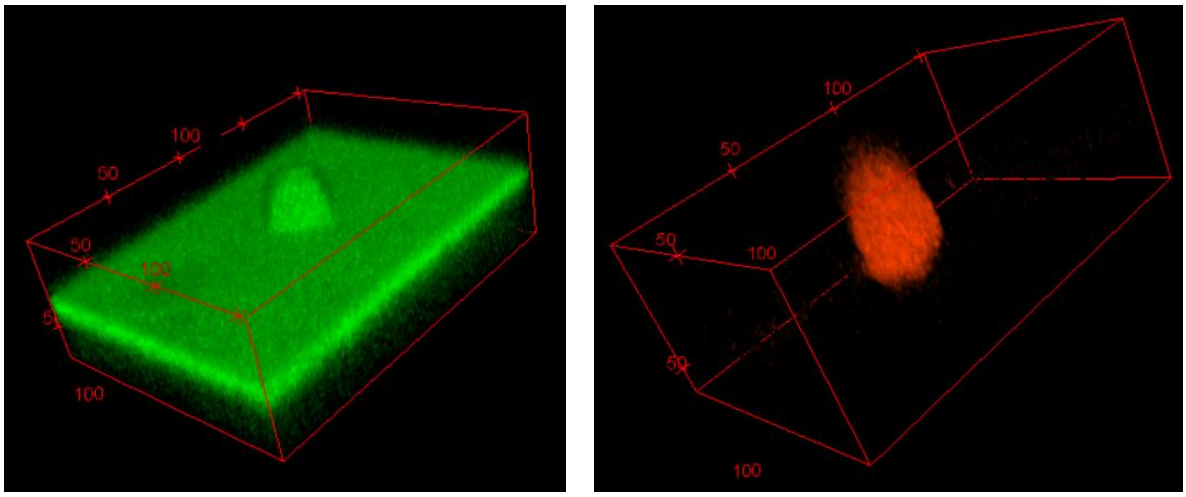


Figure 5-11. Confocal images from the A1R device. The image on the left uses CellTracker™ Green BODIPY™ which is deposited on the surface of the PDMS forming a fluorescent layer that prevents the image from being effectively analysed. The image on the right uses CellTracker™ Orange CMRA™, and although the deposition effect is reduced, the presence of the PDMS between the lens and the cell results in an inaccurate fluorescence signal filtered by the confocal layer. This makes the cells elongated and therefore the results are unusable for analysis. The scale on the box shown is in μm.

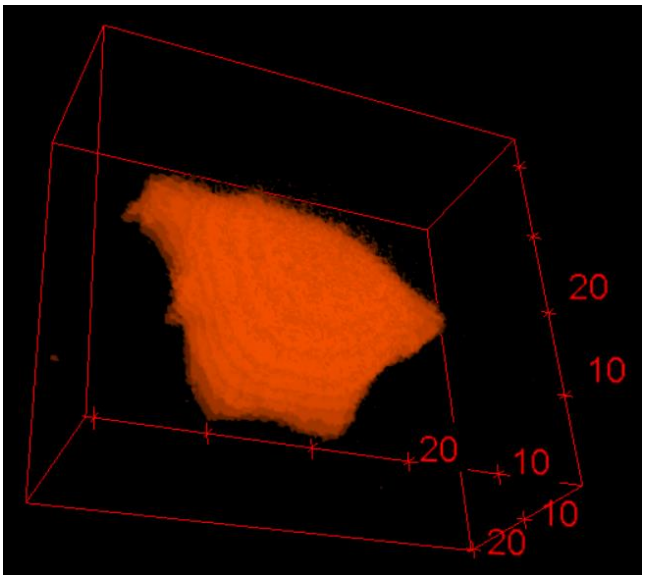


Figure 5-12. Confocal image taken with A1 equipment. The image quality is much clearer due to the use of a upright immersed microscope. The thickness of the cells, the projected area and the contact area are measured and the scale on the box shown is in μm.

In the analysis of the confocal images using the improved method, the thickness of the cells, the area in contact with the bottom surface and the projected area were measured, and the results are shown in Figure 5-13 and Table 2.

The thickness achieved by MCF-7 cells growing on different PDMS surfaces varies. Although there is no statistical difference in the areas of cells on the different PDMS surfaces, cells over large areas can be observed on the harder 1-10 surfaces while this phenomenon is rarer on the other two surfaces. In addition, the ratio of the projected area on all surfaces to the area actually in contact with PDMS is greater than 90%, so that in the FluidFM experiments it can be assumed that the projected area of the cell under the inverted microscope is approximately the same as the area of the cell in contact with PDMS.

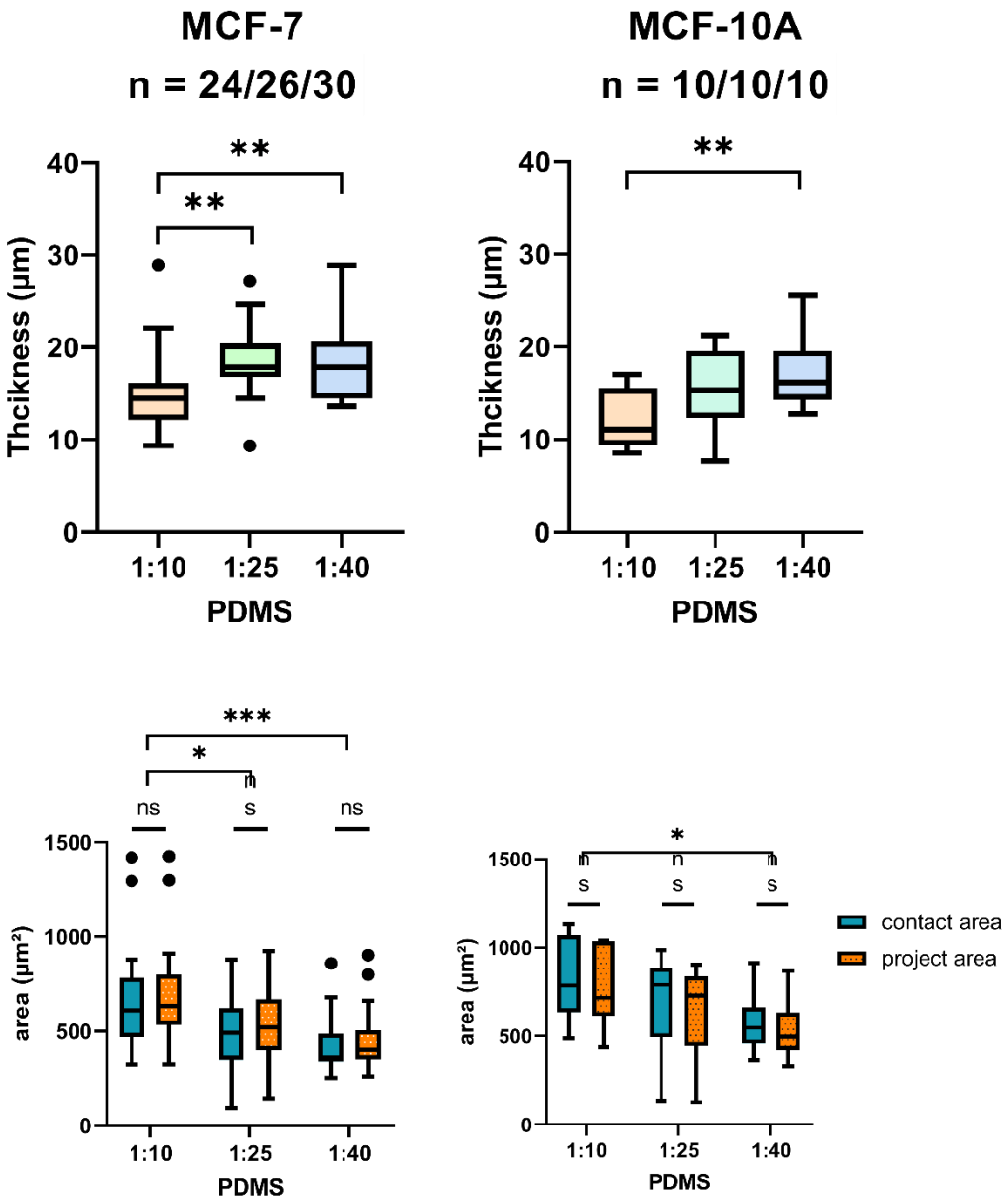


Figure 5-13. Box plots of cell thickness, projected cell area and contact area of MCF-7 and MCF-10A cells on different PDMS surfaces. There was a significant difference between the thickness of cells on the harder PDMS surfaces (1-10) and the thickness of cells on the softer PDMS surfaces (1-25 and 1-40; p = 0.004, 0.007 respectively), with the cells being less thick on the harder surfaces. In contrast, there was no significant difference in the thickness of cells on the 1-25 and 1-40 PDMS surfaces (p = 0.979).

Table 5-1. Morphological parameters of MCF-7 cells on different PDMS surfaces

| | 1:10 (n=24) | 1:25 (n=30) | 1:40 (n=26) |
|---|---|---|---|
| Average thickness (µm) | 15.02 ± 4.3 | 18.38 ± 3.6 | 18.41 ± 4.1 |
| Projected area (µm$^2$) | 689 ± 260 | 531 ± 200 | 451 ± 160 |
| Contact area (µm$^2$) | 661 ± 270 | 490 ± 200 | 428 ± 150 |
| Projected-contact area ratio | 0.95 ± 0.071 | 0.90 ± 0.077 | 0.94 ± 0.054 |

Table 5-2: Morphological parameters of MCF-10A cells on different PDMS surfaces

| | 1:10 (n=10) | 1:25 (n=10) | 1:40 (n=10) |
|---|---|---|---|
| Average thickness (µm) | 12.155 ± 3 | 15.30 ± 4 | 16.92 ± 3.60 |
| Projected area (µm$^2$) | 817 ± 220 | 693 ± 250 | 573 ± 140 |
| Contact area (µm$^2$) | 768 ± 210 | 644 ± 230 | 532 ± 140 |
| Projected-contact area ratio | 0.94± 0.021 | 0.90 ± 0.026 | 0.94 ± 0.033 |

The results for the projected area of the cells in the confocal images are consistent with those obtained with the FluidFM microscope in the previous section and show a decreasing trend as the surface to which the cells are attached becomes softer. Taking into account the thickness of the cells on different surfaces, it can be concluded that the cells contract on softer surfaces and are flatter and larger on stiffer surfaces.

### 5.3.4. Characterization of the mechanical properties of cells on different PDMS surfaces

Similar to the method described in the previous section, FluidFM was used to simultaneously determine the viscoelasticity and adhesion of MCF-7 cells and those of the corresponding healthy MCF-10A cell line on different PDMS surfaces. Cell viscoelasticity, including the instantaneous and equilibrium moduli of the cells, time constants and the viscosity coefficients were analysed based on Prony series. The stress relaxation curves obtained from the measurement were fitted using equation 3.29, resulting in a fit of good quality ( R>0.99; see Figure 5-14a and Figure 5-15a).

The force-displacement curve of the probe was then extracted from the force-time-displacement curve and the work of adhesion required to detach the cells from the surface can be measured and calculated, as shown in Figure 5-14b and Figure 5-15b.

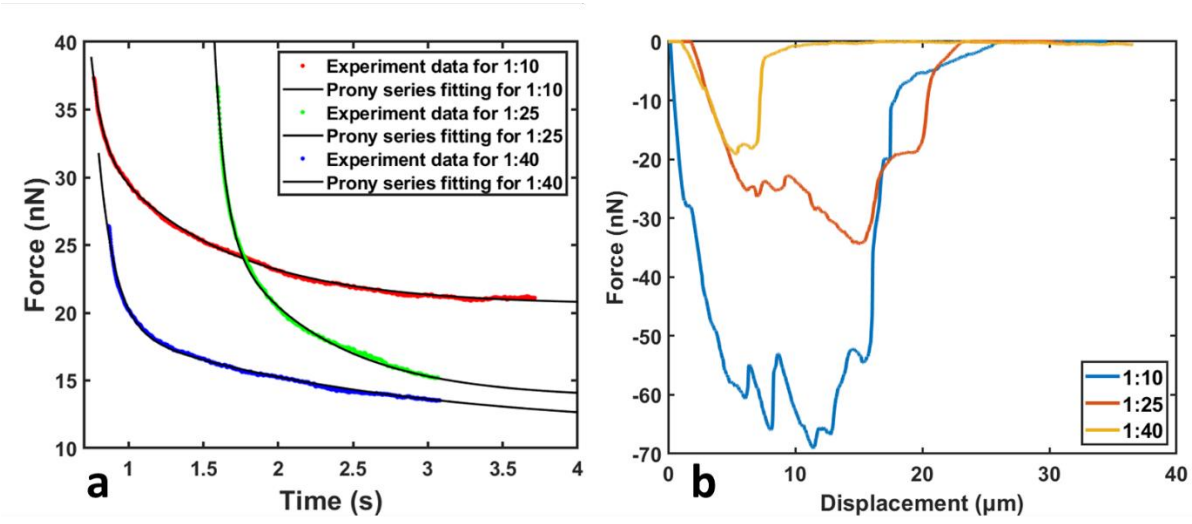


Figure 5-14. Representative curves of MCF-7 cells on different PDMS surfaces for: (a) stress relaxation when the cantilever is resting on the cell after the approaching set-point is reached; and (b) the subsequent detachment curves.

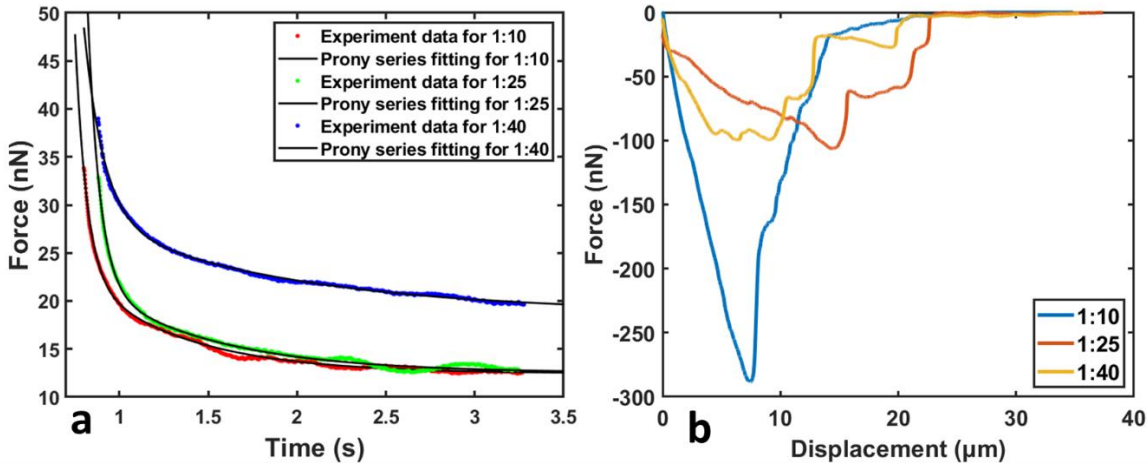


Figure 5-15. Representative curves of MCF-10A cells on different PDMS surfaces for: (a) stress relaxation when the cantilever is resting on the cell after the approaching set-point is reached; and (b) the subsequent detachment curves.

Table 5-3. Properties of MCF-7 cells on different PDMS surfaces

| | 1:10 (n=55) | 1:25 (n=23) | 1:40 (n=25) |
|---|---|---|---|
| Adhesive force F (nN) | 68.97 ± 55 | 31.30 ± 32 | 17.20 ± 13 |
| Adhesion energy W (pJ) | 0.57 ± 0.52 | 0.70 ± 1.2 | 0.18 ± 0.12 |
| Instantaneous modulus $E_0$ (kPa) | 2.21 ± 0.95 | 2.34 ± 0.96 | 1.56 ± 0.45 |
| Equilibrium modulus $E_\infty$ (kPa) | 0.19 ± 0.11 | 0.18 ± 0.12 | 0.13 ± 0.07 |
| Time constant $\tau_1$ (s) | 0.083 ± 0.035 | 0.085 ± 0.027 | 0.10 ± 0.032 |
| Maxwell arm modulus E1 (kPa) | 1.81 ± 0.70 | 1.84 ± 0.86 | 1.28 ± 0.46 |
| Viscosity coefficient $\eta_1$ (Pa·s) | 141.72 ± 56 | 139.97 ± 47 | 133.82 ± 74 |
| Time constant $\tau_2$ (s) | 0.96 ± 0.69 | 1.07 ± 0.53 | 1.04 ± 0.62 |
| Maxwell arm modulus E2 (kPa) | 0.33 ± 0.15 | 0.28 ± 0.11 | 0.12 ± 0.03 |
| Viscosity coefficient $\eta_2$ (Pa·s) | 685.47 ± 2700 | 307.34 ± 280 | 125.14 ± 82 |
| Max adhesion force displacement (μm) | 12.42 ± 12 | 16.59 ± 8.8 | 21.25 ± 10 |
| Fully detached displacement (μm) | 29.72 ± 22 | 29.73 ± 9.2 | 33.2 ± 12 |
| Projected area of cell (μm2) | 721 ± 390 | 590 ± 340 | 410 ± 180 |

Table 5-4. Properties of MCF-10A on different PDMS surfaces

| | 1:10 (n=21) | 1:25 (n=17) | 1:40 (n=16) |
|---|---|---|---|
| Adhesive force F (nN) | 221.25 ± 140 | 115.24 ± 100 | 114.67 ± 60 |
| Adhesion energy W (pJ) | 2.49 ± 1.6 | 1.15 ± 1.05 | 1.01 ± 0.82 |
| Instantaneous modulus $E_0$ (kPa) | 1.36 ± 0.54 | 0.98 ± 0.55 | 1.20 ± 0.53 |
| Equilibrium modulus $E_\infty$ (kPa) | 0.12 ± 0.066 | 0.12 ± 0.056 | 0.15± 0.12 |
| Time constant $\tau_1$ (s) | 0.072 ± 0.023 | 0.089 ± 0.031 | 0.091 ± 0.037 |
| Maxwell arm modulus E1 (kPa) | 1.03 ± 0.51 | 0.83 ± 0.50 | 0.91 ± 0.50 |
| Viscosity coefficient $\eta_1$ (Pa·s) | 70.03 ± 19 | 55.04 ± 32 | 70.21 ± 22 |
| Time constant $\tau_2$ (s) | 1.00 ± 0.54 | 1.30 ± 1.00 | 1.09 ± 0.41 |
| Maxwell arm modulus E2 (kPa) | 0.16 ± 0.073 | 0.14 ± 0.073 | 0.14 ± 0.043 |
| Viscosity coefficient $\eta_2$ (Pa·s) | 161.60 ± 160 | 159.60 ± 82 | 145.71 ± 74 |
| Max adhesion force displacement (μm) | 14.62 ± 6.8 | 15.45 ± 7.2 | 13.90 ± 8.8 |
| Fully detached displacement (μm) | 35.18 ± 12 | 35.31 ± 20 | 29.48 ± 20 |
| Projected area of cell (μm2) | 837 ± 440 | 553 ± 210 | 429 ± 160 |

### 5.3.5. Adhesion and modulus of MCF-7 cells on different PDMS surfaces

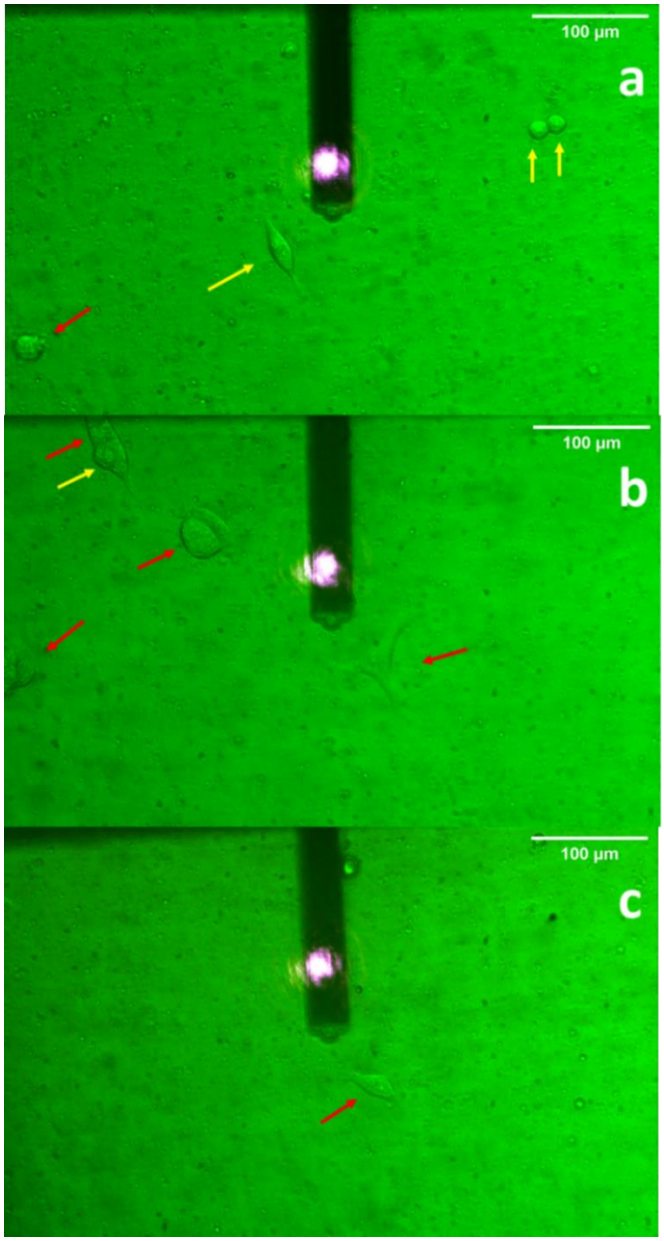


Figure 5-16. MCF-7 cells on different PDMS surfaces, with red arrows showing well-spread cells while yellow arrows show less-spread cells: (a) 1-10 PDMS, where the most attached cells can be seen and well-spread cells outnumber less-spread cells; (b) 1-25 PDMS, with fewer attached cells, and more less-spread cells are visible; (c) 1-40 PDMS, where only a few cells are attached to the substrate.

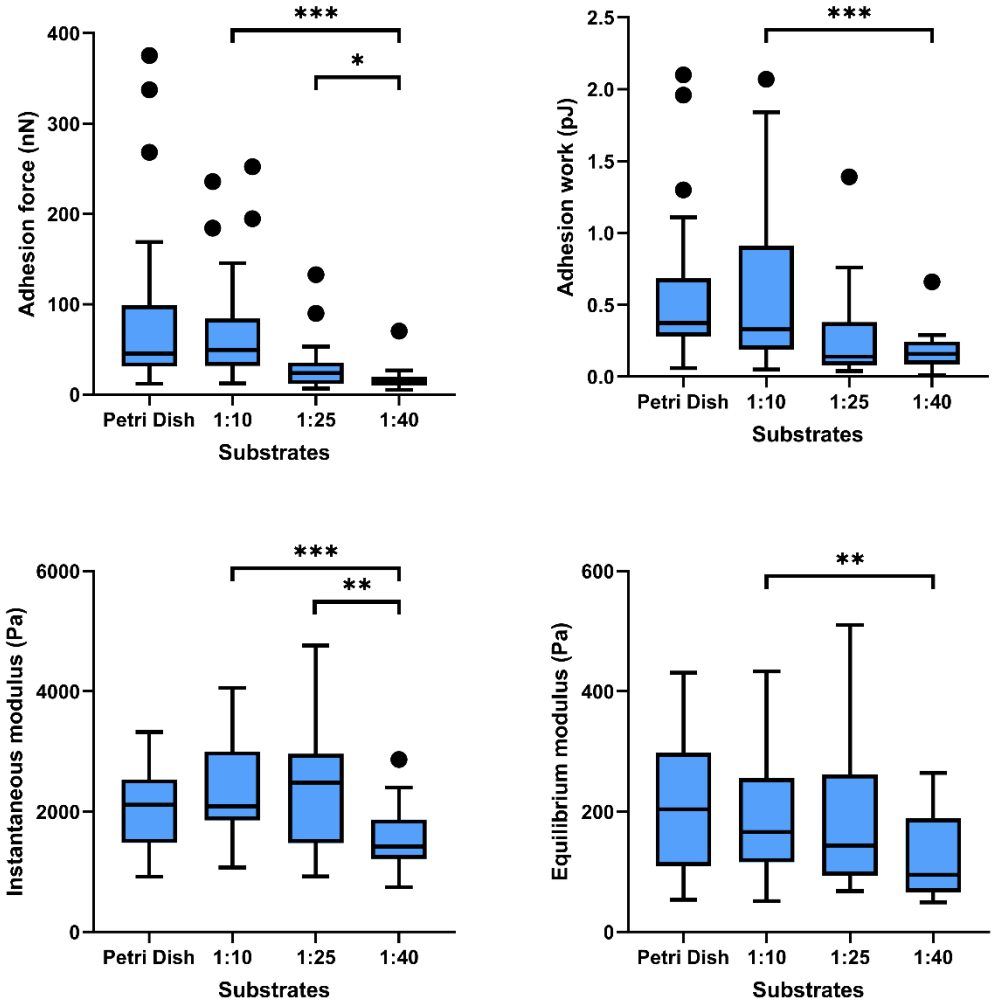


Figure 5-17. Adhesion, instantaneous modulus and equilibrium modulus of MCF-7 on different PDMS substrates. The data of MCF-7 cells on the Petri dish from Chapter 4 are also plotted in the figure for comparation. There are significant differences in adhesion between the 1-10 and 1-40 surfaces (p = 1.71E-8 and 1E-5 respectively in max adhesion force and adhesion work of detachment). The same is the case for the 1-25 and 1-40 groups (p = 0.05 and 0.026 in max adhesion force and adhesion work of detachment respectively). There is no such statistically significant difference between the 1-10 and 1-25 surfaces (p = 0.921 and 0.603), but the overall trend is that a softer surface has cells attached weaker to it. (In this section, the number of MCF-7 data points on different substrates n=47/55/23/25 respectively.)

Figure 5-16 and Figure 5-17 show the adhesion of MCF-7 cells on different PDMS surfaces. Both moduli of MCF-7 cells on different PDMS layers show a decreasing trend as the stiffness of the surface decreases. The instantaneous and equilibrium moduli in the 1-10 group are significantly larger than those in the 1-40 group ($p = 1.6E-5$ and 0.011 respectively). When comparing the 1-10 with the 1-25 group and the 1-25 with the 1-40 group, one of these parameters is significantly different and the other is not: where for the instantaneous modulus, $p=0.828$ and 0005 for 1-10 vs. 1-15 and 1-25 vs. 1-40 respectively; while for the equilibrium modulus, $p=0.697$ and 0.088 for 1-10 vs. 1-15 and 1-25 vs. 1-40.

Because the trends in the moduli and adhesion of cells on different surfaces remain consistent, a correlation analysis was performed for these parameters in an attempt to interpret the relationship between these mechanical properties in the context of findings in the literature.

Table 5-5. Pearson's correlation analysis of adhesion and moduli of MCF-7 cells

| | | Adhesion work | Instantaneous modulus | Equilibrium modulus |
|---|---|---|---|---|
| Adhesion force | Pearson correlation | 0.92** | 0.04 | 0.58** |
| | Sig. (2-tailed) | 2.73E-43 | 0.70 | 1.33E-8 |
| | N | 102 | 82 | 82 |
| Adhesion work | Pearson correlation | - | -0.03 | 0.59** |
| | Sig. (2-tailed) | - | 0.79 | 7.45E-9 |
| | N | - | 82 | 82 |
| Instantaneous modulus | Pearson correlation | - | - | 0.37** |
| | Sig. (2-tailed) | - | - | 0.00 |
| | N | - | - | 88 |

As can be seen from the table, adhesion force and adhesion work are strongly correlated, and explanations for this have been discussed in the previous chapter. Because the adhesion work of a cell is approximately equal to the adhesion force multiplied by the separation distance, and since the cells are able to deform to a similar extent and have similar separation distances from the surface in the adhesion force measurement experiments, adhesion force and adhesion work can be expected to be approximately linearly correlated. Meanwhile, the instantaneous and equilibrium moduli are correlated because both moduli are the result of the combined action of multiple subcellular structures[62-64, 179].

The equilibrium modulus is strongly correlated with both adhesion force and adhesion work. This is due to the fact that the actin-myosin, which are the intermediate filaments that contribute to the cell modulus, and the non-specific cellular junctions that contribute to the cell-to-surface adhesion force (for example, in focal adhesion) are linked together in tandem in the cytoskeleton[180, 181]. The mechanism by which mechanotransduction from cell junctions on the cell membrane to the interior of the cell affects the cell modulus is as yet unclear.

It is worth noting that the equilibrium modulus is significantly correlated with the adhesion of the cell, and that both the instantaneous and equilibrium moduli are also linearly correlated. However, the instantaneous modulus is not significantly correlated with adhesion, and therefore further partial correlation analysis was performed for instantaneous modulus and adhesion.

Table 5-6. Partial correlation analysis of instantaneous modulus and cell-to-surface adhesion

| Variable | Control variable | | Adhesion force | Adhesion work |
|---|---|---|---|---|
| Instantaneous modulus | PDMS surface | Correlation | -0.071 | -0.11 |
| | | Significance (2-tailed) | 0.53 | 0.33 |
| | | df | 79 | 79 |
| | Equilibrium modulus | Correlation | -0.24 | -0.35 |
| | | Significance (2-tailed) | 0.029 | 0.002 |
| | | df | 79.00 | 79.00 |
| | PDMS surface and equilibrium modulus | Correlation | -0.31 | -0.38 |
| | | Significance (2-tailed) | 0.0048 | 0.00057 |
| | | df | 78 | 78 |

Considering the effect of different surface groupings, this variable was first used as a control variable in the partial correlation analysis of instantaneous modulus against adhesion. The results in Table 5-6 show that, when the effect of surface grouping is excluded, the correlation between the cell's instantaneous modulus

and cell-to-surface adhesion increased but was still not statistically significant. Next, equilibrium modulus was used as a control variable and partial correlation analysis was applied for the cell's instantaneous modulus and cell-to-surface adhesion. It was found that once the effect of the equilibrium modulus of the cell was excluded, the instantaneous modulus showed a significant correlation with adhesion. When the effects of both PDMS grouping and equilibrium modulus were also excluded, the significance of the correlation between cell transient modulus and cell-surface adhesion was further enhanced to show a negative correlation.

This suggests that the remaining factors affecting the transient modulus and those affecting cell adhesion capacity may mutually inhibit each other after the exclusion of common factors affecting both moduli. Although the subcellular components that contribute to the cell equilibrium and instantaneous moduli are not yet clear, this result may provide a hypothetical insight in the study of the mechanisms by which subcellular structures affect the mechanical properties of cells, and could be a reference point in the later quantification of the effects of subcellular structures and their behaviour on the overall mechanical properties of cells.

**Viscoelasticity of MCF-7 on different PDMS surfaces**

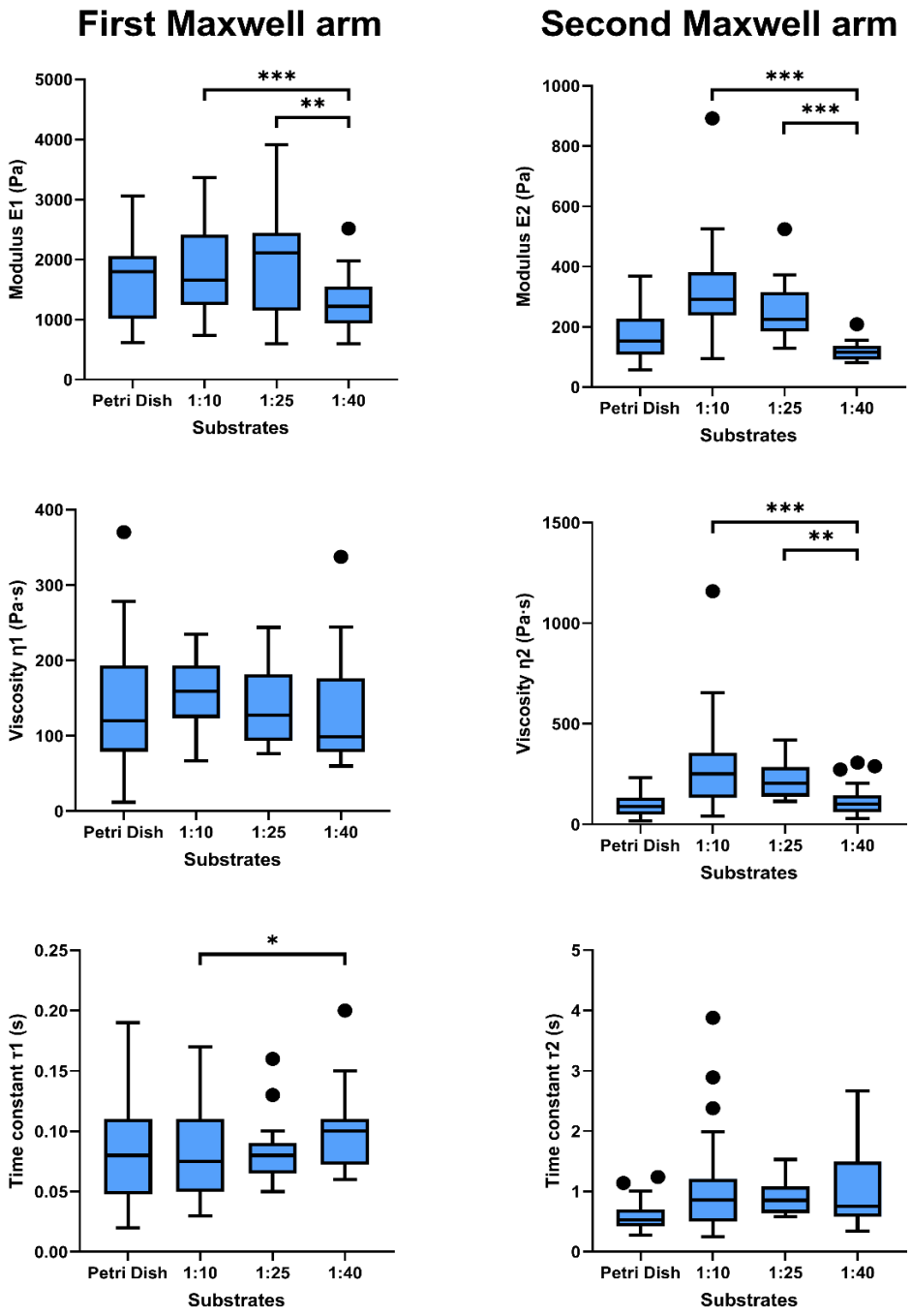


Figure 5-18. Viscoelastic parameters of the Maxwell arms of MCF-7 cells on different PDMS surfaces compared to cells on the Petri dish: (a) first Maxwell arm modulus $E_i$; (b) viscosity coefficient $\eta_i$; (c) relaxation time constant $\tau_i$. The data of MCF-7 cells on the Petri dish from Chapter 4 is also plotted in the figure for comparison.

Viscoelastic data for the first Maxwell arm of MCF-7 cells are shown in Figure 5-18. The elastic modulus E1 tends to decrease as the hardness of the surface the cell is attached to becomes softer, with a significant difference between the values on the 1:10 PDMS surface compared to the 1:40 PDMS surface ($p = 0.00039$). However, values of viscosity n1 were not significantly different on different surfaces. Based on these two results, the relaxation time constant $\tau 1$, which is equal to n1/E1, is greater on softer surfaces.

Although the elastic modulus E2 and viscosity $\eta 2$ of the cells on PDMS decreased as the layer became softer, with a significant difference for 1:10 compared to 1:40 PDMS, this trend was not consistent given the values for the cells on the Petri dishes. The time constants, $\tau 2$, of the cells on PDMS did not significantly differ, but they were significantly greater than the values for the cells on the Petri dishes.

**Adhesion and modulus of MCF-10A on different PDMS surfaces**

Because the adhesion force between MCF-10A cells and the surface after 48 hours of growth on the Petri dish was too high for the well-spread cells to be separated from the surface in most of the FluidFM experiments, measurements were then taken only of the adhesion of cells grown on different PDMS materials. (In this section, the number of MCF-10A data points on different substrates n=21/17/16 respectively.)

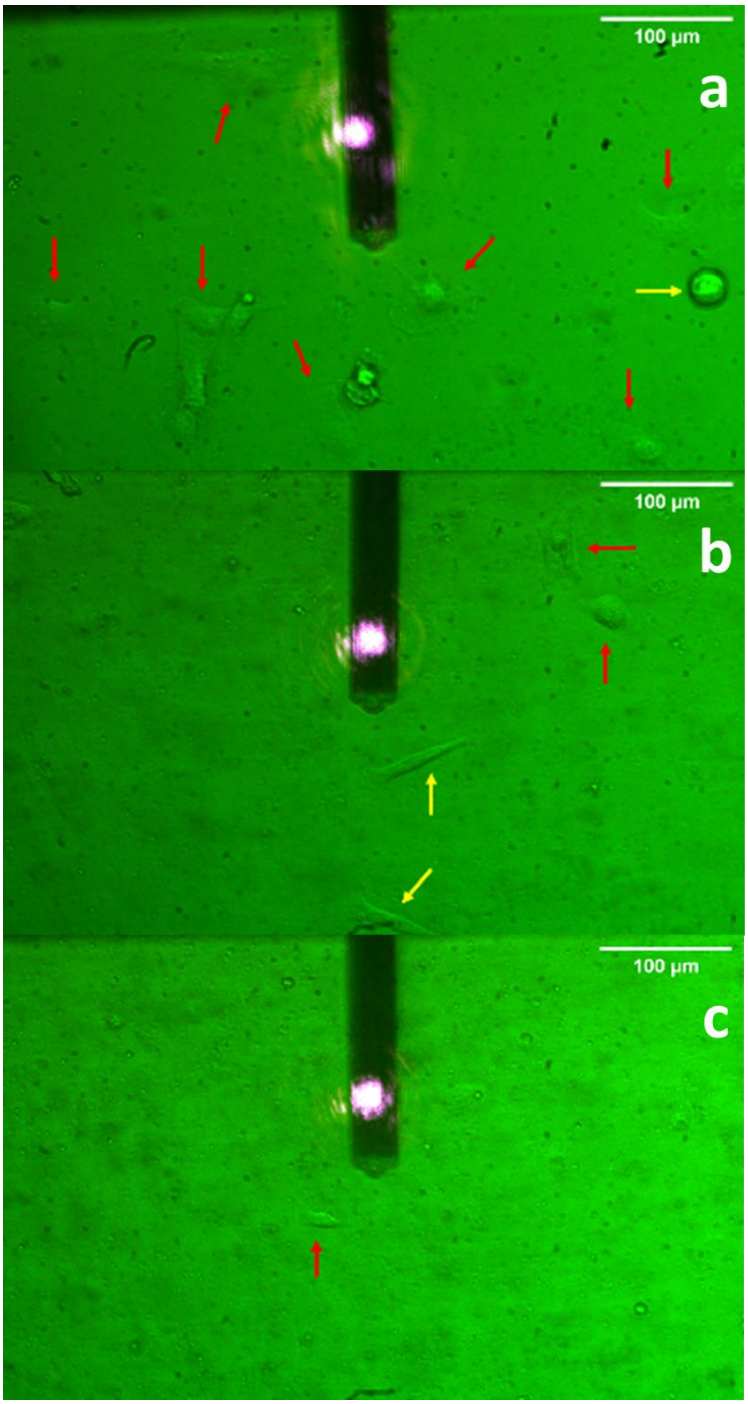


Figure 5-19. MCF-10A cells on different PDMS surfaces, with red arrows showing the well-spread cells while yellow arrows show less-spread cells: (a) 1-10 PDMS, where the number of attached cells is larger than in the other two groups; (b) 1-25 PDMS, where there are fewer attached cells, and the proportion of less-spread cells increases; (c) 1-40 PDMS, with only a few cells attached to the substrate.

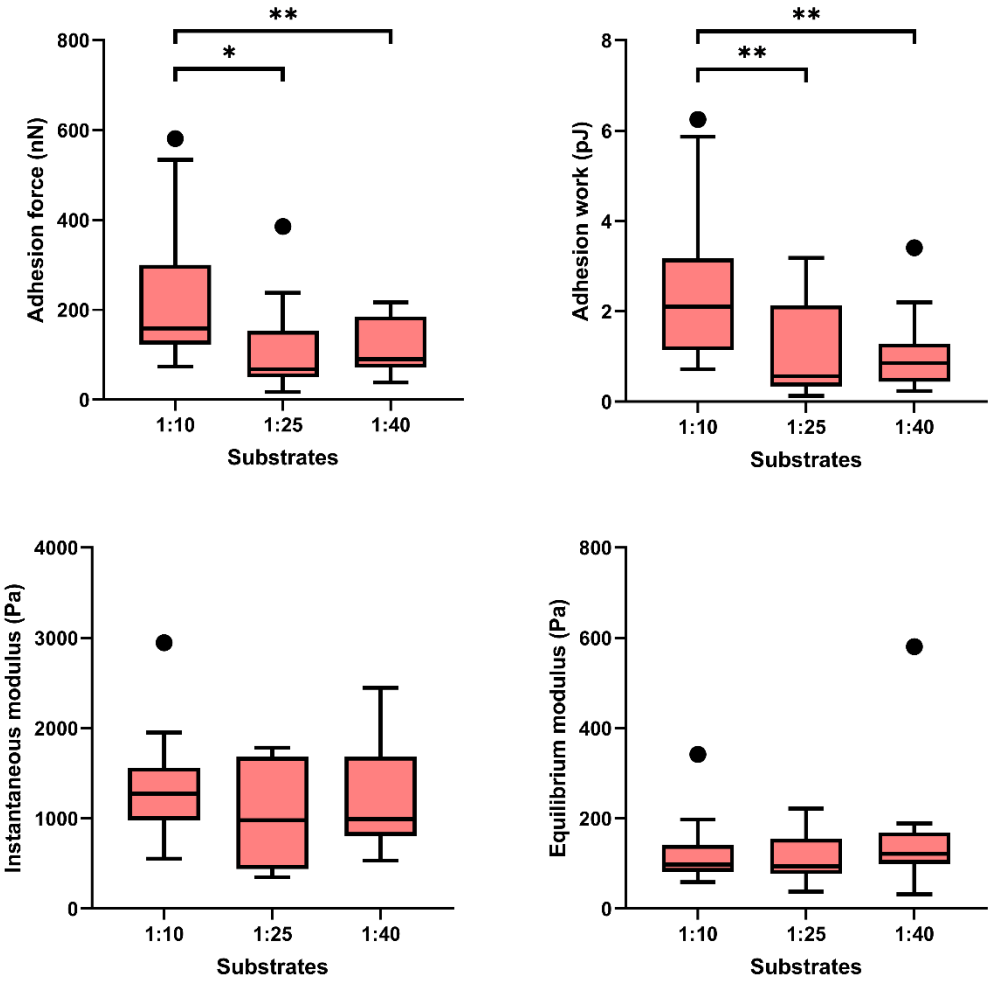


Figure 5-20. Adhesion and instantaneous and equilibrium moduli of MCF-10A on different PDMS substrates.

Compared to the corresponding MCF-7cancer cells, the adhesion between MCF-10A and PDMS was more than twice as strong on the same PDMS surface, with max adhesion forces on the surfaces of PDMS of 1-10, 1-25, and 1-40 at 221.25 ± 140 nN, 115.24 ± 100 nN, 114.67 ± 60 nN respectively and adhesion energy of 2.49 ± 1.6 pJ, 1.15 ± 1 pJ, 1.01 ± 0.82 pJ respectively. Ani *et al*. 2019 measured the adhesion force of MCF-10A and another breast cancer cell line, MDA-MB 231, to 1:10 PDMS material, and the adhesion forces required for the MCF-10A and MDA-MB-231 breast cancer cells to be pulled off

from the PDMS surface were 211 ± 50 nN and 133 ± 46 nN respectively[182]. Our measurement results for MCF-10A and PDMS surface adhesion force are consistent with those findings, and also indicate that the adhesion of cells of the normal breast cell line MCF-10A is stronger than that of the cancerous breast cell line.

There were no significant differences in either the instantaneous or equilibrium moduli exhibited by the MCF-10A cells on different PDMS surfaces. What is more notable is that they all have smaller values than those for MCF-7 cells on the same PDMS surface and, in general, the stiffness of MCF-10A in breast epithelial cells is greater than that of other breast cancer cells[10, 183-185]. This unusual phenomenon may be caused by the MCF-10A cell sensing a reduction in the hardness of the surface to which it is attached and thus changing its mechanical properties[50, 186].

No published data on the stiffness of MCF-10A on PDMS surfaces could be found in the literature, while the stiffness data for MCF-10A using AFM measurements on Petri dish surfaces vary widely from 0.25 kPa to 6 kPa[183, 184, 187-191]. The reason for such large discrepancies could be that these papers do not take into account the viscoelasticity of the cells despite the fact that some researchers have found that loading rate affects the final measurements[189], and the authors simply used the Hertz model to calculate the apparent elastic modulus of the cells. The relaxation time and viscosity measurements presented by Yasaman Nematbakhsh et al. (2017) are similar to the results in the present study (with detailed data shown in the following section), and so their apparent Young’s modulus findings are also relevant here. The Young's modulus measured for MCF-10A is 700 Pa, which is greater than that for MCF-7 of 550 Pa[184].

A correlation analysis was also performed for the adhesion and moduli of MCF-10A to compare with MCF-7. In contrast to MCF-7, there was no significant correlation between adhesion and moduli in MCF-10A cells.

Table 5-7: Pearson's correlation analysis of adhesion and moduli of MCF-10A

| | | Adhesion work | Instantaneous modulus | Equilibrium modulus |
|---|---|---|---|---|
| Adhesion force | Pearson Correlation | 0.852** | -0.202 | 0.066 |
| | Sig. (2-tailed) | 0.000 | 0.184 | 0.667 |
| | N | 52 | 45 | 45 |
| Adhesion work | Pearson Correlation | - | -0.065 | -0.067 |
| | Sig. (2-tailed) | - | 0.671 | 0.663 |
| | N | - | 45 | 45 |
| Instantaneous modulus | Pearson Correlation | - | - | 0.296* |
| | Sig. (2-tailed) | - | - | 0.048 |
| | N | - | - | 45 |

**. Correlation is significant at the 0.01 level (2-tailed).

*. Correlation is significant at the 0.05 level (2-tailed).

## Viscoelasticity of MCF-10A on different PDMS surfaces

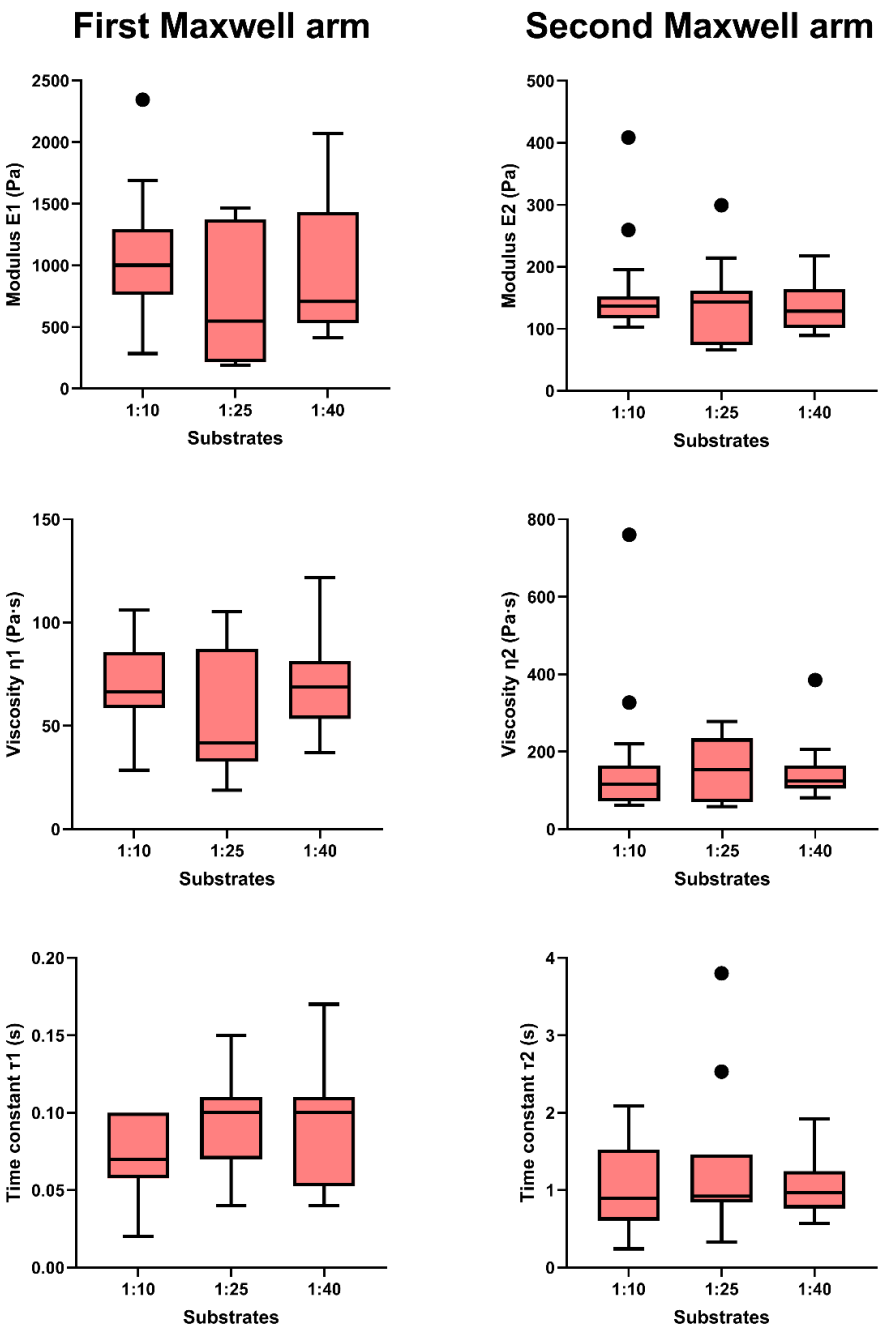


Figure 5-21. Viscoelastic parameters of the Maxwell arms of MCF-10A cells on different PDMS surfaces: (a) first Maxwell arm modulus Ei; (b) viscosity coefficient ηi; (c) relaxation time constant τi. The viscosity parameters of MCF-10A on different PDMS surfaces do not change significantly with the stiffness of the surface the cells are attached to.

The viscosity results for MCF-10A obtained by Yasaman (2017) using the Prony series model with a single Maxwell arm was 65 Pa·s for adhered cells and 40 Pa·s for suspended cells, with relaxation time constants of 2 s and 1.2 s when calculated using the loading and relaxation periods respectively. Despite the different Prony series models used, the measurements in the present study are reasonably comparable[184].

## 5.4. Comparison of the mechanical properties of MCF-7 and MCF-10A cells

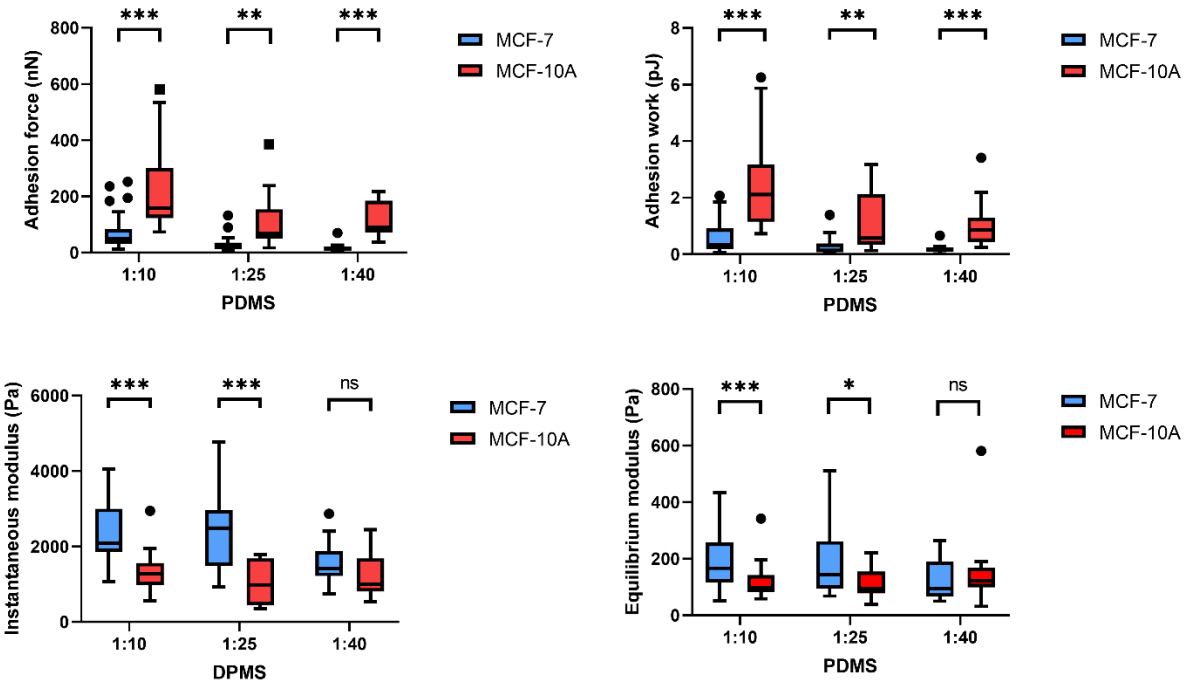


Figure 5-22. Comparison of adhesion and instantaneous and equilibrium moduli of MCF-7 and MCF-10A cells on different PDMS substrates. There are significant differences between MCF-7 and MCF-10A in adhesion and moduli on all surfaces, except for the 1:40 PDMS surface where there are no significant differences in both instantaneous and equilibrium moduli. (In this section, the number of MCF-7 and MCF-10A data points on different substrates are n=55/23/25 and n=21/17/16 respectively.)

The adhesion of MCF-7 to substrates in breast epithelial cancer cells is less than that of MCF-10A in normal breast epithelial cells, this result consists with the data reported in other studies[192, 193]. Furthermore, cancer is also associated with a lack of intercellular or cell-extracellular matrix adhesion[60, 194, 195].

However, the moduli of MCF-7 measured in this study were significantly greater than those of MCF-10A, which is contradicts the findings of other studies of these two cell lines[115, 156, 196-198]. In all of the above literature, the measurements of the Young's modulus of the cell did not consider the substrate effect and other effects, and therefore can lead to discrepancies between the measured and actual values.

The reasons for this are currently unclear and should be investigated in Chapter 6 using simulation approach and also in future studies.

## Cell migration on different PDMS surfaces

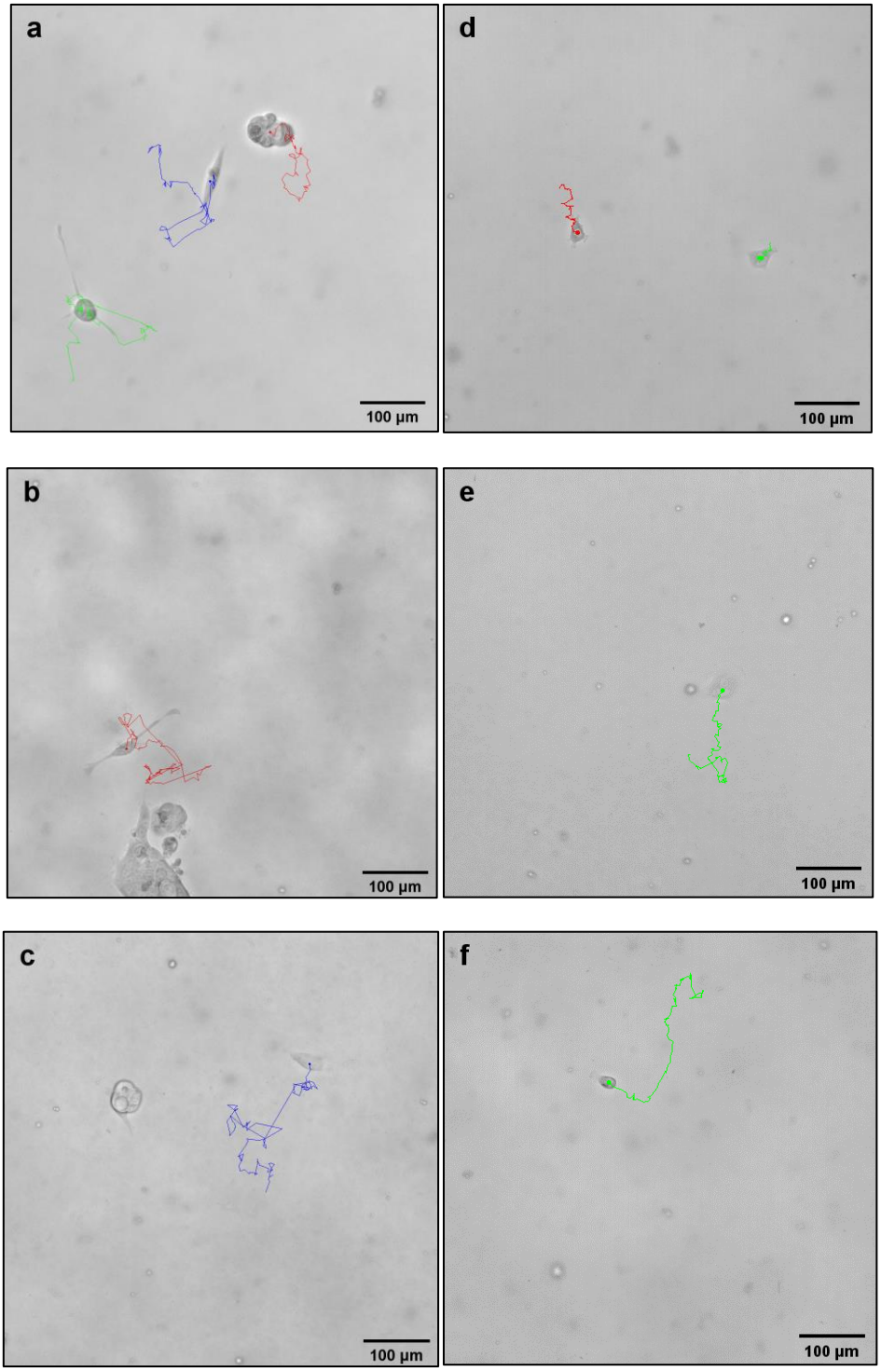


Figure 5-23. Trajectories of cells cultured on different PDMS surfaces for 24 hours. (a), (b), (c) MCF-7 cells on 1:10, 1:25, 1:40 PDMS substrates respectively; (d), (e), (f) MCF-10A cells on 1:10, 1:25, 1:40 PDMS substrates respectively.

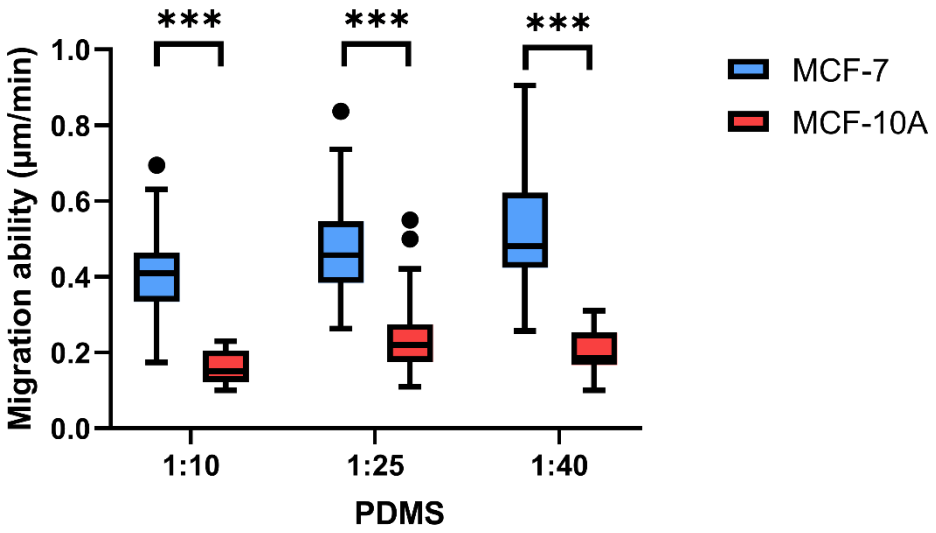


Figure 5-24. Mean migration speed of MCF-7 and MCF-10A cells on different PDMS surfaces. The migration ability of MCF-7 cells was significantly greater than that of MCF-10A cells on all three PDMS surfaces with different stiffnesses, with p values less than the 0.001 level. (The number of MCF-7 and MCF-10A data points on different substrates are shown in Table 5-8.)

Table 5-8. Speed of movement of MCF-7 and MCF-10A cells on different PDMS surfaces

| Average migration speed (μm/min) | 1:10 | 1:25 | 1:40 |
|---|---|---|---|
| MCF-7 | 0.41 ± 0.11 (n=35) | 0.47 ± 0.12 (n=35) | 0.53 ± 0.18 (n=22) |
| MCF-10A | 0.16 ± 0.041 (n=20) | 0.25 ± 0.11 (n=26) | 0.21 ± 0.052 (n=18) |

Single cell tracking revealed that the migration speed of MCF-7 cells is faster than that of MCF-10A cells, while both types of cells move faster on softer PDMS substrates. The reason for this may be that there is greater adhesion between the cells and hard surfaces, thus inhibiting the capability to migrate[195, 199].

In addition, time-lapse photography still demonstrated that individual cells move faster than multicellular aggregates. It was also observed that cells would become briefly detached from the PDMS surface and then reattach in order to move a long distance. Moreover, cells attached to the surface would also trap free suspended cells, causing the latter to also attach to the surface. Sometimes an attached cell would even attract suspended ECM debris, which may reveal the possibility that the range of action of cell adhesion is much wider than the contact range of cell junctions.

## 5.5. Conclusions

As described in this chapter, PDMS substrates have been produced that facilitate the study of cells on surfaces of varying hardness, and UV ozone treatment has been used to improve their hydrophilicity, making the surface more suitable for cell adhesion and growth.

Individual cell-surface detachment experiments were then performed with FluidFM to measure cell-surface adhesion and the viscoelastic properties of MCF-7 and MCF-10A cells on PDMS surfaces with different levels of stiffness. We have further revealed that breast cancer cell line MFC-7 have less ability to adhere to the various stiffness surfaces than the heathy cell line MCF-10A. On 1:10, 1:25, and 1:40 PDMS substrates, the adhesion forces of MCF-7 / MCF-10A are (in the unit of nN) 68.97 ± 55 / 221.25 ± 140, 31.30 ± 32 / 115.24 ± 100, and 17.20 ± 13 / 114.67 ± 60, respectively.

The modulus of MCF-7 cells is lower as the underlying substrate becomes softer, instantaneous / equilibrium modulus on 1:10, 1:25, and 1:40 PDMS substrates are (in the unit of kPa) 2.21 ± 0.95 / 0.19 ± 0.11, 2.34 ± 0.96 / 0.18 ± 0.12, 1.56 ± 0.45 / 0.13 ± 0.07, respectively.

Meanwhile the viscoelastic parameters of MCF-10A cells do not vary significantly with the stiffness of the attached surface. Time constant $\tau_1$ / $\tau_2$ are 0.072 ± 0.023 / 1 ± 0.54, 0.089 ± 0.031 / 1.3 ± 1, 0.091 ± 0.037 / 1.09 ± 0.41 when they are on the 1:10, 1:25, and 1:40 PDMS substrates.

The experimental results for the adhesion, spread area and stiffness of MCF-7 and MCF-10A cells are also consistent with findings published in the literature, where a stiffer substrate and larger cell-matrix contact area are associated with greater cell-matrix adhesion and thus a reduced migration speed of cells[200, 201].

The moduli of MCF-7 measured in Chapter 5 were significantly larger than the moduli of MCF-10A, in contrast to other articles. Therefore, the measurements need to be calibrated in the following chapter.

Further analysis of the data was conducted using statistical methods to identify correlations among parameters of cellular mechanical properties and to provide plausible explanations of the findings in the light of previous research. A number of mechanical models of subcellular structures proposed in the literature are supported by the present experimental and empirical findings.

An improved protocol of fluorescent confocal imaging was deployed to determine aspects of the 3D structure of cells on different PDMS surfaces. It was discovered that the cells tend to contract when on soft surfaces and become flatter and wider on stiff surfaces. The contact area of MCF-7 / MCF-10A cells on the 1:10, 1:25 and 1:40 PDMS substrates are 661 ± 269 / 817 ± 222, 490 ± 202 / 693 ± 251 and 428 ± 148 / 573 ± 144 ($\mu m^2$), respectively. While their corresponding thickness are 15.02 ± 4.32 / 12.155 ± 2.97, 18.38 ± 3.56 / 15.30 ± 3.98 and 18.41 ± 4.11 / 16.92 ± 3.60 (μm).

These findings were consistent with the nature of cells on different surfaces as observed using FluidFM microscopy, and also provides secondary corroboration of the mechanical model of the cell as well as improving the data used for subsequent FEA simulation modelling.

Finally, time-lapse photography was performed of cells on different surfaces using microscopy and it was found that the movement speed of both types of cells when migrating decreased on the stiffer substrate. The average migration speeds of MCF-7 / MCF-10A on 1:10, 1:25 and 1:40 PDMS substrates are 0.41 ± 0.11 / 0.16 ± 0.041, 0.47 ± 0.12 / 0.25 ± 0.11 and 0.53 ± 0.18 / 0.21 ± 0.052 (μm/min), respectively.

It was also found that the cells could actively become detached from the surface and re-attach after rapid movement, and that cells already attached to the surface could trap suspended cells to help them attach to the surface. This may indicate that cell adhesion has a much wider range of action than cell junctions.

# Chapter 6. Finite element (FE) model verification and calibration

## 6.1. Introduction

The previous two chapters have analysed the mechanical properties, morphology and migration capacity of MCF-7 and MCF-10A cells in different environments using a viscoelastic model. However, during the analysis of data from the experiments, there are several points that no longer fit the assumptions of theory, such as the replacement of irregularly shaped contact areas with circles of equivalent area, thus approximating the flat-punch contact model for calculations. Furthermore, the modified Sneddon model is only applicable to an infinite half-space where the indentation depth and flat-punch indenter radius are much smaller than the thickness of the sample being measured[128, 202, 203], whereas the actual measurement process has an indentation depth and equivalent flat-punch indenter radius of 35% and 100% of the sample thickness respectively, and the width of the cell relative to the indenter radius means that it cannot be considered to be a semi-infinite substrate.

In order to analyse the data subject to boundary and substrate effects, for example, when ideal conditions are not met, a three-dimensional (3D) single-cell and disk model based on the finite element (FE) method is developed in this chapter using the commercial simulation software Abaqus to perform simulation experiments. The work in this chapter is divided into three parts.

First, a 3D cylinder model was created with a width and thickness more than 10 times the radius of the indenter and the flat-punch indenter was used to perform an indentation simulation to determine whether or not the principle described

by Chen and Lu when modifying the Sneddon flat-punch contact model for a non-step loaded viscoelastic material could correctly describe the relaxation process under near ideal conditions[26, 204].

Secondly, several flat-end indenters with different bottom surface shapes but the same bottom area were created. The influence of the shape of the bottom surface on the measured values and the feasibility of replacing an irregular bottom surface with a circular one of the same area were verified.

Finally, two 3D cell models, termed the well-spread and less-spread models, have been developed based on the typical cell morphologies encountered in the experiments. These models were used to investigate the trends in the measured and real values of cell indentation experiments under combined effects. The applicability of the previous experimental approach is summarised and a calibration model for the measured values is provided for the two types of cells. In addition, cylinder models corresponding to the thickness and material of the two types of cells are developed to analyse the boundary effects and the influence of basal effects.

## 6.2. Methodology

### 6.2.1. FEA model validation for flat punch indentation

#### 6.2.1.1. Substrate effect validation

As previously stated, the modified Sneddon model is only applicable to an infinite half-space where the indentation depth and flat-punch indenter radius are much smaller than the thickness of the sample being measured. However, in a finite element simulation we cannot create an ‘infinite’ number of parts. Therefore, cylinders of different thicknesses have been created in this study to verify the effect of sample thickness and indenter radius on simulation results during flat punch indentation.

The radius of the indenter is set to 7 μm and the radius of the cylinders is 100 μm, which is an order of magnitude larger than the indenter radius and allows boundary effects to be ignored. The thickness of the cylinders is 1.54 (the thickness of well-spread cells), 2.74 (that of less-spread cells), and 5, 10, 15, and 20 times the radius of the indenter. The indenter is much stiffer than the cell, and so the discrete rigid definition is used to create the indenter component. The use of discrete rigid allows for the custom division of the mesh and helps in solving convergence problems with larger indentations. All indenters in the latter section are the discrete rigid type.
In order to reduce the scale of computation in the simulation, only one-quarter of the cylinder and one-quarter of the cells were simulated.

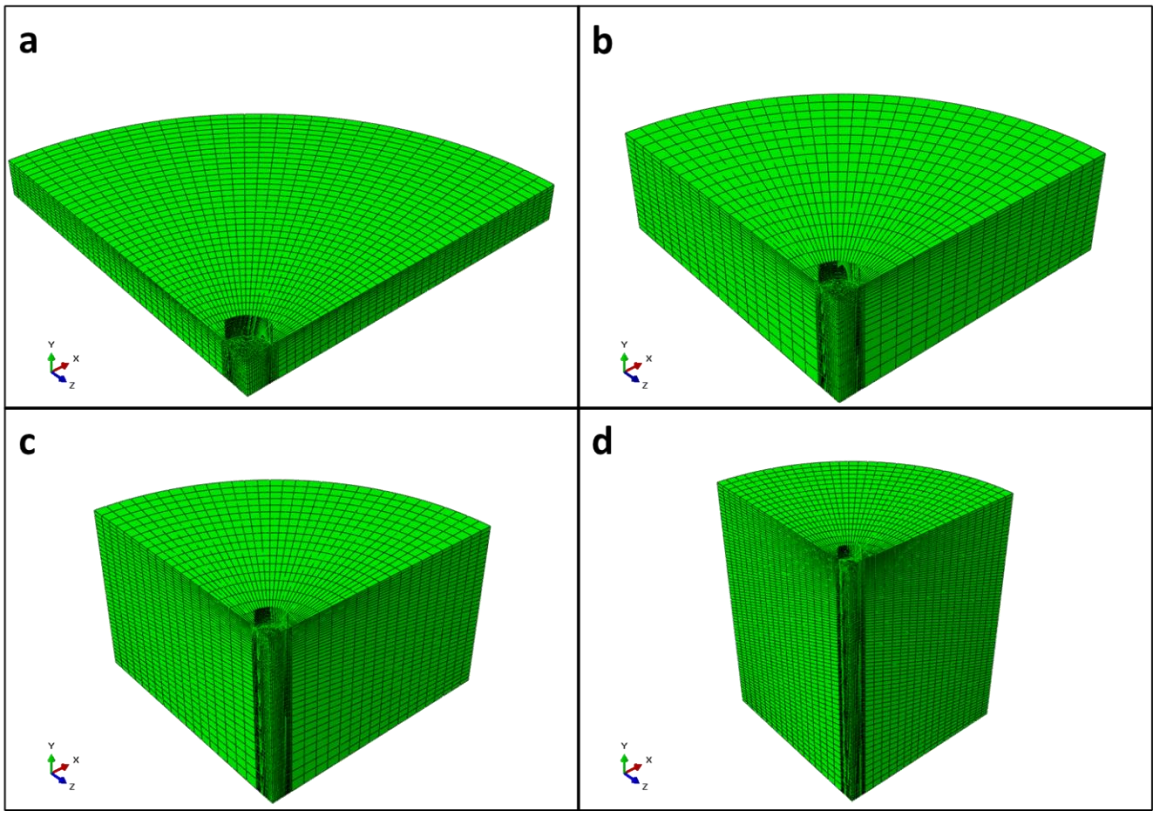


Figure 6-1. Schematic diagram of the indenter and cylinders with thicknesses of: (a) 1.54 times, (b) 10 times, (c) 15 times, and (d) 20 times the radius of the indenter. The mesh for the parts in contact with the indenter is refined, especially the fillet of the indenter, and coarse spaced meshes are used for the other parts in order to reduce the computation required.

The cylinders are made of a structure of hexahedral elements with the standard 3D stress quadratic element type (C3D20H). They are meshed with a subdivision of the contact area and a larger mesh for the rest of the cylinder for the non-critical areas. In the process of meshing the indenter, the part near the edge is subdivided and the rest of the cylinder is subdivided at a larger size. The different levels of coarseness of the meshing for different regions helps to reduce the time required for calculation and increases efficiency, which also ensures better calculation accuracy. A mesh sensitivity analysis was conducted, and the results can be found in the appendix, see Figure S 7 and Figure S 8.

#### 6.2.1.2. Indenter with different geometries

In the previous sections, irregularly shaped contact areas were replaced with circular shapes of equal area, thus obtaining equivalent radii, and the contact model of flat punch was used in the analysis of data to calculate the viscoelastic parameters of the cells.

Here a set of indentation simulations have been created with different shapes of the same base area. Differences in force profiles are then compared to determine the effect of the indentation results on the shape of the indenter and to verify the feasibility of the data analysis using equivalent circles as a replacement as proposed in the previous section.

The radius of the flat-punch indenter is set to 7 μm, while the other indenters retain the same bottom area as that of the flat-punch indenter. The fillet radius of 0.5 μm is an order of magnitude smaller than the indenter radius, so the difference in area due to the presence of the fillet can be ignored.

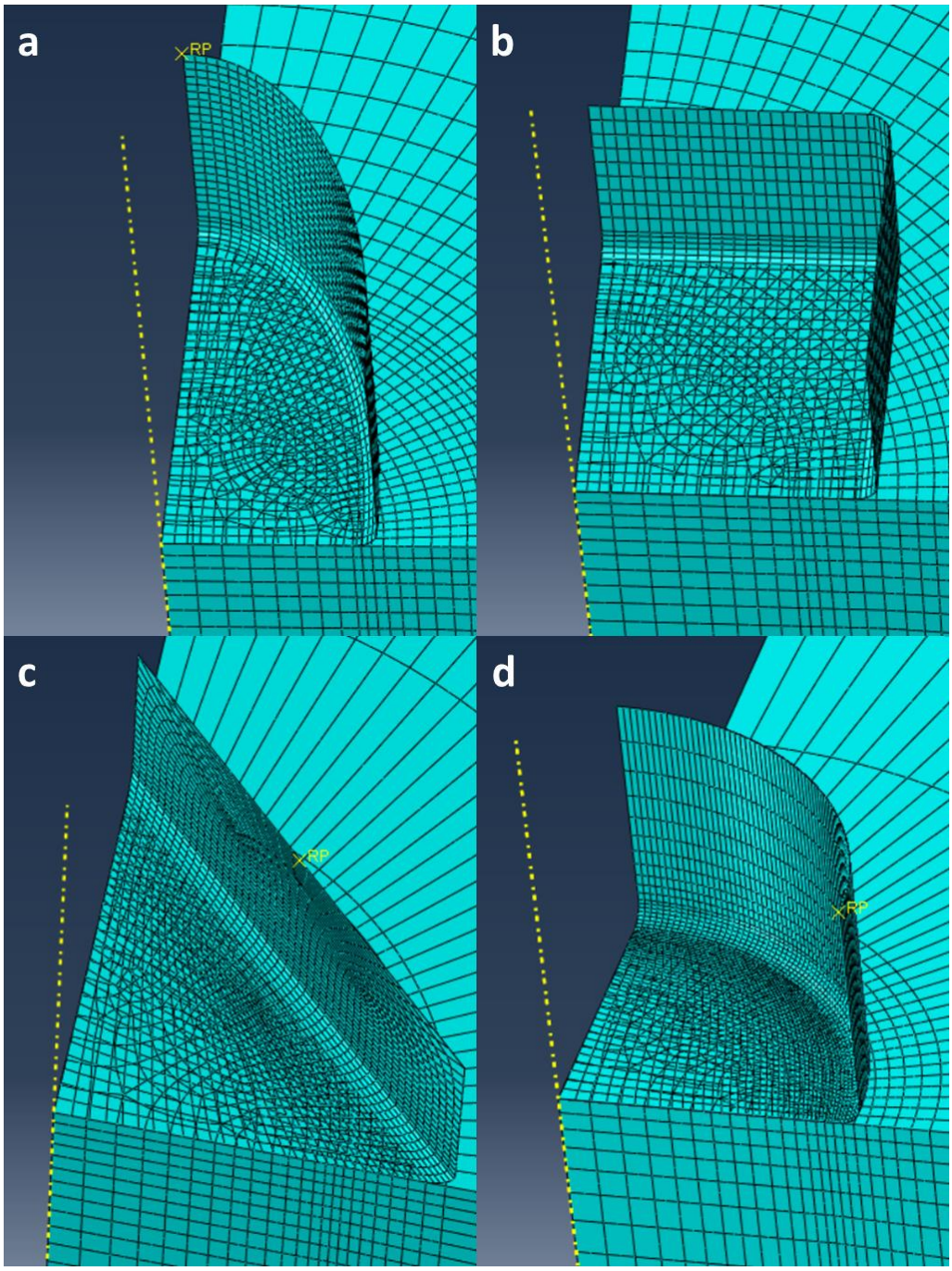


Figure 6-2. The four different bottom shapes of the indenters: (a) ellipse; (b) square; (c) diamond; (d) round. The elliptical and square parts are integral, but the contact with the cylinder is also quartered symmetrically about the centre.

## 6.2.2.FE model for indenting the cells

The practical measurement experiments for indentation on cells do not satisfy the conditions assumed by Equation 3.29. Therefore, the apparent viscoelastic parameters of the cells must be affected by various factors, in particular by the substrate effect, the finite width effect, and cell surface slope and 3D structure effects, as shown in Figure 6-3.

In order to investigate the difference between the flat-punch indentation measurements and the actual values of the apparent viscoelastic parameters of the cells under the combined influence of various factors, two common cell models were constructed for the flat-punch indentation simulation experiments. The two cell models are the well-spread cell in the shape of a flying saucer and the less-spread cell in the shape of a spindle.

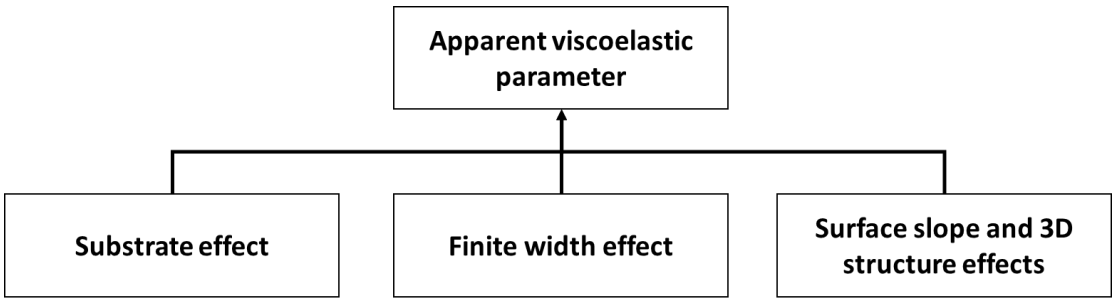


Figure 6-3. The measured apparent viscoelastic parameters of the cell are mainly influenced by the substrate effect, finite width effect and cell surface slope, and 3D structure effects, which correspond to practical conditions that do not satisfy the infinite thickness, infinite width and flat surface conditions of infinite half-space assumed by the flat-punch contact model.

The cell models are all abstracted and simplified by confocal imaging of the 3D cell map to obtain their geometric features.

The less-spread cells, which are spindle-like and have a complex geometry, cannot be sketched with the sketching tools built into ABAQUS. Therefore, the geometry was generated using SolidWorks software. The top, bottom, left, right and front views of the cell outlines were first extracted from the 3D cell images and then sketched to generate the geometry of the spindle by using the software's sweep function, as shown in Figure 6-4 and Figure 6-5. Finally, it was imported into ABAQUS as a less-spread cell part.

The well-spread cell is reduced to a model part in the shape of a flying saucer. From the front cross-sectional views of the 3D image of the cell, the outline of the cell is sketched, then deformable-solid-evolution is used to obtain the part, as shown in Figure 6-6.

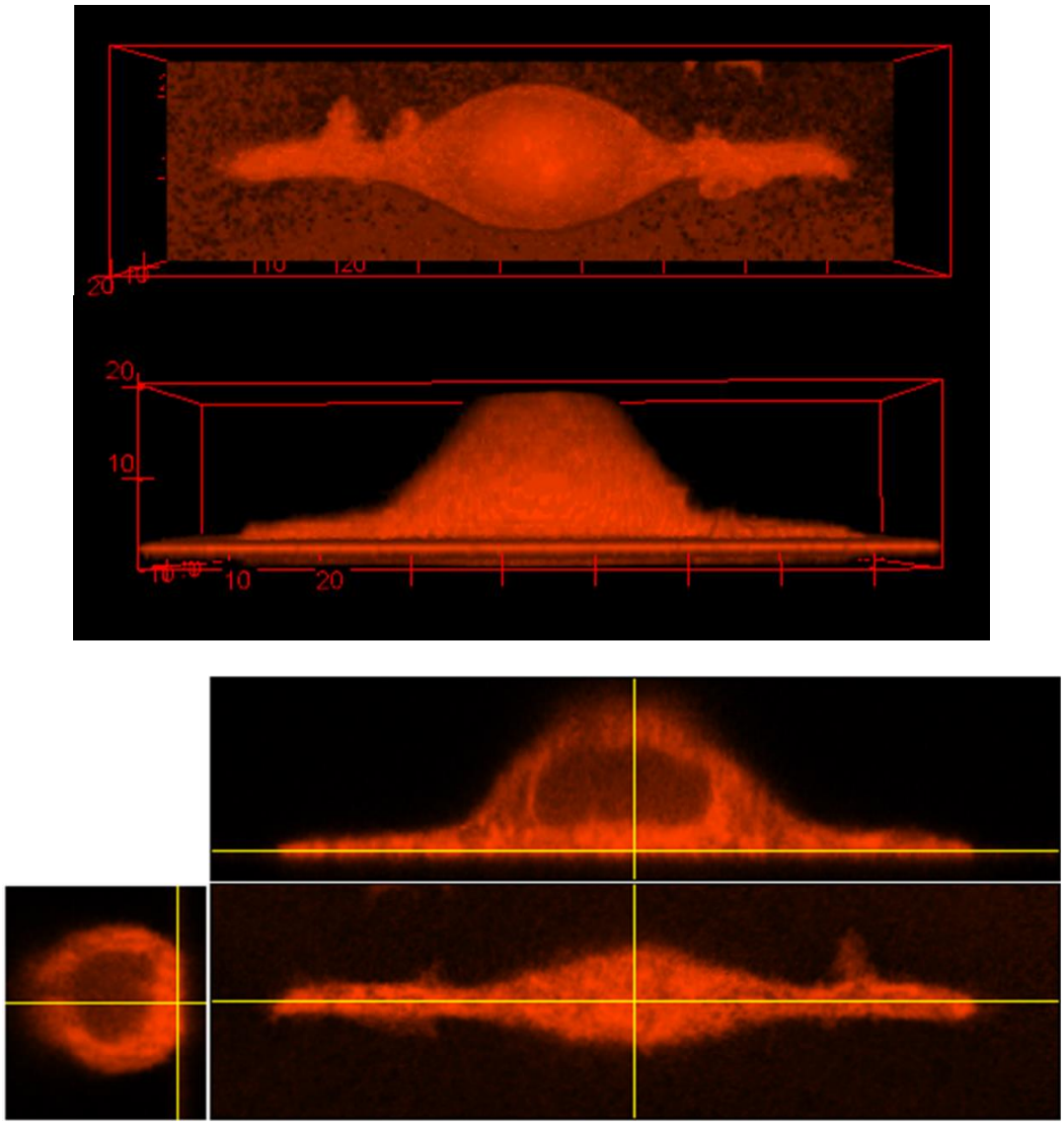


Figure 6-4. A 3D image of the cell is firstly constructed from the confocal image and then several sections are cut out from the 3D image of the cell for sketching. Examples are given here for the front, left and bottom contact surfaces of the cell, with the yellow lines showing the positions of the sections.

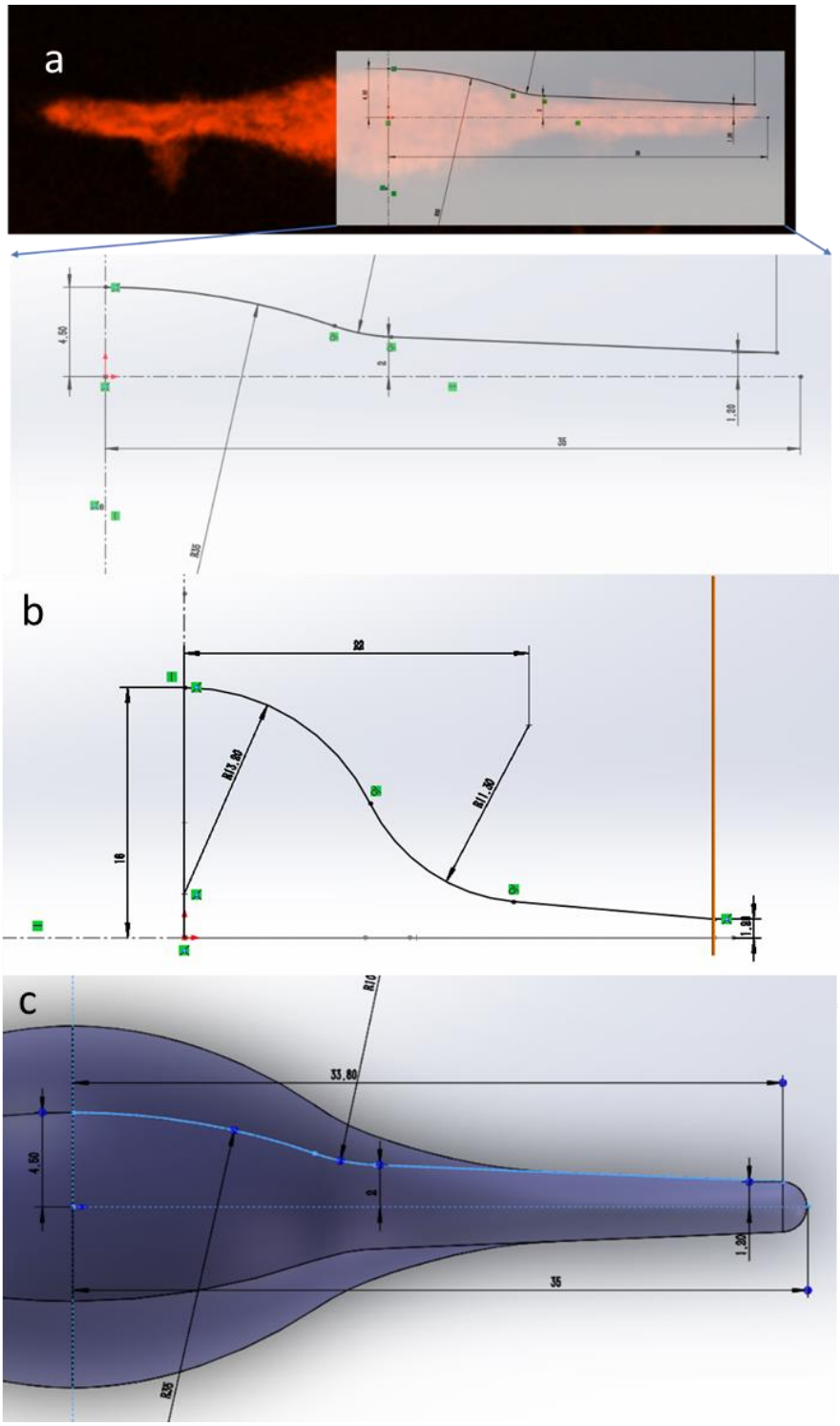


Figure 6-5. Schematic diagram of the steps in the development of the less-spread cell model using cross-sectional views of the cell using SolidWorks: (a) bottom cell profile sketched based on the bottom cross-section; (b) front view cell profile sketched based on the front view cross-section (c) top view cell profile sketched based on the top view cross-section.

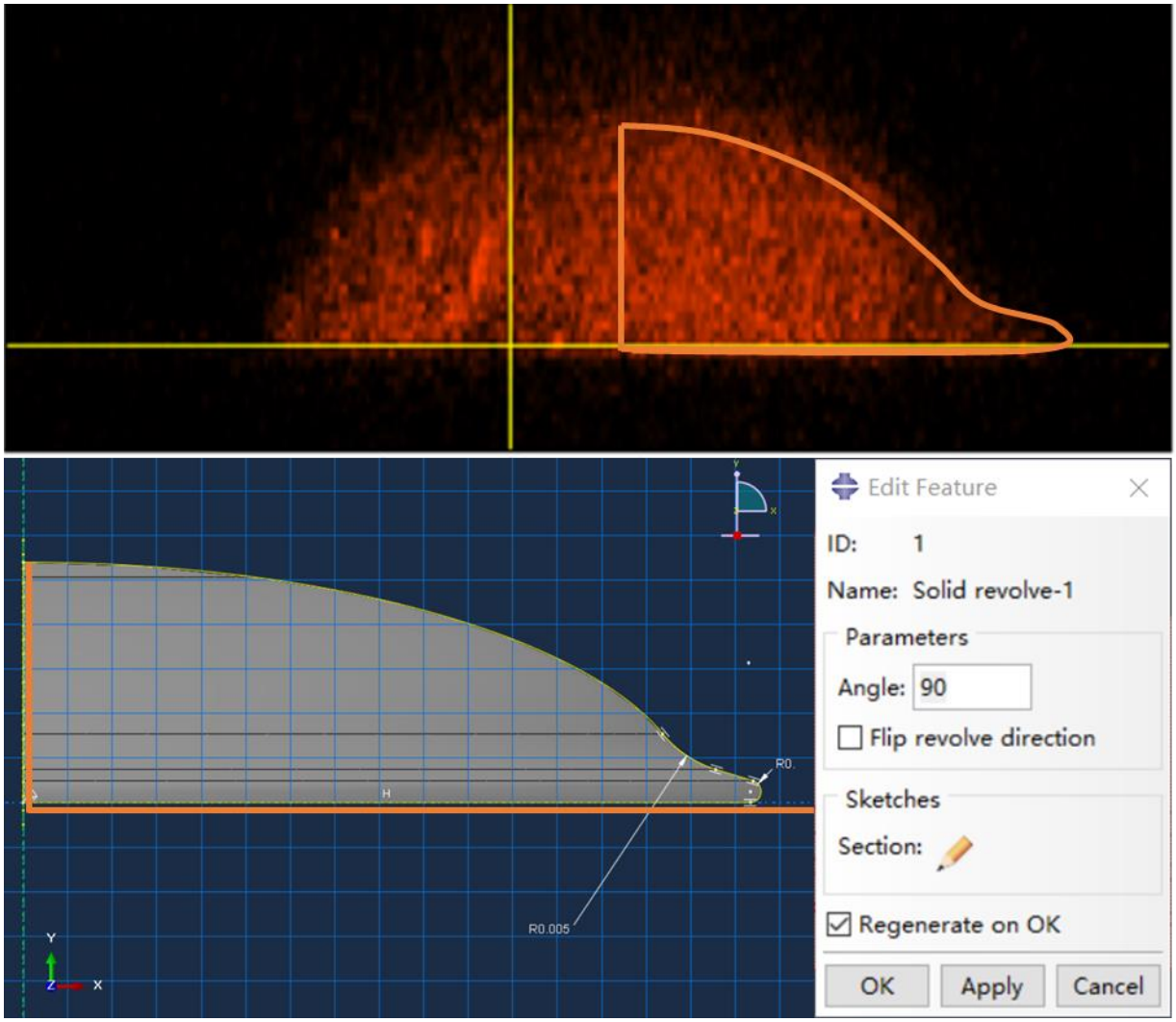


Figure 6-6. Outline of the front view of the less-spread cell sketched using the sketch function in ABAQUS software and then rotated by 90 degrees around the central axis to obtain a simplified model part of the less-spread cell.

#### 6.2.2.1. Mesh for cells

The mesh of cells is made of free tetrahedral elements with the standard 3D stress quadratic element type (C3D4). The cells are meshed by subdividing the contact area and meshing the non-critical areas of the rest of the cell at a larger size. During the meshing of the indenter, the parts close to the edges are subdivided, while the rest of the cell is subdivided at a larger size. Meshing the

different areas at different thicknesses helps in reducing the computation time required and increasing efficiency, which also ensures better computational accuracy.

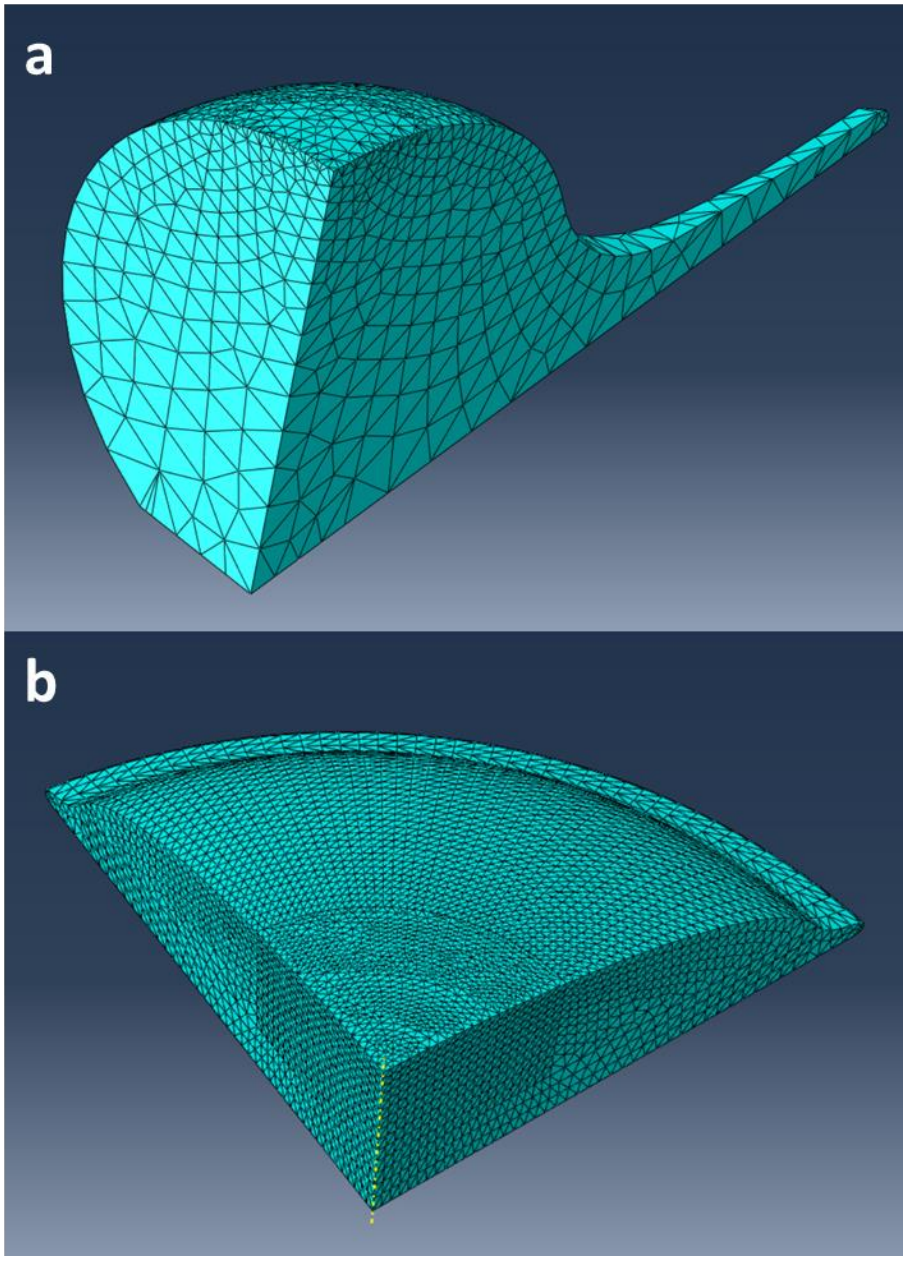


Figure 6-7. Meshes of: (a) well-spread cell, and (b) less-spread cell.

#### 6.2.2.2. Thin layer cylinder as comparison

Under non-ideal conditions, the thickness, width, and morphology of the indentation object will all have an effect on the indentation results. In order to investigate the tendency of two typical cell morphologies to affect those results, thin layer cylinders were created which have different radii but the same thickness for comparison.

The first group of cylinders have almost infinitely large lateral size in order to remove lateral boundary effects (see Figure 6-8). The group with the same height and width allow the removal of the effects of both the lateral boundary and the substrate, with only the effect of morphology remaining (see Figure 6-9).

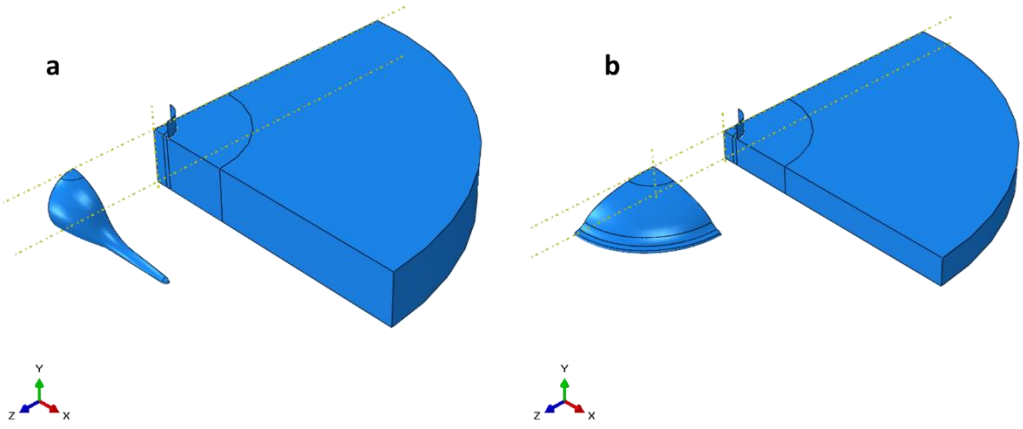


Figure 6-8. Cylinders with a 100 μm radius, which have the same thickness and material properties as the corresponding cell models and can be regarded as having infinite horizontal width: (a) well-spread cell with the same thickness of cylinder; (b) less-spread cell with the same thickness of cylinder.

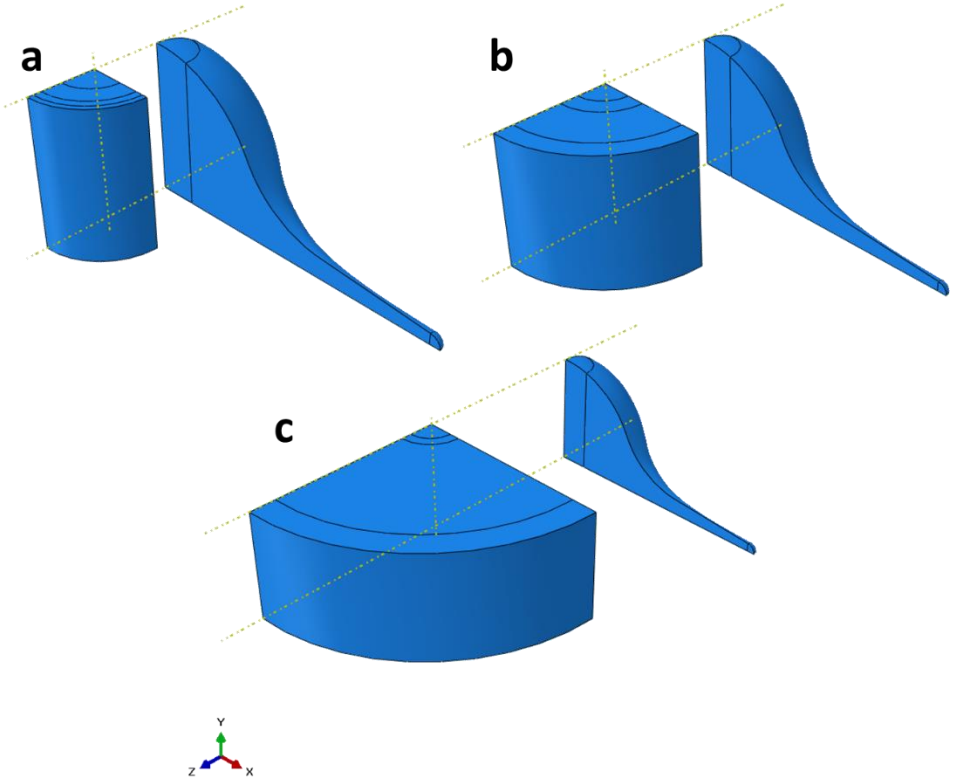


Figure 6-9. Model of cylinders of the same thickness as the less-spread cells but different radii of: (a) the length of the short axis of the cell; (b) the length of the central body of the spindle; (c) the length of the cell.

### 6.2.3. Boundary conditions and other configurations

Horizontal displacement and all of the directional rotations of the indenter are restricted to 0, while the indenter moves down 1 μm in the vertical direction following the amplitude, and the indentation depth and speed can be defined in the Amplitude setting. In different simulations, different indentation depths were used and the time point was set so as to maintain an indenter loading speed of 1 μm/s.

For the one-quarter cylinders and cells model, elements on the plane of symmetry can only be moved in the plane of symmetry and any rotation

perpendicular to this plane is prohibited. Furthermore, the elements on the bottom of the model can only be moved in the horizontal direction and any rotation perpendicular to it is prohibited.

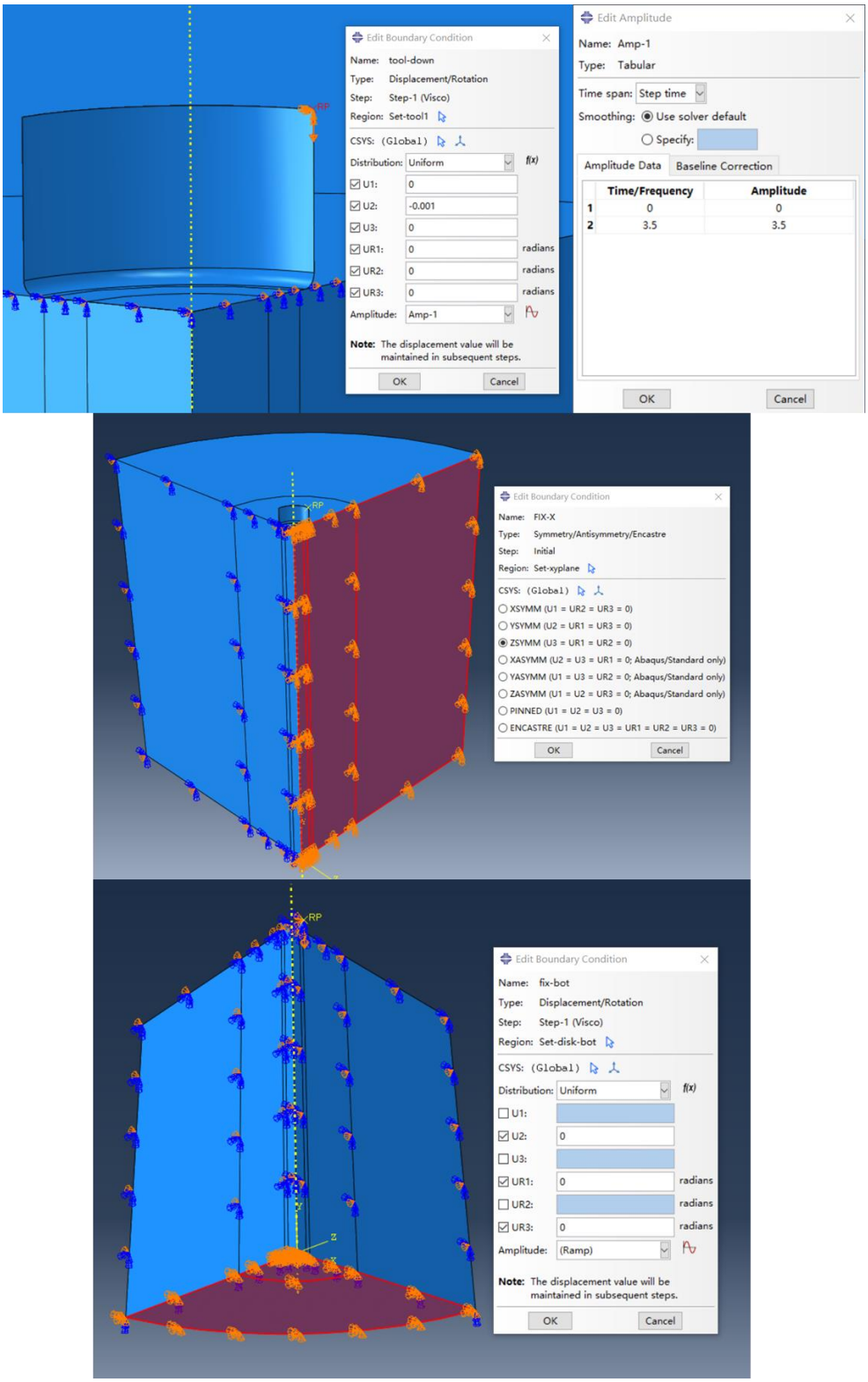


Figure 6-10. Boundary conditions of the indenter and cylinder. Only the boundary conditions for the flat-punch indenter and the cylinder model are shown; the boundary conditions for the other shapes of the indenter and the two quarter-cell models are the same as theirs.

As mentioned in Chapter 1, a variety of methods exist for the modelling and simulation of cell mechanics according to different theoretical bases. Consistent with the work described in Chapters 4 and 5, the focus here is on the viscoelastic modulus data of the cell for the AFM force-distance curve experiments, and so a continuous solid model is adopted for the simulation which assumes the cell to be made of an incompressible, isotropic and homogeneous linear elastic material. The specific parameters were averaged over the viscoelastic parameters of the two morphologies of cells experimentally obtained in Chapter 4.

The cellular material is assumed to be incompressible, and the Poisson's ratio of the material is set at a maximum of 0.49 in ABAQUS. Therefore, the Poisson's ratios of both cellular materials were set at 0.49.

Time–Prony section was used to define the materials representing well-spread cells and less-spread cells, and the parameters are equal to the value in Chapter 4, shown in Table 6-1. For cylinders in the validation section, the material is the same as that of the less-spread cells.

Table 6-1. Input material parameters for different cell models in ABAQUS

| | Less-spread cell | Well-spread cell |
|---|---|---|
| Equilibrium modulus $E_\infty$ (Pa) | 210 | 210 |
| Time constant $\tau_1$ (s) | 0.10 | 0.06 |
| First Maxwell arm modulus component $g_1$ | 0.8167 | 0.7877 |
| Time constant $\tau_2$ (s) | 0.61 | 0.55 |
| Second Maxwell arm modulus component $g_2$ | 0.068 | 0.1132 |
| Poisson's ratio | 0.49 | 0.49 |

The indenter downward press is a large deformation simulation and the parameter Nlgeom (nonlinearity geometric) should be set to On in the Step function module. A 10-second Visco-type step was created in the Steps with an automatic 0.01 second maximum and initial increment size, and a 1E-6 second minimum increment size. The creep / swelling / viscoelastic strain error tolerance is 0.04, and integration is explicit / implicit.

During interaction, the indenter is in contact with the cell surface and the cell bottom is in contact with the substrate, and the interactions need to be defined. The contact is divided between the indenter and the cell / cylinder surface into two parts according to the indenter bottom surface (bottom flat and fillet area), because the output contact area is based on a certain interaction and separating the contact between the indenter and the cell facilitates the output of the contact area between the indenter bottom surface and the cell / cylinder. Rigid parts are the master surface, while deformable parts are the slave surface. Interaction properties for indenter bottom – cell /

cylinder, indenter side – cell / cylinder and substrate - cell / cylinder are the same, being frictionless in tangential behaviour and ‘Hard’ contact in normal behaviour.

The field output focuses on the visualization of the simulation, and so stress, strain and the displacement of the whole model are the output variables. Meanwhile, the history output focuses on the force-displacement curves and contact area between the cantilever and cells recorded in the experiments, and therefore the force displacement and force in the vertical direction of the indenter and the contact area between the indenter bottom and the cell / cylinder are the output variables.

## 6.3. Results and discussion

### 6.3.1. Validation of the modified Sneddon model for viscoelastic material under substrate effect

#### Modified Sneddon model validation

As described in Section 6.2, cylinders with varied thicknesses were indented, using a flat punch indenter with a radius of 7 μm, to a 3.5 μm depth at a rate of 1 μm/s. This was followed by a stress relaxation period of 6.5s. The thickness and width of the cylinder models are one order of magnitude greater than the radius of the indenter, which could be considered as infinite half spaces. The force on the indenter in the vertical direction during the whole process was monitored, as shown in Figure 6-11. Data analysis is applied on the relaxation force curve to calculate the measured viscoelastic parameters, and these

parameters are normalized to the actual values (input parameters), as shown in Figure 6-12.

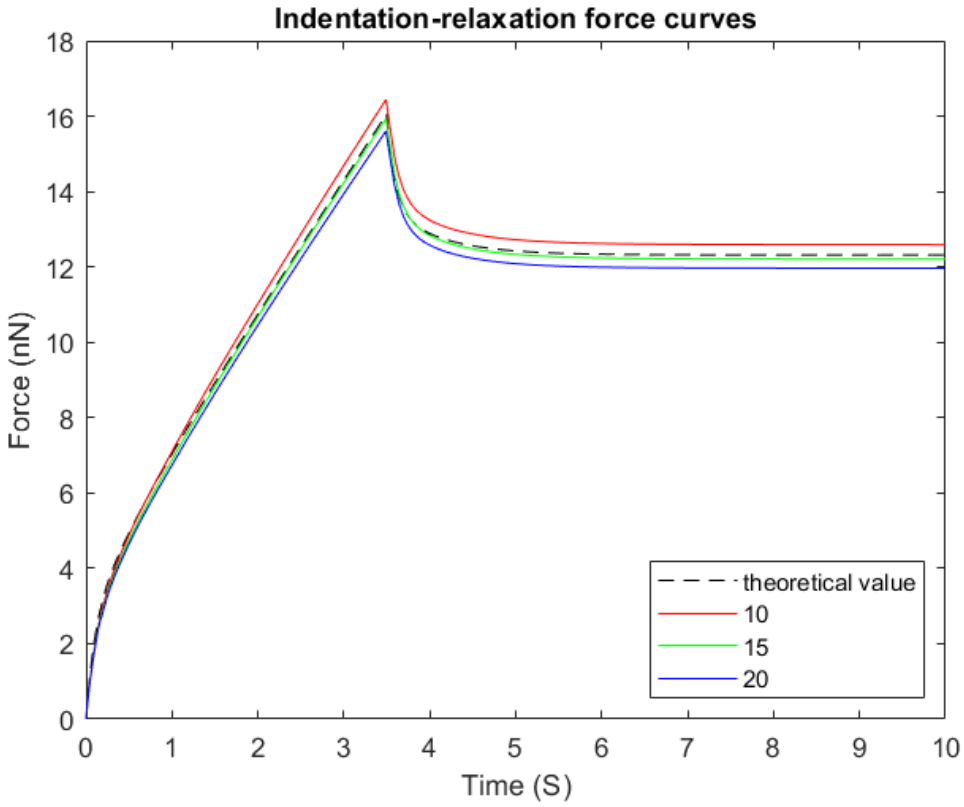


Figure 6-11. Force-time curves for indentations of cylinder models with thickness 10, 15 and 20 times as indenter radius. The theoretical curve calculated from Equation 3.29 is also shown as the black dashed line and used for comparison.

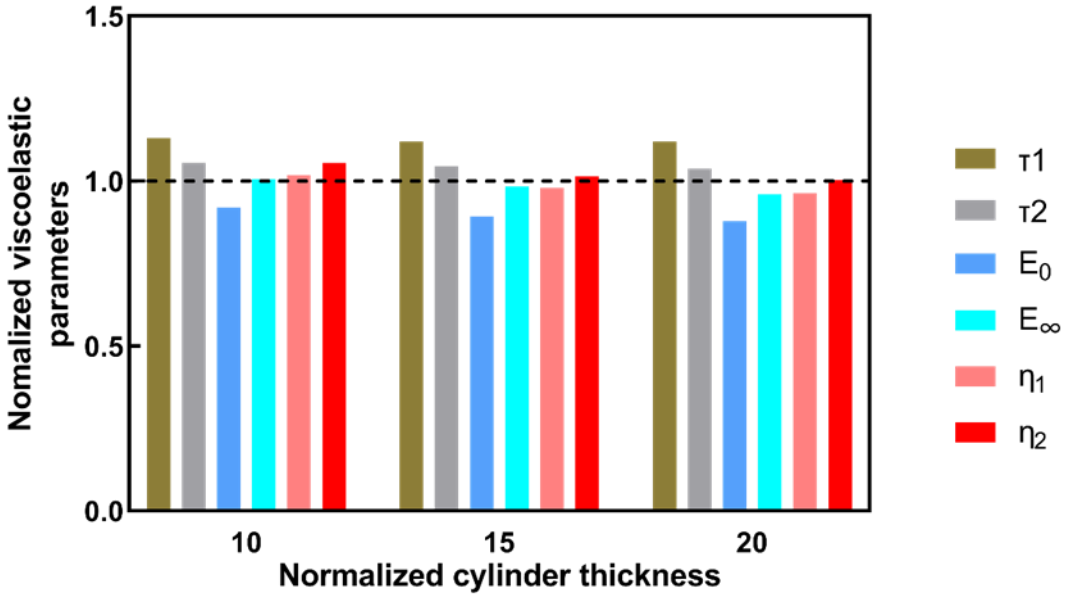


Figure 6-12. Apparent viscoelastic parameters for cylinder models with thickness 10, 15 and 20 times as indenter radius, which have been normalized to the actual values.

As shown in Figure 6-12, the force curve is closest to the theoretical value when the cylinder thickness is 15 times the radius of the flat punch. At 10 and 20 times the radius of the indenter, the force on the indenter is greater and less than the theoretical value, with a difference of less than 5%. It is assumed that the difference between the theoretical and measured force values is due to the rounding of the bottom edge of the indenter.

From Figure 6-12, except for the apparent time constant of the first Maxwell-arm τ1 and equilibrium modulus E0 which are 112% and 90% of their actual values respectively when the model thickness reaches 10 times the indenter radius, all other apparent viscoelastic parameters differ from the actual values to within 5%. The variation of these parameters is less than 4%, therefore it can be considered that when the model thickness is greater than or equal to 10 times the indenter radius, the effect of the substrate effect is small, and the

apparent viscoelastic parameters of the model no longer vary with the model thickness.

The Modified Sneddon model has been validated to accurately predict the indentation-relaxation process of viscoelastic materials under ideal conditions and can also be used to perform data analysis of the force curves of the relaxation and to calculate the viscoelastic parameters of the material.

**Substrate effect for the flat punch indentation**

To further investigate the substrate effect, indentation was performed on smaller thickness models of cylinders to observe the changes in the vertical force on the indenter and apparent viscoelastic parameters.

Cylinders with thicknesses of 1.54 times, 2.74 times and 5 times the radius of the indenter were used, where the first two were equal to the thickness of the well-spread cell and well-spread cell respectively.

In this study, only rigid substrates are considered for simulation. In fact, in order to simulate cell growth on PDMS surfaces with different stiffness, a solid with viscoelastic parameters close to those of PDMS should be employed as substrates, rather than just a rigid substrate. This updated work will be developed in the future.

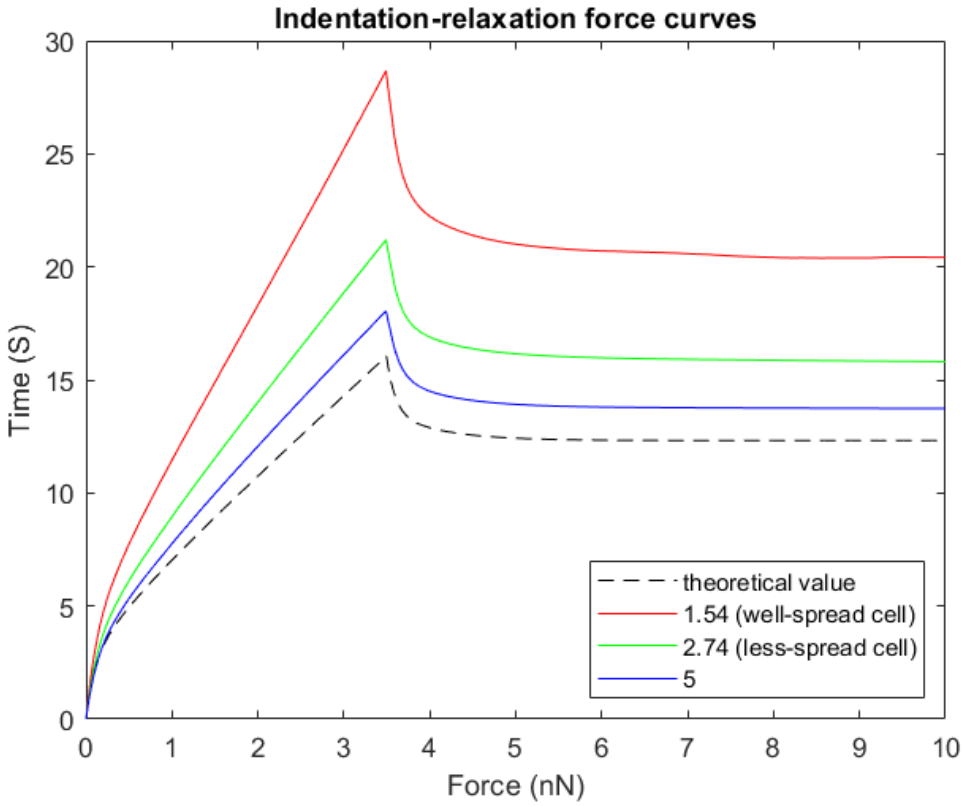


Figure 6-13. Force-time curves for indentations of cylinder models with thickness 1.54 (same as well-spread cell), 2.74 (same as less-spread cell) and 5 times as indenter radius. The theoretical curve calculated from Equation 3.29 is also shown as a black dashed line and used for comparison.

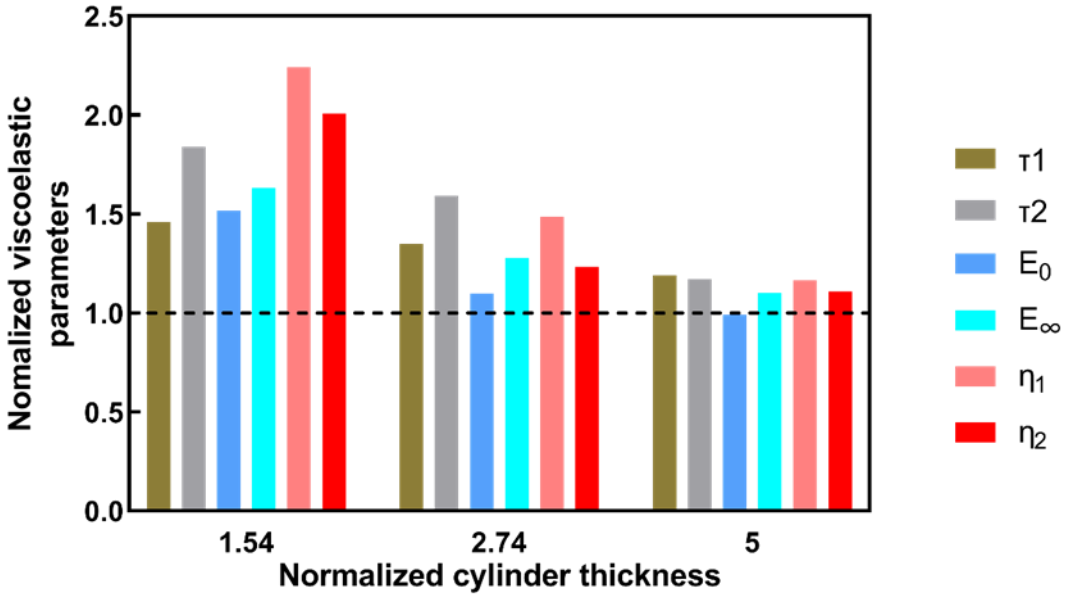


Figure 6-14. Apparent viscoelastic parameters for cylinder models with thickness 10, 15 and 20 times as indenter radius, which have been normalized to the actual values.

As the thickness of the cylinder decreases, as the substrate effect gradually becomes non-negligible, the force increases in the resultant of the substrate effect. At a cylinder thickness 1.5 times as the radius of the flat punch, the force curve is about twice the theoretical value.

This theoretical equation is suitable for predicting indentation and relaxation processes in viscoelastic materials under near ideal conditions, or for calculating viscoelastic parameters from force relaxation processes in materials. However, when the thickness of the sample is not large enough compared to the radius of the indenter, the substrate effect makes the vertical force obtained from indenter measurements to be larger and affects the analytical results.

### 6.3.2. Verification of the effect of different base shapes on the flat bottom indenter

Flat-end indenters of different shapes with the same bottom area were used to perform indentation on the cylinder, applying a 3.5 μm indentation depth at a speed of 1 μm/s and then holding the displacement to allow the viscoelastic material to relax. The forces on the indenters in the vertical direction were recorded throughout the process as well as the contact area between the indenter and the cylinder in order to ensure that the contact area remained essentially the same.

For different shapes of indenter, the force results of indentation vary within 5% for the same bottom area. Converting an indenter to another different shape with the same bottom area results in nearly same force. Therefore, it is feasible to equate the radius R (used in the formula for calculating the modulus by means of the F-curve) of the contact area with a circle of the same area in the methodology of the previous experiment.

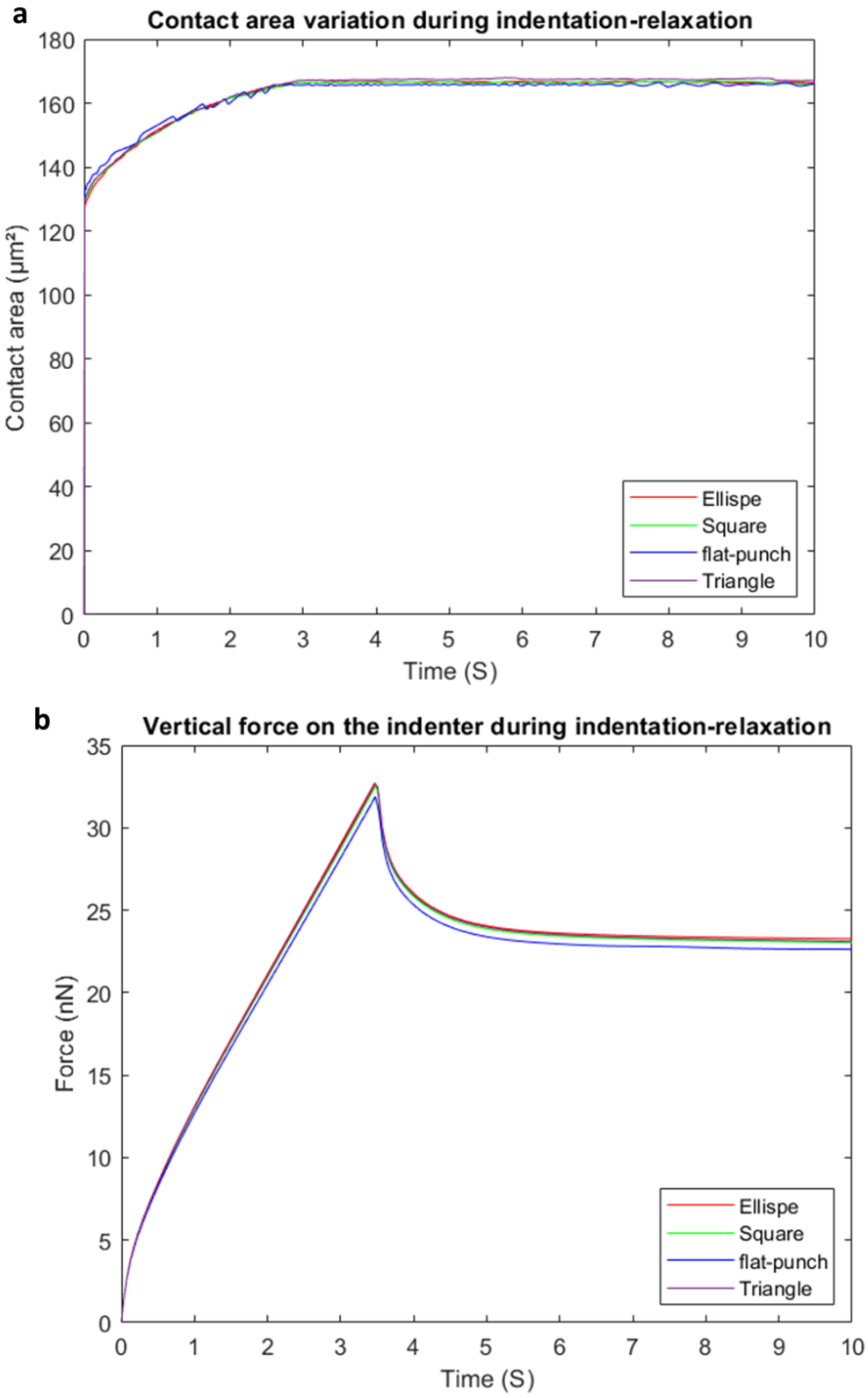


Figure 6-15. Indentation on cylinder models with different indenter shapes for an indentation depth of 3.5um as in previous simulations: (a) vertical force on the indenter; (b) contact areas between indenter and cylinders.

### 6.3.3. Effect of cellular morphology on the measurement of the viscoelastic modulus of cells

As described in Section 2.2, in order to investigate the difference between the apparent observations and the actual values of the viscoelastic parameters of the two cell models, a flat-punch indenter was first used to indent the two cells so as to quantify the variation in apparent cellular viscoelastic parameters at different indentation depths.

Next, variables were controlled to isolate the factors which affect the apparent cellular viscoelastic parameters and to explore the magnitude of each factor's contribution in affecting those parameters.

Due to differences in the production process, the cantilever as an indenter has edges with fillets of variable radius, which may also affect the apparent viscoelastic parameters, and indenters have been used with different fillet radii of 0.5 μm and 0.1 μm. The smaller corner radii are too sharp and cause convergence problems in the ABAQUS simulation, which cannot be run smoothly when the indentation depth is large. Therefore, only some of the data points with small indentation depths were used in the control group for the small fillet half warp in order to compare the effect of fillet radius on the results.

The measured apparent values of the viscoelastic parameters of the two cell shapes were normalised to their real values by calculating the ratio of the measured values to the true values at different indentation depths.

#### 6.3.3.1. Less-spread cell

The trends for the variation of the apparent viscoelastic parameters with indentation depth is shown for the spindle shaped less-spread cell. The indentation depth of the less-spread cells in the experiments in the previous two chapters was in the region of 4 to 8 μm, which is about 20% to 40% of the maximum cell thickness, corresponding to the interval indicated to the right of the black dashed line in Figure 6-14.

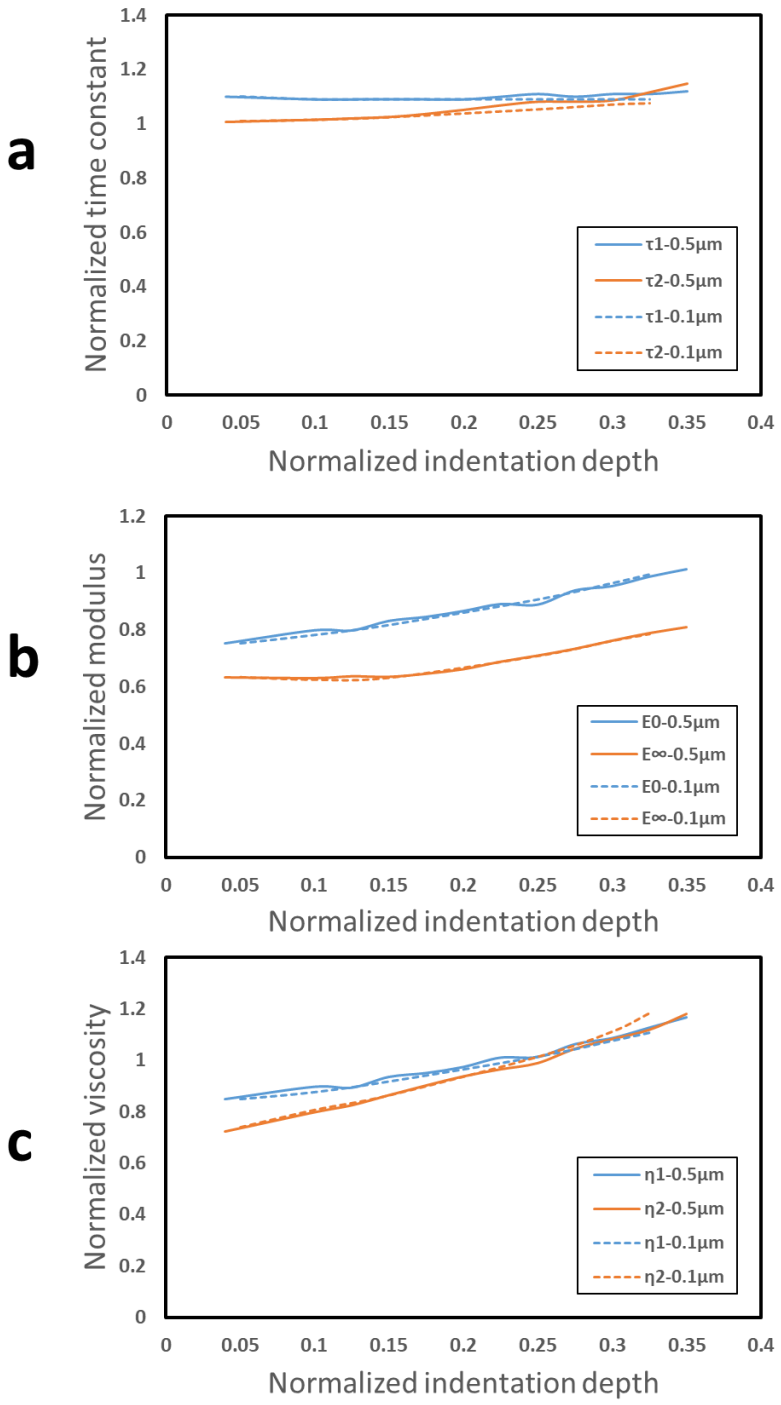


Figure 6-16. Variation in apparent viscoelastic parameters with indentation depth for the less-spread cell model. (a) time constant τ; (b) instantaneous modulus $E_0$ and equilibrium modulus $E_\infty$; (c) viscosity η. The solid curve is the measurement of the 0.5 μm fillet radius indenter, indicated by -0.5μm and the dashed curve is the measurement of the 0.1 μm fillet radius indenter, indicated by -0.1μm.

As shown in Figure 6-16, for the indentation measurements of the less-spread cell model, the time constant is relatively close to the actual value. The first Maxwell arm time constant remains constant, while the second Maxwell arm time constant increases with indentation depth, but in smaller increments, reaching 110% of the actual value at an indentation depth of 35% of the cell thickness.

Both the apparent instantaneous and equilibrium moduli increase approximately linearly with increasing indentation depth. The instantaneous and equilibrium moduli are 75% and 63% respectively of the actual values for an indentation depth of 5% cell thickness and increase to 101% and 81% of the actual values for an indentation depth of 35% cell thickness.

The apparent viscosity of the less-spread cell also increases approximately linearly with increasing indentation depth. The viscosity of the first Maxwell arm increases from 85% to 116% of the actual value as the indentation depth increases from 5% to 35% of the cell thickness. The viscosity of the second Maxwell arm increases from 72% to 118% of the actual value as the indentation depth increases from 5% to 35% of the cell thickness.

In the less-spread cell model, the different values of the radius of the indenter fillet lead to insignificant differences in the measurements.

**Calibration model**

Based on the above simulation results, calibration equations of the apparent viscoelastic parameters against the actual values can be calculated for the spindle-shaped less-spread cell. Since the viscosity parameters can be calculated from the time constant and the instantaneous modulus, only the time constant and modulus calibration equations have been calculated.

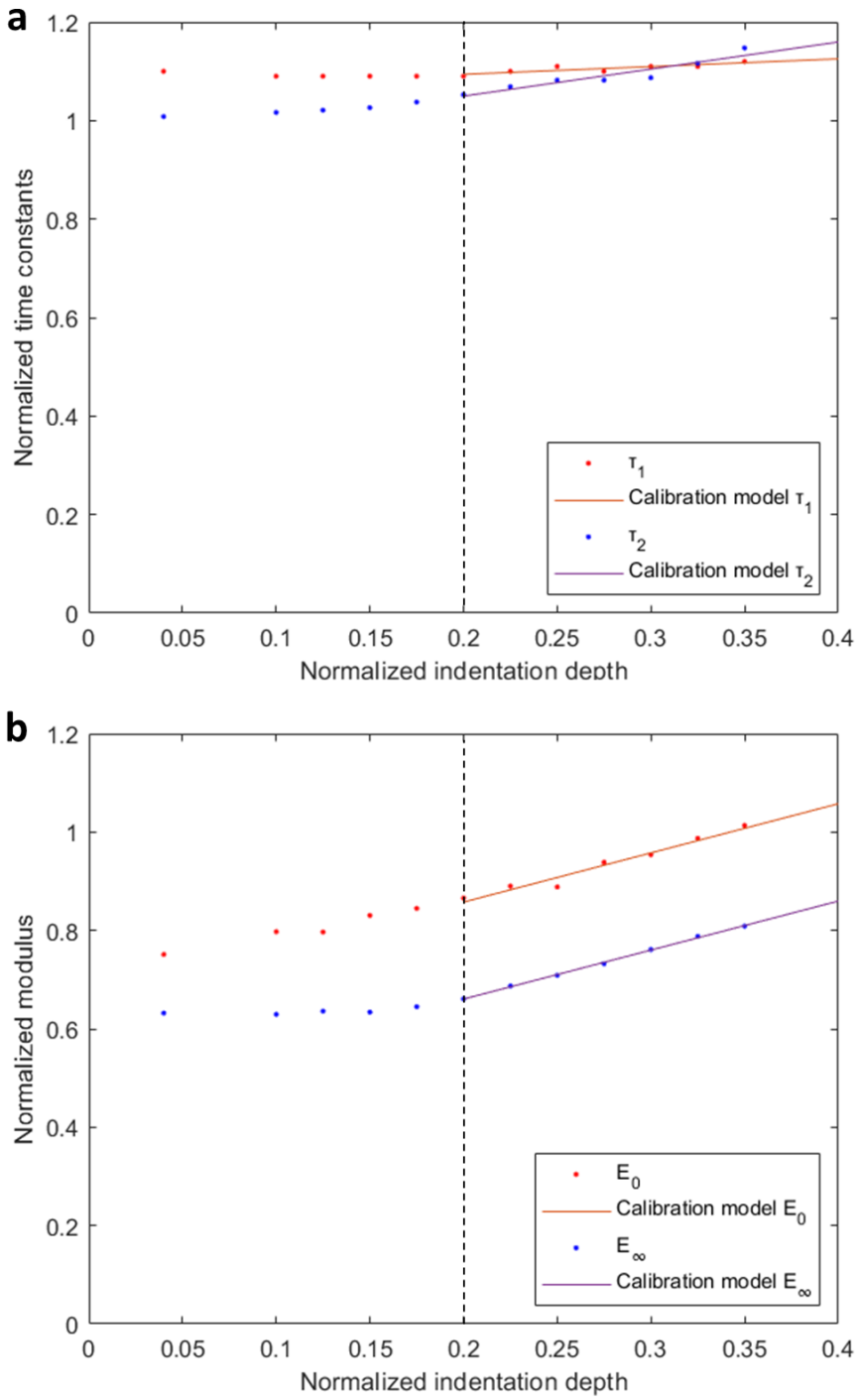


Figure 6-17. Calibration models for the apparent viscoelastic parameters: (a) time constant τ; (b) instantaneous modulus $E_0$ and equilibrium modulus $E_\infty$. Because the indentation depths in the experiments were 20%-40% of the cell thickness, data points with an indentation depth of 20% or more were used for the fitting, represented in the graph as the interval to the right of the black dashed line.

The correction equations for the spindle-shaped less-spread cell model are:

$$\tau_1 = \tau_1^*/(0.15714\,\delta + 1.0625) \qquad R^2 = 0.697$$

$$\tau_2 = \tau_2^*/(0.54986\,\delta + 0.9397) \qquad R^2 = 0.828$$

$$E_0 = E_0^*/(1.0004\,\delta + 0.6577) \qquad R^2 = 0.931$$

$$E_\infty = E_\infty^*/(0.9964\,\delta + 0.4623) \qquad R^2 = 0.991$$

In the above equations, $\delta$ is the normalized indentation depth, the actual values of the viscoelastic parameters are not marked with *, and the apparent values are marked with *.

#### 6.3.3.2. Well-spread cell

The trends for the variation of the apparent viscoelastic parameters with indentation depth is shown for the flying saucer shaped well-spread cell. The indentation depth of the less-spread cells in the experiments in the previous two chapters was in the region of 2.5 to 5 μm, which is about 20% to 50% of the maximum cell thickness, corresponding to the interval indicated to the right of the black dashed line in the Figure 6-17.

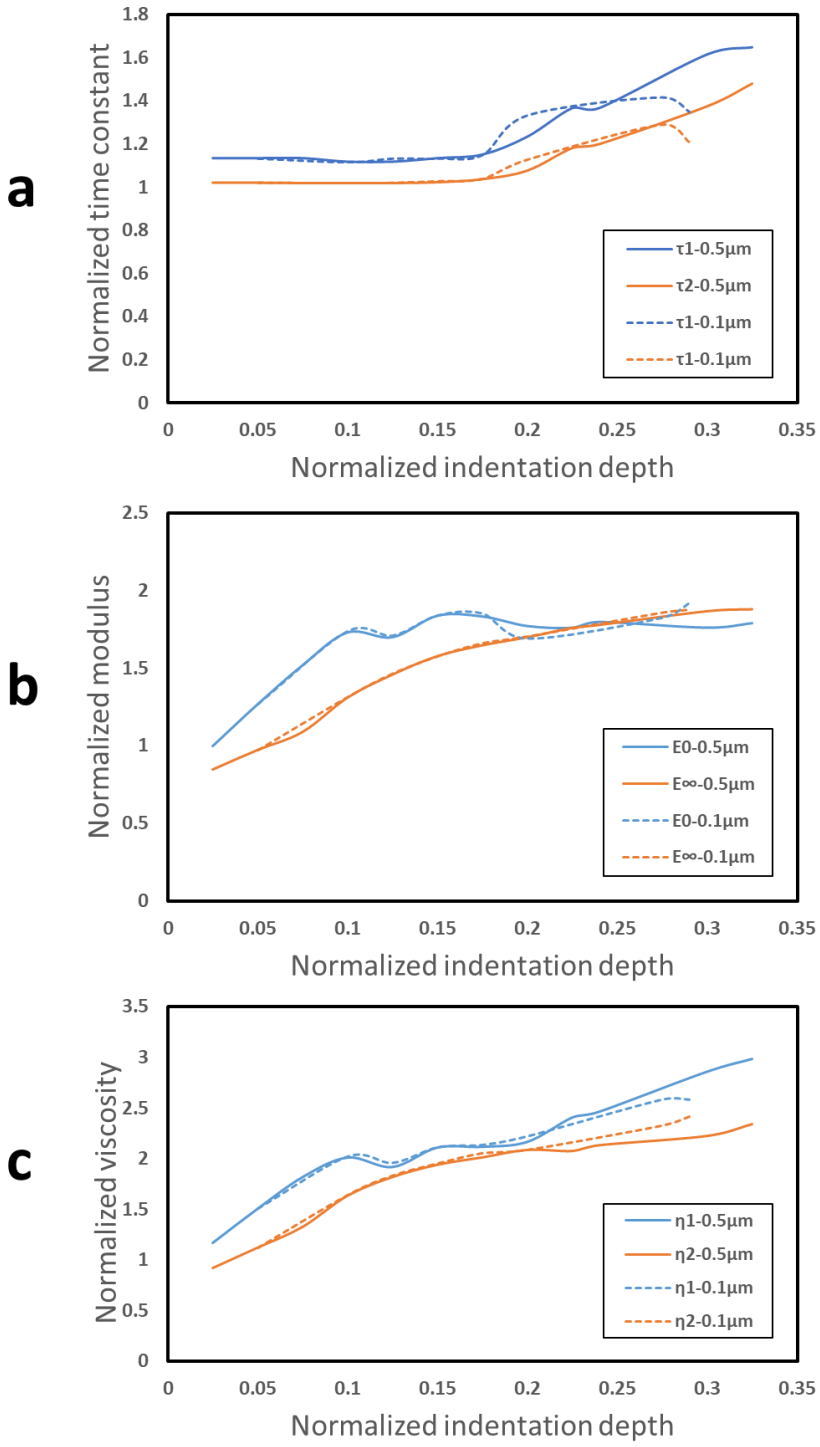


Figure 6-18. Variation in apparent viscoelastic parameters with indentation depth for the well-spread cell model: (a) time constant τ; (b) $E_0$ and equilibrium modulus $E_\infty$; (c) viscosity η. The solid curve is the measurement of the 0.5 μm fillet radius indenter indicated by -0.5μm, and the dashed curve is the measurement of the 0.1 μm fillet radius indenter indicated by -0.1μm.

As shown in Figure 6-18, for the indentation measurements of the well-spread cell model, the time constant is similar to the actual value when the indentation depth is smaller than 18% of the cell thickness. It then starts to rise after the indentation depth exceeds 18% of the cell thickness. The time constants of the first and second Maxwell arms increase to approximately 162% and 147% of the actual value respectively when the indentation depth reaches 35% of the cell thickness.

Both the apparent instantaneous and equilibrium moduli increase with increasing indentation depth. The value of instantaneous modulus increases from 100% of the actual value to 170% from 2% to 10% indentation and then fluctuates around 170%. The equilibrium modulus increases from 85% of the actual value to 158% from 2% to 15% indentation, and then slows down and finally increases to 180% of the actual value when the indentation reaches 35% cell thickness.

The apparent viscosity of the less-spread cell also increases approximately linearly with increasing indentation depth. The viscosity of the first Maxwell arm increases from 117% to 297% of the actual value as the indentation depth increases from 2% to 35% of the cell thickness. The viscosity of the second Maxwell arm increases from 94% to 239% of the actual value as the indentation depth increases from 2% to 35% of the cell thickness.

It is worth noting that the instantaneous modulus and the time constant of the first Maxwell arm in the 0.5 μm fillet radius indenter show large fluctuations in the depth range of 25-30%, and they appear to fluctuate in opposite directions. Thus, the apparent viscosity (the product of the instantaneous modulus and the time constant) does not fluctuate dramatically as the indentation depth

increases. However, similar fluctuations do not occur for indenters with smaller fillet radii.

**Calibration model**

Similar to the previous simulation results for the well-spread cell model, the calibration equations of time constant and modulus can be fitted and calculated.

The correction equations for saucer shape well-spread cell model are:

$$\tau_1 = \tau_1^*/(3.2432\,\delta + 0.6113) \qquad R^2 = 0.984$$

$$\tau_2 = \tau_2^*/(2.7159\,\delta + 0.5698) \qquad R^2 = 0.94$$

$$E_0 = E_0^*/(-0.307\,\delta + 1.8637) \qquad R^2 = 0.387$$

$$E_\infty = E_\infty^*/(1.7712\,\delta + 1.348) \qquad R^2 = 0.928$$

In the above equations, $\delta$ is the normalized indentation depth, the actual values of the viscoelastic parameters are not marked with * and the apparent values are marked with *.

Applying this calibration model to the less-spread and well-spread cell moduli measured in Chapter 4, the results changed from no significant difference to a significantly larger modulus for the less-spread cells than for the well-spread cells, as shown in Figure 6-19.

The corrected results are consistent with the published data[149, 157]. The reason for the greater modulus of less-spread cells compared to well-spread cells is that less-spread cells correspond to metaphase or prophase. The cells change their shape from spread to spherical in order to mitosis, creating a large 'rounding stress' inside the cell[149].

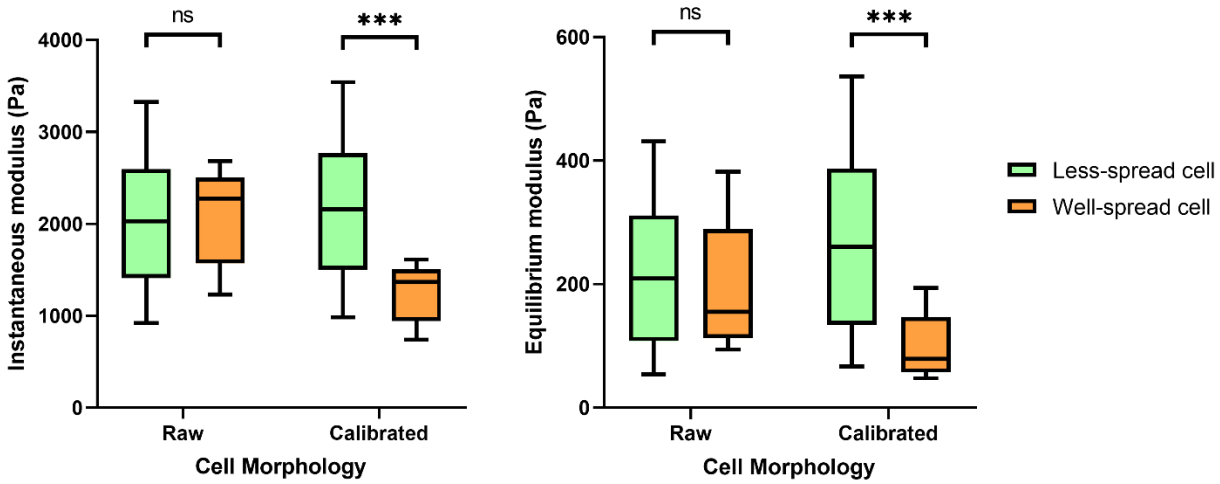


Figure 6-19. Comparison of cell modulus raw data and calibrated data for results in Chapter 4. After calibration, the results changed from no significant difference to a significantly larger modulus for the less-spread cells than for the well-spread cells.

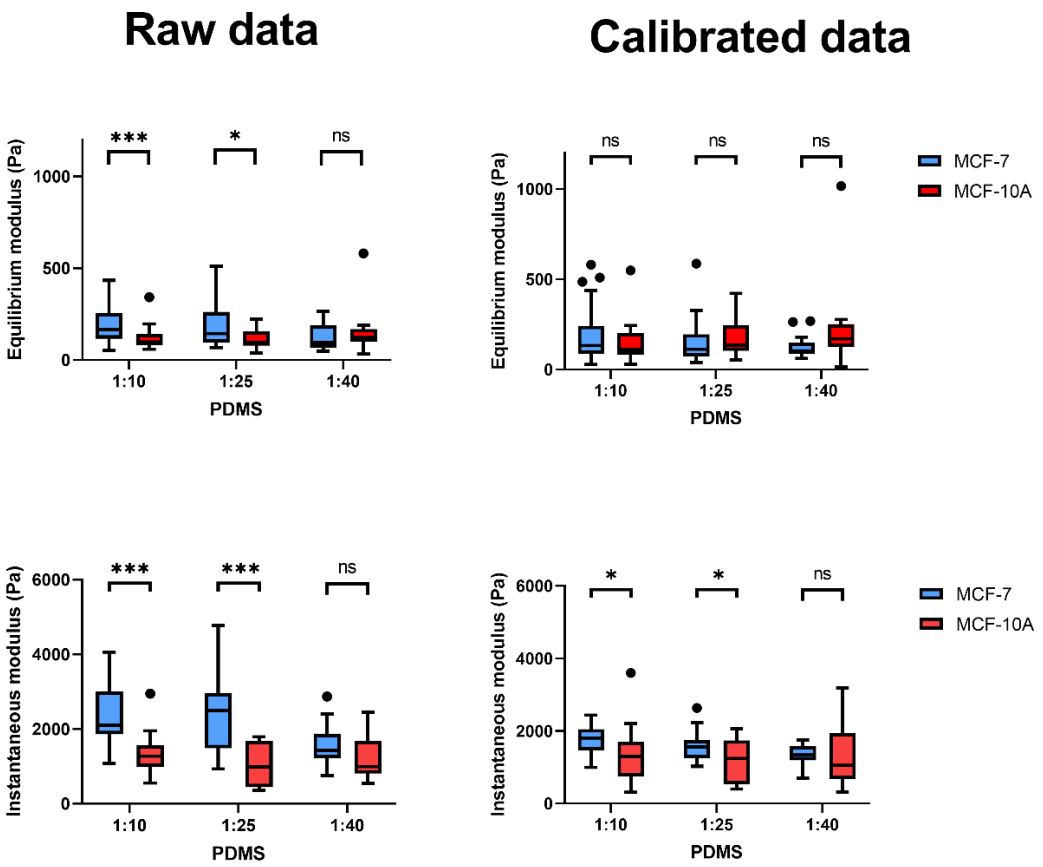


Figure 6-20. Comparison of cell moduli raw data and calibrated data for results in Chapter 5. There was no significant difference between the apparent moduli and the calibrated moduli of MCF-10A.

The apparent modulus of MCF-7 cells was reduced after using the calibrated model, while there were no significant changes in the moduli of MCF-10A. This is because the adhesion force of MCF-10A on the substrate is greater than that of MCF-7. During the FEM measurements, although the measured cells were randomly selected, the well-spread MCF-10A was more difficult to be separated from the substrate. As a result, less-spread cells accounted for a larger proportion of MCF-10A than MCF-7 in the measured data counted, 82.2% and 54.5% respectively. The well-spread cells received a greater substrate effect than the less-spread cells, resulting in the larger apparent moduli.

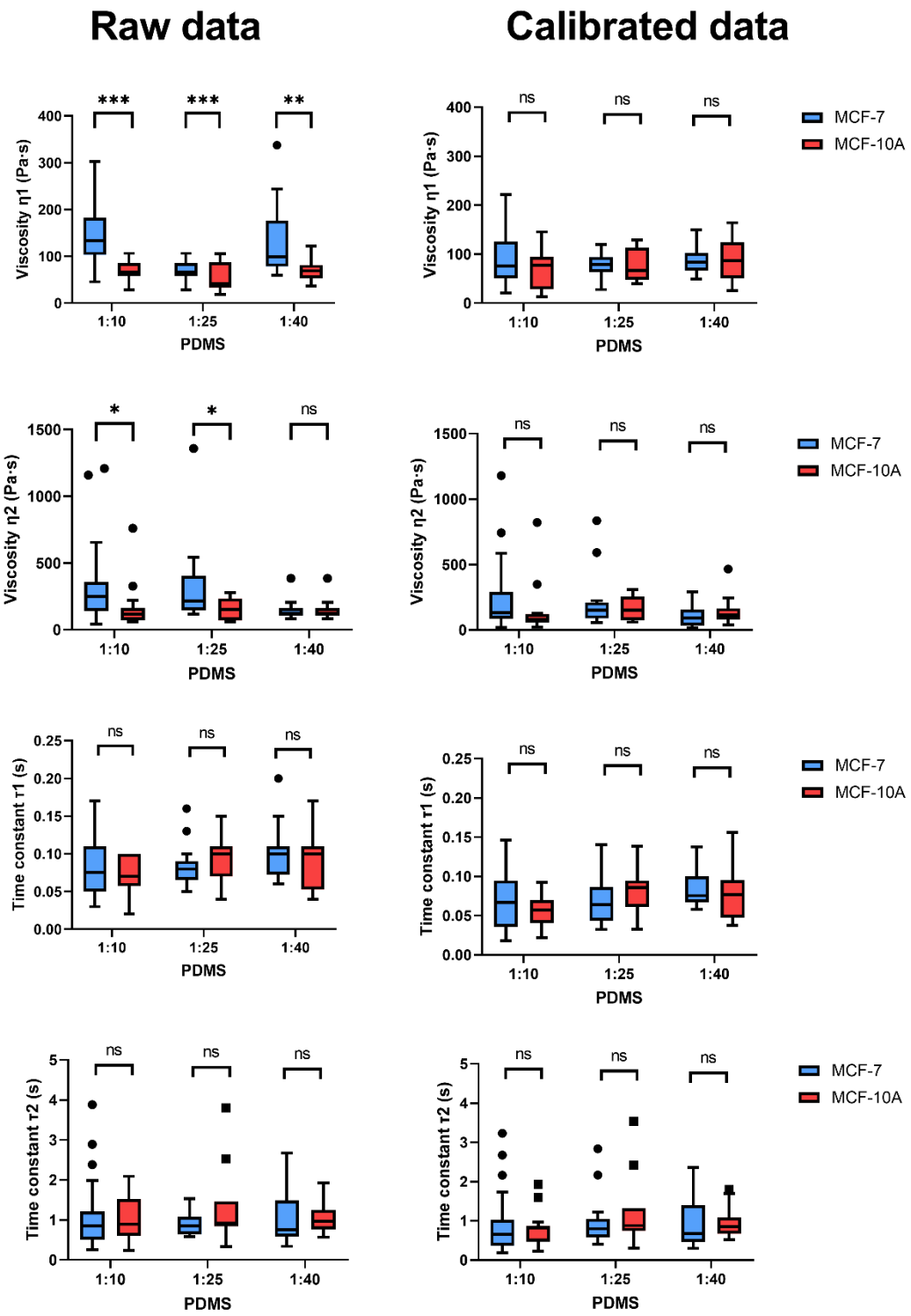


Figure 6-21. Comparison of viscoelastic parameters raw data and calibrated data for results in Chapter 5. The viscoelastic parameters of the two cells became no longer significantly different after correction.

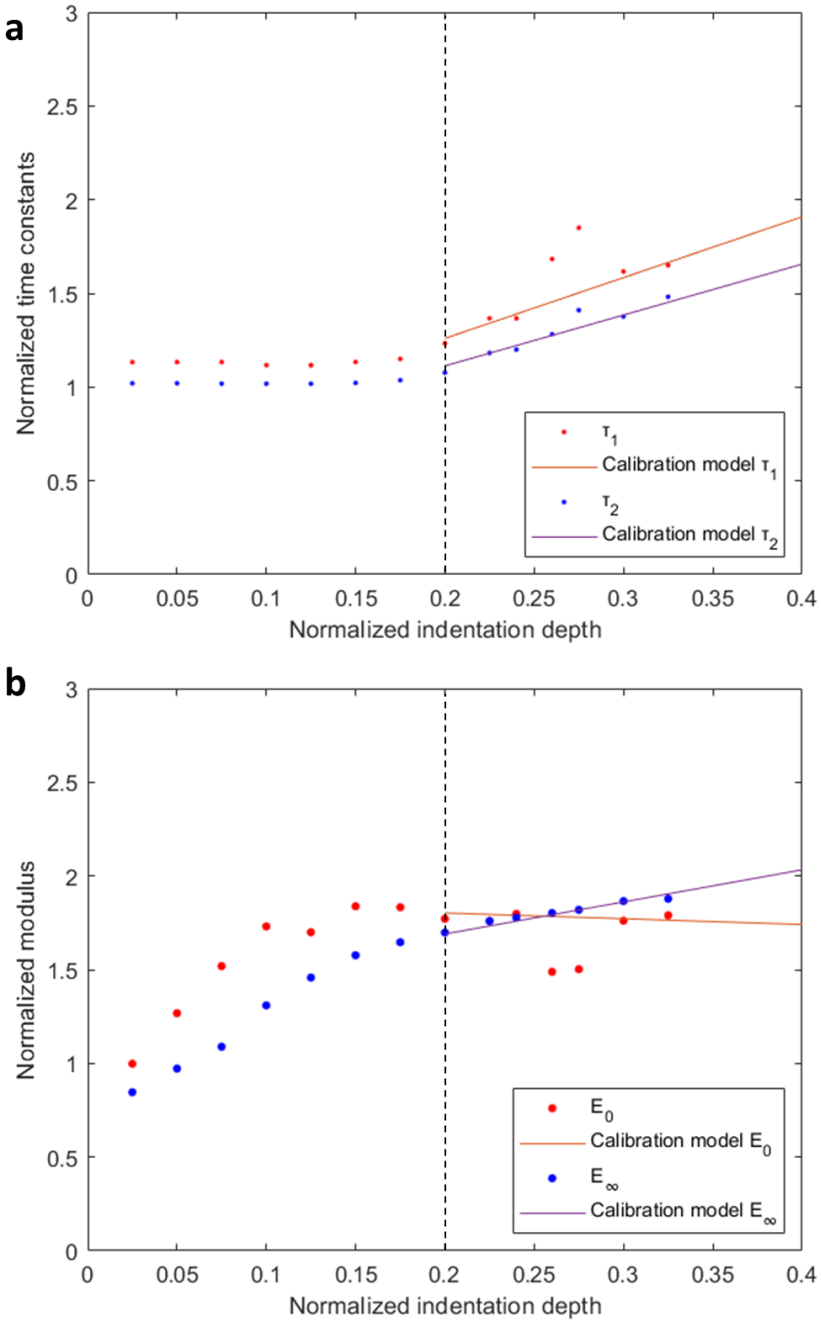


Figure 6-22. Calibration models for the apparent viscoelastic parameters: (a) time constant $\tau$; (b) instantaneous modulus $E_0$ and equilibrium modulus $E_\infty$. Because the indentation depth in the experiments were 20%-50% of the cell thickness, data points with an indentation depth of 20% or more were used for the fitting, represented in the graph as the interval to the right of the black dashed line. Two discrete points of $\tau_1$ and $E_0$ are excluded in the calculation of the calibration equation.

#### 6.3.3.3. Thin-layer cylinders

**Substrate effect**

In the indentation of wide discs with the same material properties and thickness as the cells at different depths, the radii of the discs are much larger than the dimensions of the cells and the indenter. In this case, the difference between apparent and actual viscoelastic properties can therefore be considered to result from the separate effect of the substrate.

In the indentation simulation of the cylinder model with the same thickness as the less-spread cell, the apparent instantaneous and equilibrium moduli show relatively small variations with indentation depth, both within 10%, while the apparent time constant and viscosity modulus increase with increasing indentation depth.

The apparent second-order time constant $\tau_1$ is stable at an indentation depth of less than 12.5% of the model thickness, which is the same as the actual value. Then it starts to rise rapidly when the indentation depth exceeds 12.5% of the model thickness, reaching a local maximum value of 173% of the actual value at 19% of the model thickness, before decreasing as the indentation depth increases further and reaching a local minimum value at 25% of the model thickness of 142% of the actual value, and continuing to rise to 30% of the indentation depth of 172% of the actual value. The apparent first-order time constant $\tau_2$ also stabilises at around 115% of the actual value for indentation depths less than 12.5% of model thickness. It then rises and reaches a maximum value of 142% at 19%, decreasing slightly as the indentation depth increases further and it then remains between 127% and 136% of the actual value.

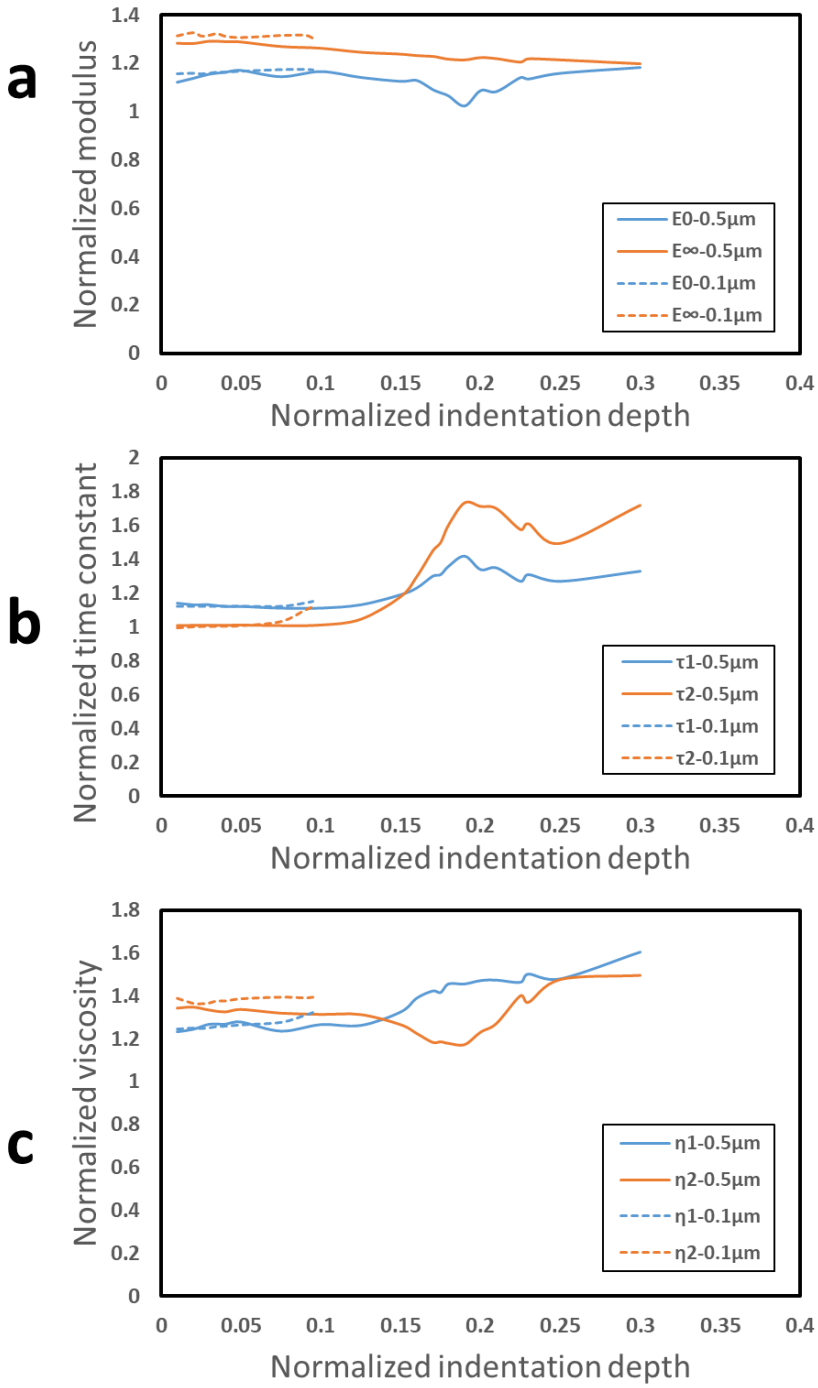


Figure 6-23. Variation in apparent viscoelastic parameters with indentation depth for cylinders with the same height as the less-spread cell model: (a) time constant τ; (b) instantaneous modulus $E_0$ and equilibrium modulus $E_\infty$; (c) viscosity η. The solid curve is the measurement of the 0.5 μm fillet radius indenter, indicated by -0.5μm. and the dashed curve is the measurement of the 0.5 μm fillet radius indenter, indicated by -0.1μm.

The apparent equilibrium modulus decreases slightly and linearly from 128% to 120% of the actual value between 1% to 30% of the indentation depth. The apparent instantaneous modulus varies between 112% and 118% of the actual value at all indentation depths, except for a fluctuation between 17% and 21% indentation depth, where it drops to 102% of the actual value at 19% indentation depth.

The apparent viscosities of the first and second Maxwell-arms $\eta_1$ and $\eta_2$ stabilise at around 126% and 133% of the actual values respectively when the indentation depth is less than 12.5% of the model thickness. Then η1 rises linearly, reaching 160% of the actual value at 30% indentation depth, whereas η2 firstly takes a downward swing, dropping to 118% of the actual value at 19% indentation depth, before rising again to 150% of the actual value at 30% indentation depth.

In this cylinder model, there is little difference in the results for indenters with different fillet radii. It is worth noting that the apparent time constant for the 0.1 μm fillet radius indenter starts to rise at an indentation of 9% of the model thickness, which is less than the 12.5% indentation depth at the start of the rise for the 0.5 μm fillet radius indenter.

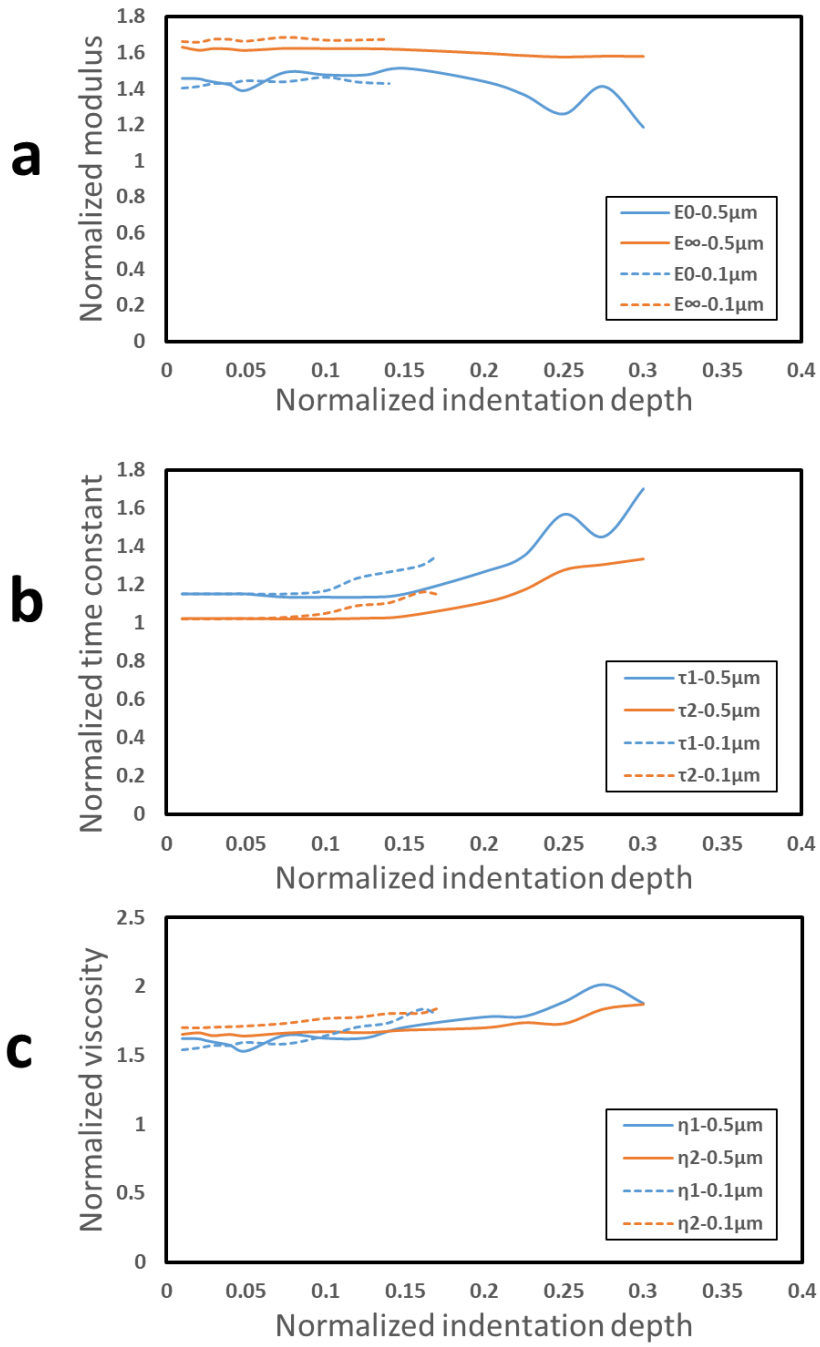


Figure 6-24. Variation in apparent viscoelastic parameters with indentation depth for cylinders with the same height as the well-spread cell model: (a) time constant $\tau$; (b) instantaneous modulus E0 and equilibrium modulus Elong; (c) viscosity $\eta$. The solid curve is the measurement of the 0.5 μm fillet radius indenter indicated by -0.5μm, and the dashed curve is the measurement of the 0.1 μm fillet radius indenter indicated by -0.1μm.

The indentation simulations results of cylinders with the same height as the well-spread cell model vary with indentation depth and show similar trend as the cylinder with the same height as the well-spread cell model, and also fluctuate less than the latter when the indentation depth is over 15% of the model thickness.

For the 0.5 μm fillet radius indenter, the apparent time constants $\tau_1$ and $\tau_2$ are 115% and 102% of the actual values respectively when the indentation depth is less than 15%. Both apparent time constants rise to 170% and 133% of the actual value respectively at 30% indentation depth. The value of $\tau_1$ fluctuates by ±20% in the 25%-30% indentation depth, while for the 0.1 μm fillet radius indenter the values of apparent $\tau_1$ and $\tau_2$ are same as in the results for the 0.5 μm fillet radius indenter at the beginning. Then they rise earlier at an indentation depth of 10% and, when the indentation depth reaches 17%, they are 135% and 115% respectively of the actual values.

For the apparent instantaneous and equilibrium moduli, the difference between the results for the indenters with different fillet radii is within 5%. The apparent equilibrium modulus remains constant at approximately 160% of the actual value. The instantaneous modulus is approximately 140% of the actual value at indentation depths less than 20% of the model thickness, and then fluctuates at indentation depths greater than 20% with an amplitude of approximately 20% and is complementary to the fluctuations in $\tau_1$.

The apparent viscosities $\eta_1$ and $\eta_2$ show slight increases with increasing indentation depth. For smaller fillet radius indentations, the apparent $\eta_1$ is 160% of the actual value at 1% indentation depth, rising to 187% of the actual value when the indentation depth reaches 30% of the model thickness. The apparent $\eta_2$ is 165% of the actual value at 1% indentation depth, rising to 187% of the

actual value when the indentation depth reaches 30% of the model thickness. For larger fillet radius indentations, the apparent $\eta_1$ increases from 170% of the actual value at 1% indentation depth to 183% of the actual value at 17% indentation depth; while the apparent $\eta_2$ increases from 153% of the actual value at 1% indentation depth to 182% of the actual value at 17% indentation depth.

The difference between the apparent and actual values of the viscoelastic parameters due to the substrate effect can be seen in the above two groups of indentation simulations. The self-similar or spherical indenters have a small contact area at low indentation depths, and the measured apparent modulus is closer to the actual value. In contrast to the former indenters, the contact area of the indenter and cylinder represents full contact at a very small indentation depth and does not vary with indentation depth. Therefore, when the indentation is small relative to the thickness of the model, the force measured by the indenter is affected by a non-negligible substrate effect.

As the indentation depth increases, both the time constant $\tau$ and equilibrium $E_0$ fluctuate, and their fluctuations are exactly complementary so that viscosity $\eta$ does not fluctuate as much with indentation depth as the first two at large indentation depths. Since the two fluctuations are complementary, it can be hypothesized that this fluctuation is an error due to the relaxation curve fitting.

**The effect of the finite width and thickness of the sample**

The thickness of the cylinder (which is the same as for the well-spread cell) was then controlled and the radius was varied to observe the change in apparent viscoelastic parameters as the cylinder was reduced from infinite width to cell size. Here it can be assumed that any such change is the result only of the combined effect of the finite width boundary condition.

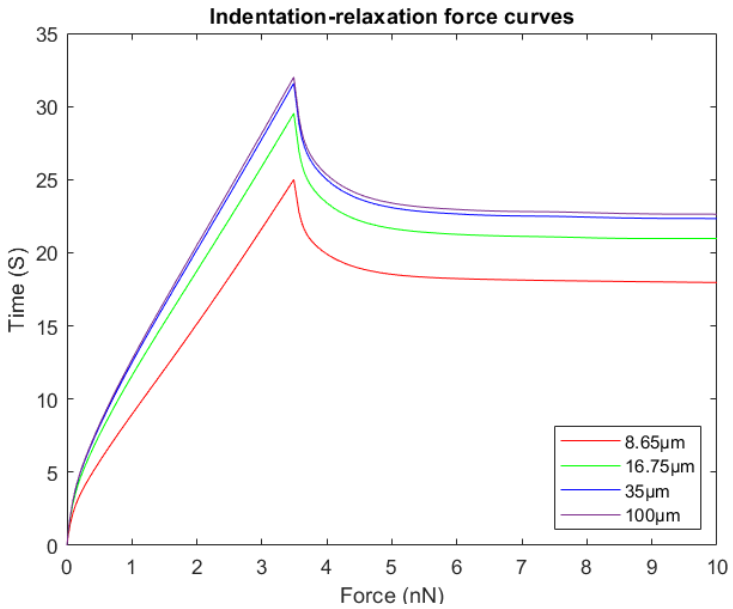


Figure 6-25. Force-time curves for indentations of cylinder models with different radii. The first 3.5 seconds is the indenter loading period, and after 3.5 seconds the indenter remains in the same position and the viscoelastic cylinder starts its relaxation.

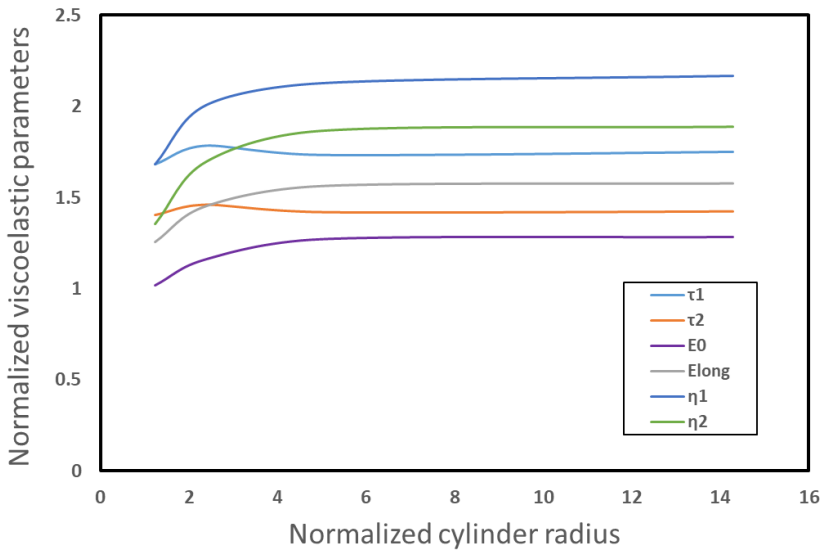


Figure 6-26. Trends in the apparent viscoelastic parameters of cylinders of the same thickness as the well-spread cell with variation in cylinder radius, where the apparent viscoelastic parameters have been normalized to the actual values. The apparent viscoelastic parameters were obtained from the data analysis of the relaxation curve in Figure 6-25. The cylinder radius was normalized to the indenter radius.

As can be seen from Figure 6-25 and Figure 6-26, the finite width effect reduces the force on the indenter as the horizontal size of the model decreases, and then becomes negligible once the radius of the cylinder model is greater than 5 times the radius of the indenter.

## 6.4. Conclusions

This chapter describes the use of FEA simulation to investigate the feasibility of the modified Sneddon model for the analysis of viscoelastic materials and to develop different cell and disc models of the corresponding thicknesses to investigate the effect of not meeting the ideal conditions on the measurement results. The cell models are verified by mesh sensitivity analysis.

The modified Sneddon model can accurately predict the force profile of indentation-relaxation for non-step loading forces and can be approximated as an infinite half-space model for model thicknesses and widths greater than 10 and 5 times the radius of the flat-punch indenter respectively.

The measured apparent viscoelastic parameters of the cells are mainly influenced by the substrate, finite boundary, and cell surface slope and three-dimensional structure effects which respectively correspond to the actual situation of planar conditions that do not satisfy the infinite thickness, infinite width and infinite half-space as assumed by the flat punch contact model[205].

The substrate effect results in the measured instantaneous and equilibrium moduli being larger than the actual values. Because the contact area between the flat-punch indenter and the cylinder represents full contact at very small indentation depths and does not vary with indentation depth, the measured values of both moduli will be larger even when the indentation is small relative to the thickness of the model. The time constants do not differ significantly from the actual values until the indentation depth is less than 10% of the model thickness but increase with increasing indentation depth once the indentation depth exceeds 10% of the model thickness.

The finite width effect causes the viscoelastic parameters to decrease as the radius of the model decreases, but when the radius of the model is greater than 5 times the radius of the flat-punch indenter, the finite width effect can be ignored.

The measured apparent viscoelastic parameters are affected differently in the well-spread and less-spread cell models. This is because the cell surface slopes and three-dimensional structures are different. However, the measured apparent viscoelastic parameters follow a similar trend where both increase with indentation depth.

# Chapter 7. Conclusions and future work

## 7.1. Conclusions

In this work, experimental protocols have been developed to simultaneously determine the viscoelastic and adhesion properties of single cells. These yield results consistent with previously reported values using AFM while also taking loading effects into account[151, 155]. The Young's modulus (equilibrium elastic modulus) of MCF-7 cells on tissue culture-treated polystyrene dishes was approximately 0.2 kPa, and this was not dependent on cell morphology. In contrast, cell adhesion was closely related to the rate at which the cells spread. The viscoelasticity of MCF-7 cells obtained from the measurements taken is consistent with the previously reported results from AFM nanoindentation using spherical probes.

The pulling tests using FluidFM during the retraction stage can detect multiple discrete events that could be associated with the separation of different adhesion structures.

For the same stiffness of surfaces, MFC-7 cells exhibited lower adhesion than MCF-10A cells to PDMS surfaces. This is correlated to much higher migration rates of MCF-7 compared to MCF-10A cells. The modulus of MCF-7 cells decreased with the softening of the underlying substrate, while the time constant increased with the decreasing stiffness of the PDMS. The experimental results for adhesion force, spread area and stiffness of MCF-7 cells are also consistent with results published in the literature. Stiffer substrates and larger cell-substrate contact areas are associated with greater cell-substrate adhesion, thereby reducing cell migration speed[200, 201].

In contrast, the viscoelastic parameters of MCF-10A cells did not vary with the stiffness of the attached surface.

The results were further analyzed using statistical methods to determine the correlations between cellular mechanical parameters and to provide a reasonable interpretation of the findings in the light of previous studies. The present experimental and empirical results support some of the mechanical models of subcellular structures proposed in the literature.

Finite element modelling has also confirmed that thin layer effect is not significant when indenting the less spread cells. This is due to the combined effect of cell morphology and finite thickness of cells. Whilst the thin layer effect is still significant for well spread cells. Furthermore, when using the empirical equations informed by FE simulations to modify the contact models, the spherical cells (possibly at mitosis phase) appear to be 1.4 times stiffer than well-spread cells (possibly at S/G1 phase) attached to the same substrate. This agrees with the findings of other *in situ* studies of cells at different phases[149, 157].

Research in cell mechanics is now still biased towards basic research, dedicated to describing complex cell structures in a practical simplified mathematical model, which is then used to further investigate cell behaviour that is difficult to explain using traditional biochemical pathways.

As mentioned in literature review, since the 1980s, researchers have used measurements of cell mechanics in vitro to diagnose cancer[6, 10, 59, 112]. However, this technique has not been widely used for clinical diagnosis of cancer yet, the main drawback being the low throughput of the cells detected. Typically, a flow cytometer can detect thousands of cells per second, whereas an AFM probe can take 10 seconds to a few minutes to measure a single cell. IBM developed a technology that uses thousands of AFM cantilevers simultaneously, Millipede[206], which is used for data storage and reads data by measuring the mechanical properties of the material surface. If this

technique of manipulating thousands of AFM cantilevers simultaneously is used for in vitro cell diagnostics, it will solve the current problem of low throughput of AFM for in vitro cell detection. The technology needs to address how to neatly culture the cells on the container arrays corresponding to the AFM cantilevers arrays to ensure that each cantilever is touching a single cell.

In addition to diagnostics, AFM technology has advantages in the biomedical field in experiments where high throughput is not required. For example, using AFM to measure the mechanical properties of cells is used to examine the performance of drugs[207-209]. And the molecular level imaging that AFM can do on cells also helps to examine drug delivery[210-213].

## 7.2. Future work

The present study treats a cell as a homogeneous isotropic monolithic viscoelastic material. This assumption simplifies the complexity involved but is not suitable in studying the effect of subcellular structures such as the cytoskeleton and nucleus on the mechanical properties of the cell. Therefore, future studies should consider more complex cellular models which consists of the nucleus, cytoplasm, microtubules and actin[28, 32]. Besides, the FEA simulation also need to consider the PDMS substrates rather than only using rigid substrates. Experiment protocols will also need to be developed to measure the viscoelastic parameters of these different cell components separately in order to investigate the links between them.

In considering the effect of different external environments on the mechanical properties of cells, this study was only designed to consider surfaces with different levels of stiffness. In future studies, cells should be grown on surfaces with varying structures.

In the future, it would also be desirable to combine AFM and confocal microscopy to enable the in-situ observation of cell deformation. In addition, AFM cantilevers with spherical will be employed to do nanoindentation for viscoelastic properties measurement of cells to further validate the results determined using the FluidFM.

# References


[1] J. Ferlay *et al.*, "Cancer incidence and mortality worldwide: sources, methods and major patterns in GLOBOCAN 2012," *International journal of cancer,* vol. 136, no. 5, 2015.

[2] B. Stewart and C. P. Wild, "World cancer report 2014," *Health,* 2017.

[3] M. H. Forouzanfar *et al.*, "Global, regional, and national comparative risk assessment of 79 behavioural, environmental and occupational, and metabolic risks or clusters of risks, 1990–2015: a systematic analysis for the Global Burden of Disease Study 2015," *The Lancet,* vol. 388, no. 10053, pp. 1659-1724, 2016.

[4] D. Hanahan and R. A. Weinberg, "The hallmarks of cancer," *cell,* vol. 100, no. 1, pp. 57-70, 2000.

[5] S. Suresh, "Nanomedicine: elastic clues in cancer detection," *Nature Nanotechnology,* vol. 2, no. 12, p. 748, 2007.

[6] P. Katira, R. T. Bonnecaze, and M. H. Zaman, "Modeling the mechanics of cancer: effect of changes in cellular and extra-cellular mechanical properties," *Frontiers in oncology,* vol. 3, p. 145, 2013.

[7] M. Plodinec *et al.*, "The nanomechanical signature of breast cancer," *Nature nanotechnology,* vol. 7, no. 11, p. 757, 2012.

[8] S. Suresh, "Biomechanics and biophysics of cancer cells," *Acta Materialia,* vol. 55, no. 12, pp. 3989-4014, 2007.

[9] L. Hinck and I. Näthke, "Changes in cell and tissue organization in cancer of the breast and colon," *Current opinion in cell biology,* vol. 26, pp. 87-95, 2014.

[10] M. Lekka, "Discrimination between normal and cancerous cells using AFM," *Bionanoscience,* vol. 6, no. 1, pp. 65-80, 2016.

[11] X. F. Cai, H. Deng, J. Y. Cai, and X. Huang, "Progress and application of atomic force microscope concerning mechanical properties of cells," *Journal of Clinical Rehabilitative Tissue Engineering Research,* vol. 12, no. 48, pp. 9573-9576, 2008.

[12] S. Hiratsuka, Y. Mizutani, M. Tsuchiya, K. Kawahara, H. Tokumoto, and T. Okajima, "The number distribution of complex shear modulus of single cells measured by atomic force microscopy," *Ultramicroscopy,* vol. 109, no. 8, pp. 937-941, 2009.

[13] G. Lenormand, E. Millet, B. Fabry, J. P. Butler, and J. J. Fredberg, "Linearity and time-scale invariance of the creep function in living cells," *Journal of The Royal Society Interface,* vol. 1, no. 1, pp. 91-97, 2004.

[14] J. Alcaraz *et al.*, "Microrheology of human lung epithelial cells measured by atomic force microscopy," *Biophysical journal,* vol. 84, no. 3, pp. 2071-2079, 2003.

[15] B. Fabry, G. N. Maksym, J. P. Butler, M. Glogauer, D. Navajas, and J. J. Fredberg, "Scaling the microrheology of living cells," *Physical review letters,* vol. 87, no. 14, p. 148102, 2001.

[16] L. Deng *et al.*, "Fast and slow dynamics of the cytoskeleton," *Nature materials,* vol. 5, no. 8, pp. 636-640, 2006.

[17] A. R. Bausch, F. Ziemann, A. A. Boulbitch, K. Jacobson, and E. Sackmann, "Local measurements of viscoelastic parameters of adherent cell surfaces by magnetic bead microrheometry," *Biophysical journal,* vol. 75, no. 4, pp. 2038-2049, 1998.

[18] P. Kollmannsberger and B. Fabry, "BaHigh-force magnetic tweezers with force feedback for biological applications," *Review of Scientific Instruments,* vol. 78, no. 11, p. 114301, 2007.

[19] C. E. Schmidt, A. F. Horwitz, D. A. Lauffenburger, and M. P. Sheetz, "Integrin-cytoskeletal interactions in migrating fibroblasts are dynamic, asymmetric, and regulated," *The Journal of cell biology,* vol. 123, no. 4, pp. 977-991, 1993.

[20] M. Balland *et al.*, "Power laws in microrheology experiments on living cells: Comparative analysis and modeling," *Physical Review E,* vol. 74, no. 2, p. 021911, 2006.

[21] N. Desprat, A. Richert, J. Simeon, and A. Asnacios, "Creep function of a single living cell," *Biophysical journal,* vol. 88, no. 3, pp. 2224-2233, 2005.

[22] S. G. Charlton *et al.*, "Regulating, measuring, and modeling the viscoelasticity of bacterial biofilms," *Journal of bacteriology,* vol. 201, no. 18, pp. e00101-19, 2019.

[23] J. C. Crocker *et al.*, "Two-point microrheology of inhomogeneous soft materials," *Physical Review Letters,* vol. 85, no. 4, p. 888, 2000.

[24] D. Wirtz, "Particle-tracking microrheology of living cells: principles and applications," *Annual review of biophysics,* vol. 38, no. 1, pp. 301-326, 2009.

[25] J. J. Chen, "Nanobiomechanics of living cells: a review," *Interface Focus,* vol. 4, no. 2, Apr 2014, Art no. 20130055, doi: 10.1098/rsfs.2013.0055.

[26] J. J. Chen and G. X. Lu, "Finite element modelling of nanoindentation based methods for mechanical properties of cells," *Journal of Biomechanics,* vol. 45, no. 16, pp. 2810-2816, Nov 2012, doi: 10.1016/j.jbiomech.2012.08.037.

[27] G. T. Charras and M. A. Horton, "Single cell mechanotransduction and its modulation analyzed by atomic force microscope indentation," *Biophysical Journal,* vol. 82, no. 6, pp. 2970-2981, Jun 2002, doi: 10.1016/s0006-3495(02)75638-5.

[28] S. Barreto, C. H. Clausen, C. M. Perrault, D. A. Fletcher, and D. Lacroix, "A multi-structural single cell model of force-induced interactions of cytoskeletal components," *Biomaterials,* vol. 34, no. 26, pp. 6119-6126, Aug 2013, doi: 10.1016/j.biomaterials.2013.04.022.

[29] C. R. Guerrero, P. D. Garcia, and R. Garcia, "Subsurface Imaging of Cell Organelles by Force Microscopy," *Acs Nano,* vol. 13, no. 8, pp. 9629-9637, Aug 2019, doi: 10.1021/acsnano.9b04808.

[30] G. T. Charras and M. A. Horton, "Determination of cellular strains by combined atomic force microscopy and finite element modeling," *Biophysical Journal,* vol. 83, no. 2, pp. 858-879, Aug 2002, doi: 10.1016/s0006-3495(02)75214-4.

[31] P. Carl and H. Schillers, "Elasticity measurement of living cells with an atomic force microscope: data acquisition and processing," *Pflugers Archiv-European Journal of Physiology,* vol. 457, no. 2, pp. 551-559, Nov 2008, doi: 10.1007/s00424-008-0524-3.

[32] W. J. Yang, D. Lacroix, L. P. Tan, and J. J. Chen, "Revealing the nanoindentation response of a single cell using a 3D structural finite element model," *Journal of Materials Research,* vol. in press, pp. DOI:10.1557/s43578-020-00004-5, 2021, doi: 10.1557/s43578-020-00004-5.

[33] J. A. C. Santos, L. M. Rebelo, A. C. Araujo, E. B. Barros, and J. S. de Sousa, "Thickness-corrected model for nanoindentation of thin films with conical indenters," *Soft Matter,* vol. 8, no. 16, pp. 4441-4448, 2012, doi: 10.1039/c2sm07062f.

[34] E. M. Darling, S. Zauscher, J. A. Block, and F. Guilak, "A thin-layer model for viscoelastic, stress-relaxation testing of cells using atomic force microscopy: Do cell properties reflect metastatic potential?," *Biophysical Journal,* vol. 92, no. 5, pp. 1784-1791, Mar 2007, doi: 10.1529/biophysj.106.083097.

[35] E. K. Dimitriadis, F. Horkay, J. Maresca, B. Kachar, and R. S. Chadwick, "Determination of elastic moduli of thin layers of soft material using the atomic force microscope," *Biophysical Journal,* vol. 82, no. 5, pp. 2798-2810, May 2002, doi: 10.1016/s0006-3495(02)75620-8.

[36] W. R. Bowen, N. Hilal, R. W. Lovitt, and C. J. Wright, "Direct measurement of the force of adhesion of a single biological cell using an atomic force microscope," *Colloids and Surfaces a-Physicochemical and Engineering Aspects,* vol. 136, no. 1-2, pp. 231-234, Apr 1998, doi: 10.1016/s0927-7757(97)00243-4.

[37] J. Friedrichs *et al.*, "A practical guide to quantify cell adhesion using single-cell force spectroscopy," *Methods,* vol. 60, no. 2, pp. 169-178, Apr 2013, doi: 10.1016/j.ymeth.2013.01.006.

[38] G. Weder *et al.*, "The quantification of single cell adhesion on functionalized surfaces for cell sheet engineering," *Biomaterials,* vol. 31, no. 25, pp. 6436-6443, Sep 2010, doi: 10.1016/j.biomaterials.2010.04.068.

[39] E. P. Wojcikiewicz, X. Zhang, A. Chen, and V. T. Moy, "Contributions of molecular binding events and cellular compliance to the modulation of

leukocyte adhesion," *Journal of cell science,* vol. 116, no. 12, pp. 2531-2539, 2003.

[40] J. Friedrichs, J. Helenius, and D. J. Muller, "Stimulated single-cell force spectroscopy to quantify cell adhesion receptor crosstalk," *Proteomics,* vol. 10, no. 7, pp. 1455-1462, 2010.

[41] P. Dorig *et al.*, "Force-controlled spatial manipulation of viable mammalian cells and micro-organisms by means of FluidFM technology," *Applied Physics Letters,* vol. 97, no. 2, Jul 2010, Art no. 023701, doi: 10.1063/1.3462979.

[42] O. Guillaume-Gentil, E. Potthoff, D. Ossola, C. M. Franz, T. Zambelli, and J. A. Vorholt, "Force-controlled manipulation of single cells: from AFM to FluidFM," *Trends in Biotechnology,* vol. 32, no. 7, pp. 381-388, Jul 2014, doi: 10.1016/j.tibtech.2014.04.008.

[43] M. Y. Amarouch, J. El Hilaly, and D. Mazouzi, "AFM and FluidFM Technologies: Recent Applications in Molecular and Cellular Biology," *Scanning,* 2018, Art no. 7801274, doi: 10.1155/2018/7801274.

[44] P. Saha, T. Duanis-Assaf, and M. Reches, "Fundamentals and Applications of FluidFM Technology in Single-Cell Studies," *Advanced Materials Interfaces,* vol. 7, no. 23, Dec 2020, Art no. 2001115, doi: 10.1002/admi.202001115.

[45] M. K. Ghatkesar, H. H. P. Garza, and U. Staufer, "Hollow AFM cantilever pipette," *Microelectronic Engineering,* vol. 124, pp. 22-25, Jul 2014, doi: 10.1016/j.mee.2014.04.019.

[46] P. Wysotzki, A. Sancho, J. Gimsa, and J. Groll, "A comparative analysis of detachment forces and energies in initial and mature cell-material interaction," *Colloids and Surfaces B-Biointerfaces,* vol. 190, Jun 2020, Art no. 110894, doi: 10.1016/j.colsurfb.2020.110894.

[47] L. Jaatinen, E. Young, J. Hyttinen, J. Vörös, T. Zambelli, and L. Demkó, "Quantifying the effect of electric current on cell adhesion studied by single-cell force spectroscopy," *Biointerphases,* vol. 11, no. 1, p. 011004, 2016.

[48] Q. Li, G. Y. Lee, C. N. Ong, and C. T. Lim, "AFM indentation study of breast cancer cells," *Biochemical and biophysical research communications,* vol. 374, no. 4, pp. 609-613, 2008.

[49] K. Dey, E. Roca, G. Ramorino, and L. Sartore, "Progress in the mechanical modulation of cell functions in tissue engineering," *Biomaterials Science,* vol. 8, no. 24, pp. 7033-7081, Dec 2020, doi: 10.1039/d0bm01255f.

[50] C. Kothapalli, G. Mahajan, and K. Farrell, "Substrate stiffness induced mechanotransduction regulates temporal evolution of human fetal neural progenitor cell phenotype, differentiation, and biomechanics," *Biomaterials Science,* vol. 8, no. 19, pp. 5452-5464, Oct 2020, doi: 10.1039/d0bm01349h.

[51] J. Chen *et al.*, "Cell Mechanics, Structure, and Function Are Regulated by the Stiffness of the Three-Dimensional Microenvironment," *Biophysical Journal,* vol. 103, no. 6, pp. 1188-1197, Sep 2012, doi: 10.1016/j.bpj.2012.07.054.

[52] A. Diz-Munoz, D. A. Fletcher, and O. D. Weiner, "Use the force: membrane tension as an organizer of cell shape and motility," *Trends in Cell Biology,* vol. 23, no. 2, pp. 47-53, Feb 2013, doi: 10.1016/j.tcb.2012.09.006.

[53] M. G. Haugh, C. M. Murphy, R. C. McKiernan, C. Altenbuchner, and F. J. O'Brien, "Crosslinking and Mechanical Properties Significantly Influence Cell Attachment, Proliferation, and Migration Within Collagen Glycosaminoglycan Scaffolds," *Tissue Engineering Part A,* vol. 17, no. 9-10, pp. 1201-1208, May 2011, doi: 10.1089/ten.tea.2010.0590.

[54] M. Lekka, P. Laidler, D. Gil, J. Lekki, Z. Stachura, and A. Z. Hrynkiewicz, "Elasticity of normal and cancerous human bladder cells studied by scanning force microscopy," *European Biophysics Journal with Biophysics Letters,* vol. 28, no. 4, pp. 312-316, 1999, doi: 10.1007/s002490050213.

[55] D. Dutta, X. L. Palmer, J. Ortega-Rodas, V. Balraj, I. G. Dastider, and S. Chandra, "Biomechanical and Biophysical Properties of Breast Cancer Cells Under Varying Glycemic Regimens," *Breast Cancer-Basic and Clinical Research,* vol. 14, Nov 2020, Art no. 1178223420972362, doi: 10.1177/1178223420972362.

[56] Q. S. Li, G. Y. H. Lee, C. N. Ong, and C. T. Lim, "AFM indentation study of breast cancer cells," *Biochemical and Biophysical Research Communications,* vol. 374, no. 4, pp. 609-613, Oct 2008, doi: 10.1016/j.bbrc.2008.07.078.

[57] D. Ghosh and M. R. Dawson, "Microenvironment Influences Cancer Cell Mechanics from Tumor Growth to Metastasis," in *Biomechanics in Oncology*, vol. 1092, C. Dong, N. Zahir, and K. Konstantopoulos Eds., (Advances in Experimental Medicine and Biology, 2018, pp. 69-90.

[58] S. Azadi, M. Tafazzoli-Shadpour, M. Soleimani, and M. E. Warkiani, "Modulating cancer cell mechanics and actin cytoskeleton structure by chemical and mechanical stimulations," *Journal of Biomedical Materials Research Part A,* vol. 107, no. 8, pp. 1569-1581, Aug 2019, doi: 10.1002/jbm.a.36670.

[59] S. Suresh, "Biomechanics and biophysics of cancer cells," *Acta Biomaterialia,* vol. 3, no. 4, pp. 413-438, Jul 2007, doi: 10.1016/j.actbio.2007.04.002.

[60] M. Janiszewska, M. C. Primi, and T. Izard, "Cell adhesion in cancer: Beyond the migration of single cells," *Journal of Biological Chemistry,* vol. 295, no. 8, pp. 2495-2505, Feb 2020, doi: 10.1074/jbc.REV119.007759.

[61] D. Boal and D. H. Boal, *Mechanics of the Cell*. Cambridge University Press, 2012.

[62] S. Kim and P. A. Coulombe, "Intermediate filament scaffolds fulfill mechanical, organizational, and signaling functions in the cytoplasm," *Genes & development,* vol. 21, no. 13, pp. 1581-1597, 2007.
[63] S. J. Gunst, D. D. Tang, and A. O. Saez, "Cytoskeletal remodeling of the airway smooth muscle cell: a mechanism for adaptation to mechanical forces in the lung," *Respiratory physiology & neurobiology,* vol. 137, no. 2-3, pp. 151-168, 2003.
[64] S. Inoué and E. D. Salmon, "Force generation by microtubule assembly/disassembly in mitosis and related movements," *Collected Works Of Shinya InouÉ: Microscopes, Living Cells, and Dynamic Molecules (With DVD-ROM),* pp. 749-770, 2008.
[65] R. Satcher and C. F. Dewey, "Theoretical estimates of mechanical properties of the endothelial cell cytoskeleton," *Biophysical journal,* vol. 71, no. 1, pp. 109-118, 1996.
[66] D. E. Ingber, "The architecture of life," *Scientific American,* vol. 278, no. 1, pp. 48-57, 1998.
[67] D. Stamenovic, S. M. Mijailovich, I. M. Tolić-Nørrelykke, J. Chen, and N. Wang, "Cell prestress. II. Contribution of microtubules," *American journal of physiology-Cell physiology,* vol. 282, no. 3, pp. C617-C624, 2002.
[68] J. Kang, R. L. Steward, Y. Kim, R. S. Schwartz, P. R. LeDuc, and K. M. Puskar, "Response of an actin filament network model under cyclic stretching through a coarse grained Monte Carlo approach," *Journal of theoretical biology,* vol. 274, no. 1, pp. 109-119, 2011.
[69] R. B. Fuller, *Synergetics: explorations in the geometry of thinking*. Estate of R. Buckminster Fuller, 1982.
[70] D. E. Ingber, "Cellular basis of mechanotransduction," *The Biological Bulletin,* vol. 194, no. 3, pp. 323-327, 1998.
[71] D. E. Ingber, "Cellular tensegrity: defining new rules of biological design that govern the cytoskeleton," *Journal of cell science,* vol. 104, no. 3, pp. 613-627, 1993.
[72] M. F. Coughlin and D. Stamenović, "A prestressed cable network model of the adherent cell cytoskeleton," *Biophysical journal,* vol. 84, no. 2, pp. 1328-1336, 2003.
[73] J. McGarry, B. Murphy, and P. McHugh, "Computational mechanics modelling of cell–substrate contact during cyclic substrate deformation," *Journal of the Mechanics and Physics of Solids,* vol. 53, no. 12, pp. 2597-2637, 2005.
[74] N. J. Armstrong, K. J. Painter, and J. A. Sherratt, "A continuum approach to modelling cell–cell adhesion," *Journal of theoretical biology,* vol. 243, no. 1, pp. 98-113, 2006.
[75] C. Lim, E. Zhou, and S. Quek, "Mechanical models for living cells—a review," *Journal of biomechanics,* vol. 39, no. 2, pp. 195-216, 2006.

[76] D. Theret, M. Levesque, M. Sato, R. Nerem, and L. Wheeler, "The application of a homogeneous half-space model in the analysis of endothelial cell micropipette measurements," 1988.
[77] G. Schmid-Schönbein, K.-L. Sung, H. Tözeren, R. Skalak, and S. Chien, "Passive mechanical properties of human leukocytes," *Biophysical Journal,* vol. 36, no. 1, pp. 243-256, 1981.
[78] K. Sung, G. Schmid-Schönbein, R. Skalak, G. Schuessler, S. Usami, and S. Chien, "Influence of physicochemical factors on rheology of human neutrophils," *Biophysical journal,* vol. 39, no. 1, p. 101, 1982.
[79] A. N. Ketene, P. C. Roberts, A. A. Shea, E. M. Schmelz, and M. Agah, "Actin filaments play a primary role for structural integrity and viscoelastic response in cells," *Integrative Biology,* vol. 4, no. 5, pp. 540-549, 2012.
[80] M. H. Korayem, Y. H. Sooha, and Z. Rastegar, "MCF-7 cancer cell apparent properties and viscoelastic characteristics measurement using AFM," *Journal of the Brazilian Society of Mechanical Sciences and Engineering,* vol. 40, no. 6, Jun 2018, Art no. 297, doi: 10.1007/s40430-018-1214-5.
[81] Y. M. Efremov, T. Okajima, and A. Raman, "Measuring viscoelasticity of soft biological samples using atomic force microscopy," *Soft matter,* vol. 16, no. 1, pp. 64-81, 2020.
[82] S. Moreno-Flores, R. Benitez, M. D. Vivanco, and J. L. Toca-Herrera, "Stress relaxation and creep on living cells with the atomic force microscope: a means to calculate elastic moduli and viscosities of cell components," *Nanotechnology,* vol. 21, no. 44, Nov 2010, Art no. 445101, doi: 10.1088/0957-4484/21/44/445101.
[83] S. Moreno-Flores, R. Benitez, M. dM Vivanco, and J. L. Toca-Herrera, "Stress relaxation microscopy: Imaging local stress in cells," *Journal of biomechanics,* vol. 43, no. 2, pp. 349-354, 2010.
[84] A. Yeung and E. Evans, "Cortical shell-liquid core model for passive flow of liquid-like spherical cells into micropipets," *Biophysical journal,* vol. 56, no. 1, pp. 139-149, 1989.
[85] E. Evans and A. Yeung, "Apparent viscosity and cortical tension of blood granulocytes determined by micropipet aspiration," *Biophysical journal,* vol. 56, no. 1, pp. 151-160, 1989.
[86] R. Mahaffy, C. Shih, F. MacKintosh, and J. Käs, "Scanning probe-based frequency-dependent microrheology of polymer gels and biological cells," *Physical review letters,* vol. 85, no. 4, p. 880, 2000.
[87] T. Pritz, "Analysis of four-parameter fractional derivative model of real solid materials," *Journal of Sound and Vibration,* vol. 195, no. 1, pp. 103-115, 1996.
[88] B. Fabry *et al.*, "Time scale and other invariants of integrative mechanical behavior in living cells," *Physical Review E,* vol. 68, no. 4, p. 041914, 2003.

[89] M. Puig-De-Morales *et al.*, "Measurement of cell microrheology by magnetic twisting cytometry with frequency domain demodulation," *Journal of Applied Physiology,* vol. 91, no. 3, pp. 1152-1159, 2001.
[90] F. Guilak, W. R. Jones, H. P. Ting-Beall, and G. M. Lee, "The deformation behavior and mechanical properties of chondrocytes in articular cartilage," *Osteoarthritis and cartilage,* vol. 7, no. 1, pp. 59-70, 1999.
[91] K. A. Athanasiou and A. C. Shieh, "Biomechanics of single chondrocytes and osteoarthritis," *Critical Reviews™ in Biomedical Engineering,* vol. 30, no. 4-6, 2002.
[92] J. N. Reddy, *Introduction to the finite element method*. McGraw-Hill Education, 2019.
[93] L. Ng, H. H. Hung, A. Sprunt, S. Chubinskaya, C. Ortiz, and A. Grodzinsky, "Nanomechanical properties of individual chondrocytes and their developing growth factor-stimulated pericellular matrix," *J Biomech,* vol. 40, no. 5, pp. 1011-23, 2007, doi: 10.1016/j.jbiomech.2006.04.004.
[94] E. M. Arruda and M. C. Boyce, "A three-dimensional constitutive model for the large stretch behavior of rubber elastic materials," *Journal of the Mechanics and Physics of Solids,* vol. 41, no. 2, pp. 389-412, 1993.
[95] I. Kang, D. Panneerselvam, V. P. Panoskaltsis, S. J. Eppell, R. E. Marchant, and C. M. Doerschuk, "Changes in the hyperelastic properties of endothelial cells induced by tumor necrosis factor-α," *Biophysical journal,* vol. 94, no. 8, pp. 3273-3285, 2008.
[96] T. D. Nguyen and Y. Gu, "Investigation of cell-substrate adhesion properties of living chondrocyte by measuring adhesive shear force and detachment using AFM and inverse FEA," *Scientific reports,* vol. 6, no. 1, pp. 1-13, 2016.
[97] G. Ofek, R. M. Natoli, and K. A. Athanasiou, "In situ mechanical properties of the chondrocyte cytoplasm and nucleus," *Journal of biomechanics,* vol. 42, no. 7, pp. 873-877, 2009.
[98] M. Tanase, N. Biais, and M. Sheetz, "Magnetic tweezers in cell biology," *Methods in cell biology,* vol. 83, pp. 473-493, 2007.
[99] M. Dao, C. T. Lim, and S. Suresh, "Mechanics of the human red blood cell deformed by optical tweezers," *Journal of the Mechanics and Physics of Solids,* vol. 51, no. 11-12, pp. 2259-2280, 2003.
[100] C. Manzo and M. F. Garcia-Parajo, "A review of progress in single particle tracking: from methods to biophysical insights," *Reports on progress in physics,* vol. 78, no. 12, p. 124601, 2015.
[101] R. M. Hochmuth, "Micropipette aspiration of living cells," *Journal of biomechanics,* vol. 33, no. 1, pp. 15-22, 2000.
[102] E. Planus *et al.*, "Apical rigidity of an epithelial cell monolayer evaluated by magnetic twisting cytometry: ICAM-1 versus integrin linkages to F-actin structure," *Clinical hemorheology and microcirculation,* vol. 33, no. 3, pp. 277-291, 2005.

[103] Y. Zhang *et al.*, "Interfacing 3D magnetic twisting cytometry with confocal fluorescence microscopy to image force responses in living cells," *Nature protocols,* vol. 12, no. 7, pp. 1437-1450, 2017.
[104] L. Deng *et al.*, "Fast and slow dynamics of the cytoskeleton," *Nature materials,* vol. 5, no. 8, p. 636, 2006.
[105] N. Malagnino, G. Pesce, A. Sasso, and E. Arimondo, "Measurements of trapping efficiency and stiffness in optical tweezers," *Optics Communications,* vol. 214, no. 1-6, pp. 15-24, 2002.
[106] J. R. Moffitt, Y. R. Chemla, D. Izhaky, and C. Bustamante, "Differential detection of dual traps improves the spatial resolution of optical tweezers," *Proceedings of the National Academy of Sciences,* vol. 103, no. 24, pp. 9006-9011, 2006.
[107] R. Donczew, J. Zakrzewska-Czerwińska, and A. Zawilak-Pawlik, "Beyond DnaA: the role of DNA topology and DNA methylation in bacterial replication initiation," *Journal of molecular biology,* vol. 426, no. 12, pp. 2269-2282, 2014.
[108] A. Gahlmann and W. Moerner, "Exploring bacterial cell biology with single-molecule tracking and super-resolution imaging," *Nature Reviews Microbiology,* vol. 12, no. 1, pp. 9-22, 2014.
[109] J. Mitchison and M. Swann, "The mechanical properties of the cell surface," *J. exp. Biol,* vol. 31, no. 3, pp. 443-460, 1954.
[110] M. Sato, M. J. Levesque, and R. M. Nerem, "Micropipette aspiration of cultured bovine aortic endothelial cells exposed to shear stress," *Arteriosclerosis: An Official Journal of the American Heart Association, Inc.,* vol. 7, no. 3, pp. 276-286, 1987.
[111] P. M. Davidson *et al.*, "High-throughput microfluidic micropipette aspiration device to probe time-scale dependent nuclear mechanics in intact cells," *Lab on a Chip,* vol. 19, no. 21, pp. 3652-3663, 2019.
[112] M. M. Yallapu *et al.*, "The roles of cellular nanomechanics in cancer," *Medicinal research reviews,* vol. 35, no. 1, pp. 198-223, 2015.
[113] G. Binnig, C. F. Quate, and C. Gerber, "Atomic force microscope," *Physical review letters,* vol. 56, no. 9, p. 930, 1986.
[114] M. Lekka, P. Laidler, D. Gil, J. Lekki, Z. Stachura, and A. Hrynkiewicz, "Elasticity of normal and cancerous human bladder cells studied by scanning force microscopy," *European Biophysics Journal,* vol. 28, no. 4, pp. 312-316, 1999.
[115] Q. Li, G. Lee, C. Ong, and C. Lim, "Probing the elasticity of breast cancer cells using AFM," in *13th international conference on biomedical engineering*, 2009: Springer, pp. 2122-2125.
[116] M. Lekka *et al.*, "Cancer cell detection in tissue sections using AFM," *Archives of biochemistry and biophysics,* vol. 518, no. 2, pp. 151-156, 2012.

[117] B. Wang, P. Lançon, C. Bienvenu, P. Vierling, C. Di Giorgio, and G. Bossis, "A general approach for the microrheology of cancer cells by atomic force microscopy," *Micron,* vol. 44, pp. 287-297, 2013.
[118] M. Li, L. Liu, X. Xiao, N. Xi, and Y. Wang, "Effects of methotrexate on the viscoelastic properties of single cells probed by atomic force microscopy," *Journal of biological physics,* vol. 42, no. 4, pp. 551-569, 2016.
[119] M. Li *et al.*, "Nanoscale characterization of dynamic cellular viscoelasticity by atomic force microscopy with varying measurement parameters," *Journal of the mechanical behavior of biomedical materials,* vol. 82, pp. 193-201, 2018.
[120] M. Li, L. Liu, X. Xiao, N. Xi, and Y. Wang, "Viscoelastic properties measurement of human lymphocytes by atomic force microscopy based on magnetic beads cell isolation," *IEEE transactions on nanobioscience,* vol. 15, no. 5, pp. 398-411, 2016.
[121] J. Helenius, C.-P. Heisenberg, H. E. Gaub, and D. J. Muller, "Single-cell force spectroscopy," *Journal of cell science,* vol. 121, no. 11, pp. 1785-1791, 2008.
[122] J. L. Maciaszek, K. Partola, J. Zhang, B. Andemariam, and G. Lykotrafitis, "Single-cell force spectroscopy as a technique to quantify human red blood cell adhesion to subendothelial laminin," *Journal of biomechanics,* vol. 47, no. 16, pp. 3855-3861, 2014.
[123] R. Omidvar, M. Tafazzoli-Shadpour, M. A. Shokrgozar, and M. Rostami, "Atomic force microscope-based single cell force spectroscopy of breast cancer cell lines: an approach for evaluating cellular invasion," *Journal of biomechanics,* vol. 47, no. 13, pp. 3373-3379, 2014.
[124] A. Moreno-Cencerrado, J. Iturri, I. Pecorari, M. DM Vivanco, O. Sbaizero, and J. L. Toca-Herrera, "Investigating cell-substrate and cell–cell interactions by means of single-cell-probe force spectroscopy," *Microscopy research and technique,* vol. 80, no. 1, pp. 124-130, 2017.
[125] M. Li, L.-q. Liu, N. Xi, and Y.-c. Wang, "Nanoscale monitoring of drug actions on cell membrane using atomic force microscopy," *Acta Pharmacologica Sinica,* vol. 36, no. 7, p. 769, 2015.
[126] D. He, "Effect of Radiation on the Morphology of Lithium-ion Battery Cathodes," The Ohio State University, 2014.
[127] H.-J. Butt and M. Jaschke, "Calculation of thermal noise in atomic force microscopy," *Nanotechnology,* vol. 6, no. 1, p. 1, 1995.
[128] J. Harding and I. Sneddon, "The elastic stresses produced by the indentation of the plane surface of a semi-infinite elastic solid by a rigid punch," in *Mathematical Proceedings of the Cambridge Philosophical Society*, 1945, vol. 41, no. 1: Cambridge University Press, pp. 16-26.
[129] E. M. Darling, S. Zauscher, and F. Guilak, "Viscoelastic properties of zonal articular chondrocytes measured by atomic force microscopy,"

*Osteoarthritis and Cartilage,* vol. 14, no. 6, pp. 571-579, Jun 2006, doi: 10.1016/j.joca.2005.12.003.

[130] E. M. Darling, M. Topel, S. Zauscher, T. P. Vail, and F. Guilak, "Viscoelastic properties of human mesenchymally-derived stem cells and primary osteoblasts, chondrocytes, and adipocytes," *Journal of Biomechanics,* vol. 41, no. 2, pp. 454-464, 2008, doi: 10.1016/j.jbiomech.2007.06.019.

[131] N. Nijenhuis, X. Zhao, A. Carisey, C. Ballestrem, and B. Derby, "Combining AFM and Acoustic Probes to Reveal Changes in the Elastic Stiffness Tensor of Living Cells," *Biophysical Journal,* vol. 107, no. 7, pp. 1502-1512, 2014/10/07/ 2014, doi: 10.1016/j.bpj.2014.07.073.

[132] W. R. Trickey, G. M. Lee, and F. Guilak, "Viscoelastic properties of chondrocytes from normal and osteoarthritic human cartilage," *Journal of Orthopaedic Research,* vol. 18, no. 6, pp. 891-898, Nov 2000, doi: 10.1002/jor.1100180607.

[133] W. R. Trickey, T. P. Vail, and F. Guilak, "The role of the cytoskeleton in the viscoelastic properties of human articular chondrocytes," *Journal of Orthopaedic Research,* vol. 22, no. 1, pp. 131-139, Jan 2004, doi: 10.1016/s0736-0266(03)00150-5.

[134] W. P. Duan *et al.*, "Normal age-related viscoelastic properties of chondrons and chondrocytes isolated from rabbit knee," *Chinese Medical Journal,* vol. 125, no. 14, pp. 2574-2581, Jul 2012, doi: 10.3760/cma.j.issn.0366-6999.2012.14.032.

[135] J. Chen, D. L. Bader, D. A. Lee, and M. M. Knight, "Finite element modeling of cell deformation when chondrocyte seeded agarose is subjected to compression.," *Proceedings of the 8th International Conference on Cell and Stem Cell Engineering (ICCE) IFMBE Proceedings,* vol. 30, pp. 17–20, 2011.

[136] J. Y. Sheng, C. Mo, G. Y. Li, H. C. Zhao, Y. P. Cao, and X. Q. Feng, "AFM-based indentation method for measuring the relaxation property of living cells," *Journal of Biomechanics,* vol. 122, Jun 2021, Art no. 110444, doi: 10.1016/j.jbiomech.2021.110444.

[137] J. Schindelin *et al.*, "Fiji: an open-source platform for biological-image analysis," *Nature Methods,* vol. 9, no. 7, pp. 676-682, 2012/07/01 2012, doi: 10.1038/nmeth.2019.

[138] D. E. Ingber, "Tensegrity I. Cell structure and hierarchical systems biology," (in eng), *J Cell Sci,* vol. 116, no. Pt 7, pp. 1157-73, Apr 1 2003, doi: 10.1242/jcs.00359.

[139] D. E. Ingber, "Tensegrity II. How structural networks influence cellular information processing networks," *Journal of cell science,* vol. 116, no. 8, pp. 1397-1408, 2003.

[140] J. Ferlay *et al.*, "Cancer incidence and mortality worldwide: Sources, methods and major patterns in GLOBOCAN 2012," *International Journal*

*of Cancer,* vol. 136, no. 5, pp. E359-E386, Mar 2015, doi: 10.1002/ijc.29210.

[141] H. A. Moayyer, M. Naderi, and J. A. Mohandesi, "Synthesis and Nanomechanical Properties of Polystyrene/Silica Core/Shell Particles Via Atomic Force Microscopy," *Langmuir,* vol. 37, no. 35, pp. 10602-10611, Sep 2021, doi: 10.1021/acs.langmuir.1c01918.

[142] J. Li, F. Zhang, L. L. Jiang, L. Yu, and L. X. Zhang, "Preparation of Silica@Silica Core-Shell Microspheres Using an Aqueous Two-Phase System in a Novel Microchannel Device," *Langmuir,* vol. 36, no. 2, pp. 576-584, Jan 2020, doi: 10.1021/acs.langmuir.9b03034.

[143] Y. Nakamura, Y. Iso, and T. Isobe, "Bandgap-Tuned CuInS2/ZnS Core/Shell Quantum Dots for a Luminescent Downshifting Layer in a Crystalline Silicon Solar Module," *Acs Applied Nano Materials,* vol. 3, no. 4, pp. 3417-3426, Apr 2020, doi: 10.1021/acsanm.0c00175.

[144] M. Schroffenegger *et al.*, "Polymer Topology Determines the Formation of Protein Corona on Core-Shell Nanoparticles," *Acs Nano,* vol. 14, no. 10, pp. 12708-12718, Oct 2020, doi: 10.1021/acsnano.0c02358.

[145] J. Park and P. S. Doyle, "Multifunctional Hierarchically-Assembled Hydrogel Particles with Pollen Grains via Pickering Suspension Polymerization," *Langmuir,* vol. 34, no. 48, pp. 14643-14651, Dec 2018, doi: 10.1021/acs.langmuir.8b02957.

[146] Y. L. Lai, H. Zhang, Y. Sugano, H. Xie, and P. Kallio, "Correlation of Surface Morphology and Interfacial Adhesive Behavior between Cellulose Surfaces: Quantitative Measurements in Peak-Force Mode with the Colloidal Probe Technique," *Langmuir,* vol. 35, no. 22, pp. 7312-7321, Jun 2019, doi: 10.1021/acs.langmuir.8b03503.

[147] C. H. Ockey and T. D. Allen, "Distribution of DNA or DNA synthesis in mammalian cells following inhibition with hydroxyurea and 5-fluorodeoxyuridine," *Experimental Cell Research,* vol. 93, no. 2, pp. 275-282, 1975.

[148] G. Bjursell and P. Reichard, "Effects of thymidine on deoxyribonucleoside triphosphate pools and deoxyribonucleic acid synthesis in Chinese hamster ovary cells," *Journal of Biological Chemistry,* vol. 248, no. 11, pp. 3904-3909, 1973.

[149] M. P. Stewart, J. Helenius, Y. Toyoda, S. P. Ramanathan, D. J. Muller, and A. A. Hyman, "Hydrostatic pressure and the actomyosin cortex drive mitotic cell rounding," *Nature,* vol. 469, no. 7329, pp. 226-230, 2011.

[150] D. Needham, "Possible role of cell cycle-dependent morphology, geometry, and mechanical properties in tumor cell metastasis," *Cell biophysics,* vol. 18, no. 2, pp. 99-121, 1991.

[151] Y. M. Efremov, W. H. Wang, S. D. Hardy, R. L. Geahlen, and A. Raman, "Measuring nanoscale viscoelastic parameters of cells directly from AFM force-displacement curves," *Scientific Reports,* vol. 7, May 2017, Art no. 1541, doi: 10.1038/s41598-017-01784-3.

[152] A. S. Vasiliev, S. S. Volkov, S. M. Aizikovich, and B. I. Mitrin, "Plane contact problem on indentation of a flat punch into a transversely-isotropic half-plane with functionally graded transversely-isotropic coating," *Zeitschrift Fur Angewandte Mathematik Und Physik,* vol. 68, no. 1, Feb 2017, Art no. 4, doi: 10.1007/s00033-016-0746-8.

[153] Y. P. Cao, D. C. Ma, and D. Raabe, "The use of flat punch indentation to determine the viscoelastic properties in the time and frequency domains of a soft layer bonded to a rigid substrate," *Acta Biomaterialia,* vol. 5, no. 1, pp. 240-248, Jan 2009, doi: 10.1016/j.actbio.2008.07.020.

[154] O. Brazil *et al.*, "In situ measurement of bulk modulus and yield response of glassy thin films via confined layer compression," *Journal of Materials Research,* vol. 35, no. 6, pp. 644-653, Mar 2020, doi: 10.1557/jmr.2020.42.

[155] F.-S. Quan and K. S. Kim, "Medical applications of the intrinsic mechanical properties of single cells," *Acta Biochimica et Biophysica Sinica,* vol. 48, no. 10, pp. 865-871, 2016, doi: 10.1093/abbs/gmw081.

[156] T. Fischer, A. Hayn, and C. T. Mierke, "Effect of Nuclear Stiffness on Cell Mechanics and Migration of Human Breast Cancer Cells," *Frontiers in Cell and Developmental Biology,* vol. 8, May 2020, Art no. 393, doi: 10.3389/fcell.2020.00393.

[157] O. O. Adeniba, E. A. Corbin, A. Ganguli, Y. Kim, and R. Bashir, "Simultaneous time-varying viscosity, elasticity, and mass measurements of single adherent cancer cells across cell cycle," *Scientific Reports,* vol. 10, no. 1, Jul 2020, Art no. 12803, doi: 10.1038/s41598-020-69638-z.

[158] J. Schnauß *et al.*, "Cells in Slow Motion: Apparent Undercooling Increases Glassy Behavior at Physiological Temperatures," *Advanced Materials,* p. 2101840, 2021.

[159] A. N. Ketene, E. M. Schmelz, P. C. Roberts, and M. Agah, "The effects of cancer progression on the viscoelasticity of ovarian cell cytoskeleton structures," *Nanomedicine: Nanotechnology, Biology and Medicine,* vol. 8, no. 1, pp. 93-102, 2012.

[160] G. Weder *et al.*, "Use of Force Spectroscopy to Investigate the Adhesion of Living Adherent Cells," *Langmuir,* vol. 26, no. 11, pp. 8180-8186, Jun 2010, doi: 10.1021/la904526u.

[161] J. Iturri *et al.*, "Resveratrol-Induced Temporal Variation in the Mechanical Properties of MCF-7 Breast Cancer Cells Investigated by Atomic Force Microscopy," *International Journal of Molecular Sciences,* vol. 20, no. 13, Jul 2019, Art no. 3275, doi: 10.3390/ijms20133275.

[162] M. H. Korayem and Z. Rastegar, "Experimental Characterization of MCF-10A Normal Cells Using AFM: Comparison with MCF-7 Cancer Cells," *Molecular & Cellular Biomechanics,* vol. 16, no. 2, p. 109, 2019.

[163] E. McEvoy, V. S. Deshpande, and P. McGarry, "Free energy analysis of cell spreading," *Journal of the Mechanical Behavior of Biomedical*

*Materials,* vol. 74, pp. 283-295, Oct 2017, doi: 10.1016/j.jmbbm.2017.06.006.

[164] E. McEvoy, S. S. Shishvan, V. S. Deshpande, and J. P. McGarry, "Thermodynamic Modeling of the Statistics of Cell Spreading on Ligand-Coated Elastic Substrates," *Biophysical Journal,* vol. 115, no. 12, pp. 2451-2460, Dec 2018, doi: 10.1016/j.bpj.2018.11.007.

[165] C. F. Natale, J. Lafaurie-Janvore, M. Ventre, A. Babataheri, and A. I. Barakat, "Focal adhesion clustering drives endothelial cell morphology on patterned surfaces," *Journal of the Royal Society Interface,* vol. 16, no. 158, Sep 2019, Art no. 20190263, doi: 10.1098/rsif.2019.0263.

[166] J. P. McGarry *et al.*, "Simulation of the contractile response of cells on an array of micro-posts," *Philosophical Transactions of the Royal Society a-Mathematical Physical and Engineering Sciences,* vol. 367, no. 1902, pp. 3477-3497, Sep 2009, doi: 10.1098/rsta.2009.0097.

[167] M. Z. Sun *et al.*, "Multiple membrane tethers probed by atomic force microscopy," *Biophysical Journal,* vol. 89, no. 6, pp. 4320-4329, Dec 2005, doi: 10.1529/biophysj.104.058180.

[168] P. H. Puech, K. Poole, D. Knebel, and D. J. Muller, "A new technical approach to quantify cell-cell adhesion forces by AFM," *Ultramicroscopy,* vol. 106, no. 8-9, pp. 637-644, Jun-Jul 2006, doi: 10.1016/j.ultramic.2005.08.003.

[169] B. H. Shin, B. H. Kim, S. Kim, K. Lee, Y. B. Choy, and C. Y. Heo, "Silicone breast implant modification review: overcoming capsular contracture," *Biomaterials research,* vol. 22, no. 1, pp. 1-9, 2018.

[170] B. Y. Yoo *et al.*, "Dual surface modification of PDMS-based silicone implants to suppress capsular contracture," *Acta Biomaterialia,* vol. 76, pp. 56-70, 2018.

[171] A. Armugam *et al.*, "Broad spectrum antimicrobial PDMS-based biomaterial for catheter fabrication," *Biomaterials research,* vol. 25, no. 1, pp. 1-13, 2021.

[172] J.-Y. Tinevez *et al.*, "TrackMate: An open and extensible platform for single-particle tracking," *Methods,* vol. 115, pp. 80-90, 2017.

[173] S. Deguchi, J. Hotta, S. Yokoyama, and T. S. Matsui, "Viscoelastic and optical properties of four different PDMS polymers," *Journal of Micromechanics and Microengineering,* vol. 25, no. 9, p. 097002, 2015.

[174] F. Prabowo, A. L. Wing-Keung, and H. H. Shen, "Effect of curing temperature and cross-linker to pre-polymer ratio on the viscoelastic properties of a PDMS elastomer," in *Advanced Materials Research*, 2015, vol. 1112: Trans Tech Publ, pp. 410-413.

[175] J. D. Glover, C. E. McLaughlin, M. K. McFarland, and J. T. Pham, "Extracting uncrosslinked material from low modulus sylgard 184 and the effect on mechanical properties," *Journal of Polymer Science,* vol. 58, no. 2, pp. 343-351, 2020.

[176] I. Johnston, D. McCluskey, C. Tan, and M. Tracey, "Mechanical characterization of bulk Sylgard 184 for microfluidics and microengineering," *Journal of Micromechanics and Microengineering,* vol. 24, no. 3, p. 035017, 2014.
[177] E. A. Waddell, S. Shreeves, H. Carrell, C. Perry, B. A. Reid, and J. McKee, "Surface modification of Sylgard 184 polydimethylsiloxane by 254 nm excimer radiation and characterization by contact angle goniometry, infrared spectroscopy, atomic force and scanning electron microscopy," *Applied Surface Science,* vol. 254, no. 17, pp. 5314-5318, 2008.
[178] Z. Wu, H. Yan, H. Chen, and H. Huang, "One-stage fabrication of sub-micron hydrophilic microchannels on PDMS," *Applied surface science,* vol. 255, no. 8, pp. 4702-4704, 2009.
[179] B. D. Hoffman, G. Massiera, K. M. Van Citters, and J. C. Crocker, "The consensus mechanics of cultured mammalian cells," *Proceedings of the National Academy of Sciences,* vol. 103, no. 27, pp. 10259-10264, 2006.
[180] Y. L. Dorland and S. Huveneers, "Cell–cell junctional mechanotransduction in endothelial remodeling," *Cellular and Molecular Life Sciences,* vol. 74, no. 2, pp. 279-292, 2017.
[181] F. Martino, A. R. Perestrelo, V. Vinarský, S. Pagliari, and G. Forte, "Cellular mechanotransduction: from tension to function," *Frontiers in physiology,* vol. 9, p. 824, 2018.
[182] C. Ani *et al.*, "A shear assay study of single normal/breast cancer cell deformation and detachment from poly-di-methyl-siloxane (PDMS) surfaces," *Journal of the Mechanical Behavior of Biomedical Materials,* vol. 91, pp. 76-90, 2019.
[183] M. Nikkhah, J. S. Strobl, R. De Vita, and M. Agah, "The cytoskeletal organization of breast carcinoma and fibroblast cells inside three dimensional (3-D) isotropic silicon microstructures," *Biomaterials,* vol. 31, no. 16, pp. 4552-4561, 2010.
[184] Y. Nematbakhsh, K. T. Pang, and C. T. Lim, "Correlating the viscoelasticity of breast cancer cells with their malignancy," *Convergent Science Physical Oncology,* vol. 3, no. 3, p. 034003, 2017.
[185] A. Heydarian, D. Milani, and S. M. M. Fatemi, "An investigation of the viscoelastic behavior of MCF-10A and MCF-7 cells," *Biochemical and Biophysical Research Communications,* vol. 529, no. 2, pp. 432-436, 2020.
[186] S.-Y. Tee, J. Fu, C. S. Chen, and P. A. Janmey, "Cell shape and substrate rigidity both regulate cell stiffness," *Biophysical journal,* vol. 100, no. 5, pp. L25-L27, 2011.
[187] D. G. Thalla, P. Jung, M. Bischoff, and F. Lautenschläger, "Role of extracellular vimentin in cancer-cell functionality and its influence on cell monolayer permeability changes induced by SARS-CoV-2 receptor

binding domain," *International Journal of Molecular Sciences,* vol. 22, no. 14, p. 7469, 2021.
[188] T. TruongVo *et al.*, "Microfluidic channel for characterizing normal and breast cancer cells," *Journal of Micromechanics and Microengineering,* vol. 27, no. 3, p. 035017, 2017.
[189] A. H. Kulkarni, A. Chatterjee, P. Kondaiah, and N. Gundiah, "TGF-beta induces changes in breast cancer cell deformability," *Physical Biology,* vol. 15, no. 6, Nov 2018, Art no. 065005, doi: 10.1088/1478-3975/aac3ba.
[190] O. Jonas, C. T. Mierke, and J. A. Käs, "Invasive cancer cell lines exhibit biomechanical properties that are distinct from their noninvasive counterparts," *Soft Matter,* vol. 7, no. 24, pp. 11488-11495, 2011.
[191] C. Malinverno *et al.*, "Endocytic reawakening of motility in jammed epithelia," *Nature materials,* vol. 16, no. 5, pp. 587-596, 2017.
[192] M. Popielarski, H. Ponamarczuk, M. Stasiak, C. Watała, and M. Świątkowska, "Modifications of disulfide bonds in breast cancer cell migration and invasiveness," *American journal of cancer research,* vol. 9, no. 8, p. 1554, 2019.
[193] H. Bae, B. Kim, H. Lee, S. Lee, H.-S. Kang, and S. J. Kim, "Epigenetically regulated Fibronectin leucine rich transmembrane protein 2 (FLRT2) shows tumor suppressor activity in breast cancer cells," *Scientific reports,* vol. 7, no. 1, pp. 1-11, 2017.
[194] H. Kobayashi, K. C. Boelte, and P. C. Lin, "Endothelial cell adhesion molecules and cancer progression," *Current medicinal chemistry,* vol. 14, no. 4, pp. 377-386, 2007.
[195] M. C. Moh and S. Shen, "The roles of cell adhesion molecules in tumor suppression and cell migration: a new paradox," *Cell adhesion & migration,* vol. 3, no. 4, pp. 334-336, 2009.
[196] A. Calzado-Martin, M. Encinar, J. Tamayo, M. Calleja, and A. S. Paulo, "Effect of Actin Organization on the Stiffness of Living Breast Cancer Cells Revealed by Peak-Force Modulation Atomic Force Microscopy," *Acs Nano,* vol. 10, no. 3, pp. 3365-3374, Mar 2016, doi: 10.1021/acsnano.5b07162.
[197] T. Kwon, S. Gunasekaran, and K. Eom, "Atomic force microscopy-based cancer diagnosis by detecting cancer-specific biomolecules and cells," *Biochimica et Biophysica Acta (BBA)-Reviews on Cancer,* vol. 1871, no. 2, pp. 367-378, 2019.
[198] A. Ansardamavandi, M. Tafazzoli-Shadpour, R. Omidvar, and I. Jahanzad, "Quantification of effects of cancer on elastic properties of breast tissue by atomic force microscopy," *Journal of the mechanical behavior of biomedical materials,* vol. 60, pp. 234-242, 2016.
[199] M. Tamura, J. Gu, K. Matsumoto, S.-i. Aota, R. Parsons, and K. M. Yamada, "Inhibition of cell migration, spreading, and focal adhesions by

tumor suppressor PTEN," *Science,* vol. 280, no. 5369, pp. 1614-1617, 1998.
[200] J. R. Lange and B. Fabry, "Cell and tissue mechanics in cell migration," *Experimental cell research,* vol. 319, no. 16, pp. 2418-2423, 2013.
[201] A. Pathak and S. Kumar, "Independent regulation of tumor cell migration by matrix stiffness and confinement," *Proceedings of the National Academy of Sciences,* vol. 109, no. 26, pp. 10334-10339, 2012.
[202] C. Campbell and S. Gill, "An analytical model for the flat punch indentation size effect," *International Journal of Solids and Structures,* vol. 171, pp. 81-91, 2019.
[203] H. Yu, S. Sanday, and B. Rath, "The effect of substrate on the elastic properties of films determined by the indentation test—Axisymmetric Boussinesq problem," *Journal of the Mechanics and Physics of Solids,* vol. 38, no. 6, pp. 745-764, 1990.
[204] M.-G. Zhang, J. Chen, X.-Q. Feng, and Y. Cao, "On the applicability of Sneddon's solution for interpreting the indentation of nonlinear elastic biopolymers," *Journal of Applied Mechanics,* vol. 81, no. 9, 2014.
[205] J. Chen and S. Bull, "On the factors affecting the critical indenter penetration for measurement of coating hardness," *Vacuum,* vol. 83, no. 6, pp. 911-920, 2009.
[206] P. Vettiger *et al.*, "The “Millipede”—More than thousand tips for future AFM storage," *IBM Journal of Research and Development,* vol. 44, no. 3, pp. 323-340, 2000.
[207] C. Rotsch and M. Radmacher, "Drug-induced changes of cytoskeletal structure and mechanics in fibroblasts: an atomic force microscopy study," *Biophysical journal,* vol. 78, no. 1, pp. 520-535, 2000.
[208] H. Zhang, L. Xiao, Q. Li, X. Qi, and A. Zhou, "Microfluidic chip for non-invasive analysis of tumor cells interaction with anti-cancer drug doxorubicin by AFM and Raman spectroscopy," *Biomicrofluidics,* vol. 12, no. 2, p. 024119, 2018.
[209] X. Liang, S. Liu, X. Wang, D. Xia, and Q. Li, "Alteration of nanomechanical properties of pancreatic cancer cells through anticancer drug treatment revealed by atomic force microscopy," *Beilstein journal of nanotechnology,* vol. 12, no. 1, pp. 1372-1379, 2021.
[210] J. Sitterberg, A. Özcetin, C. Ehrhardt, and U. Bakowsky, "Utilising atomic force microscopy for the characterisation of nanoscale drug delivery systems," *European Journal of Pharmaceutics and Biopharmaceutics,* vol. 74, no. 1, pp. 2-13, 2010.
[211] J. M. Edwardson and R. M. Henderson, "Atomic force microscopy and drug discovery," *Drug discovery today,* vol. 9, no. 2, pp. 64-71, 2004.
[212] C. Lamprecht, P. Hinterdorfer, and A. Ebner, "Applications of biosensing atomic force microscopy in monitoring drug and nanoparticle delivery," *Expert Opinion on Drug Delivery,* vol. 11, no. 8, pp. 1237-1253, 2014.

[213] A. Berquand, M.-P. Mingeot-Leclercq, and Y. Dufrene, "Real-time imaging of drug–membrane interactions by atomic force microscopy," *Biochimica et Biophysica Acta (BBA)-Biomembranes,* vol. 1664, no. 2, pp. 198-205, 2004.

# Appendix

## Scanning electron microscope images of the cantilever

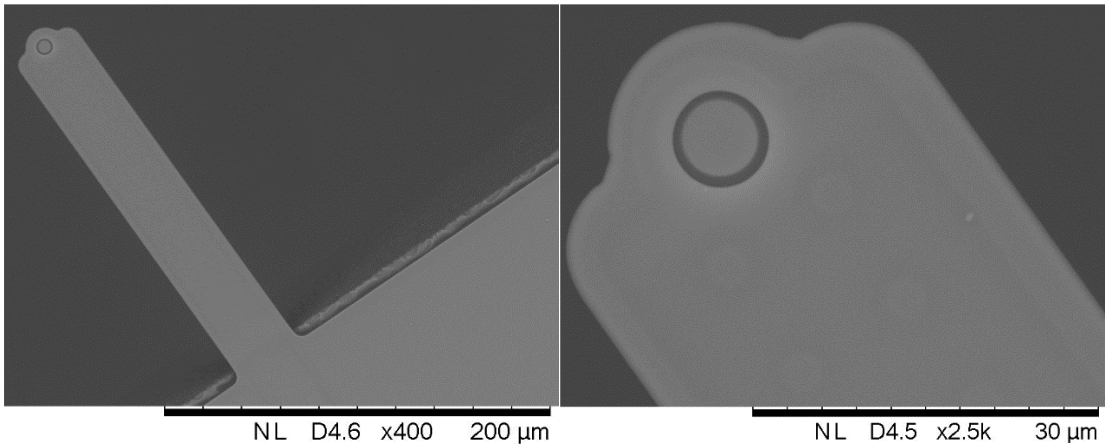


Figure S 1. The scanning electron microscope image of the cantilever for FluidFM used in this study.

## Detachment of distinct focal adhesion containing structures.

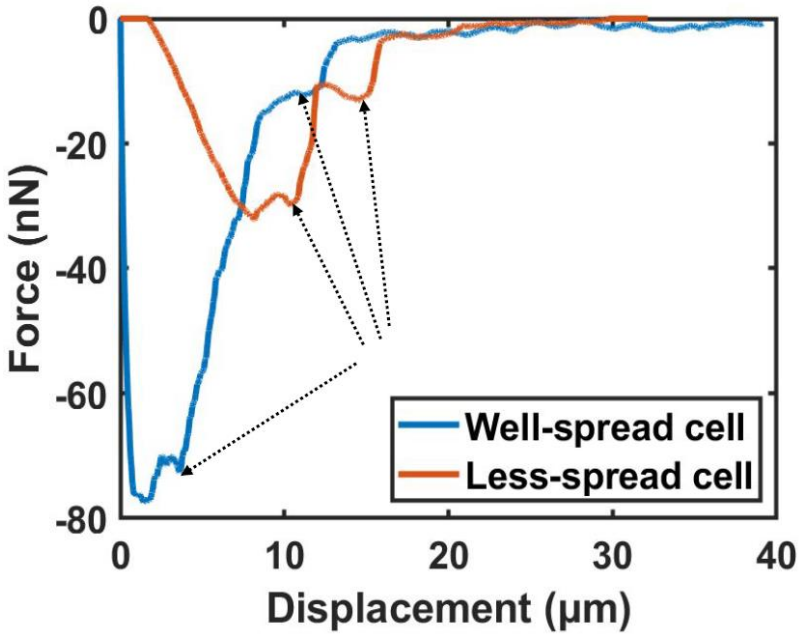


Figure S 2. Representative images of multiple events on the detachment curves for both less-spread cell and well-spread cell, which can be related to detachment of distinct focal adhesion containing structures.

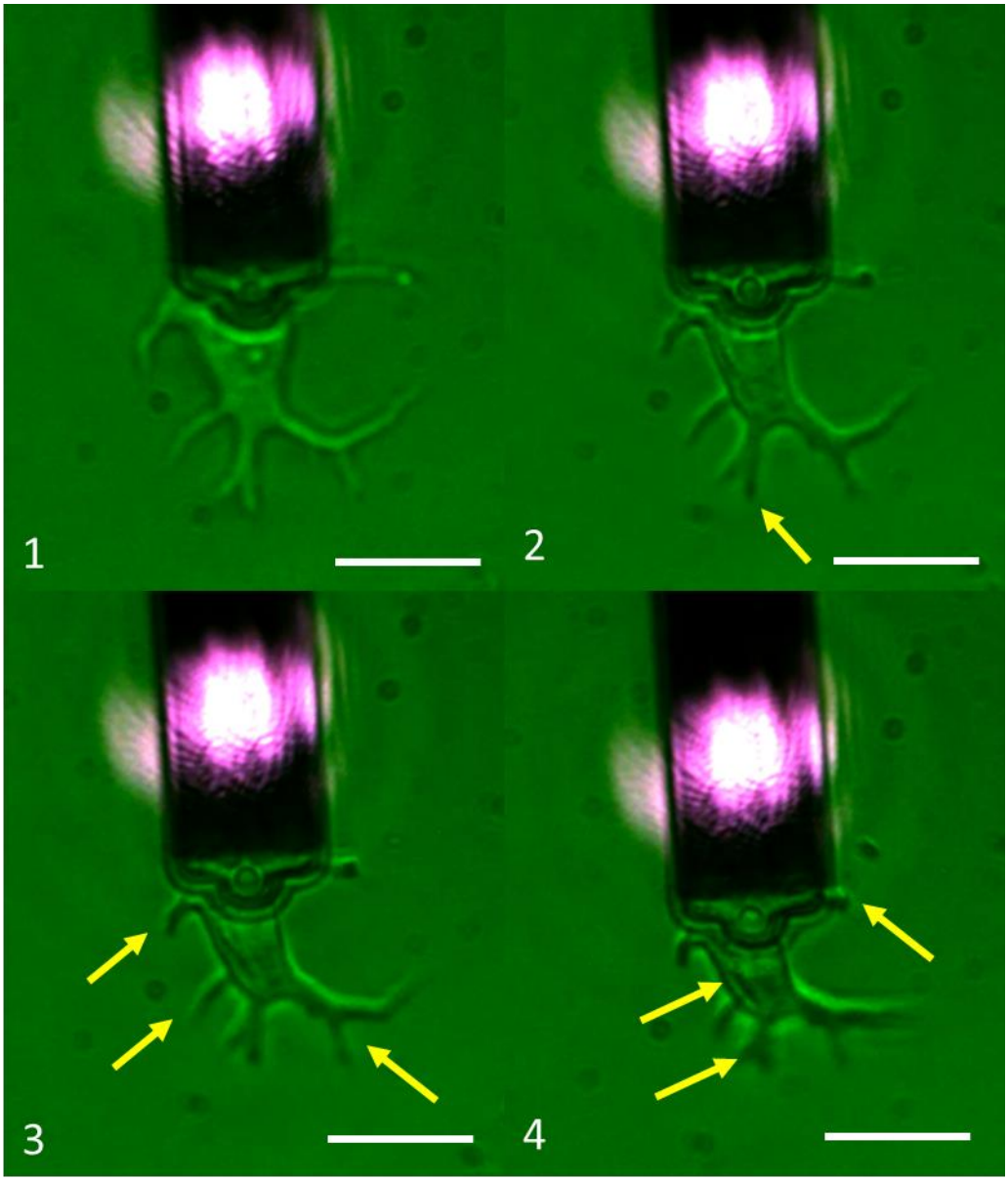


Figure S 3. Representative images of detachment of distinct focal adhesion containing structures. 1, Before detachment. 2, Detachment of one pseudopodium. 3, Detachments of more pseudopodia. 4, Detachments of the rest pseudopodia and the main body of the cell. The scale bars are 35 μm.

## 3D confocal images of MCF-7

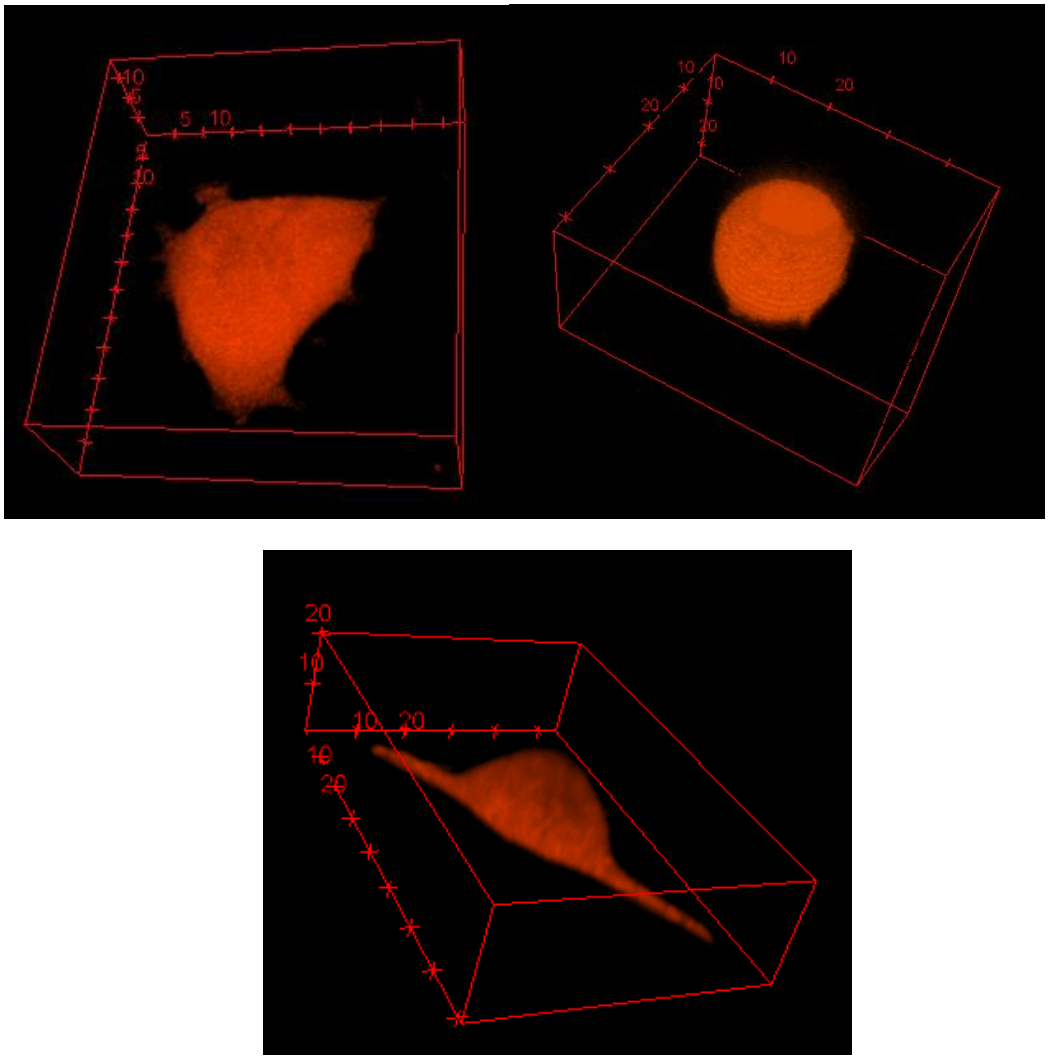


Figure S 4. Typical morphologies of MCF-7 cells on tissue culture-treated polystyrene. Spread shape (top left), Spherical shape (top right), spindle-like shape (bottom). The unit of the number on the scale box is μm.

## Problems in scratch test for cell migration

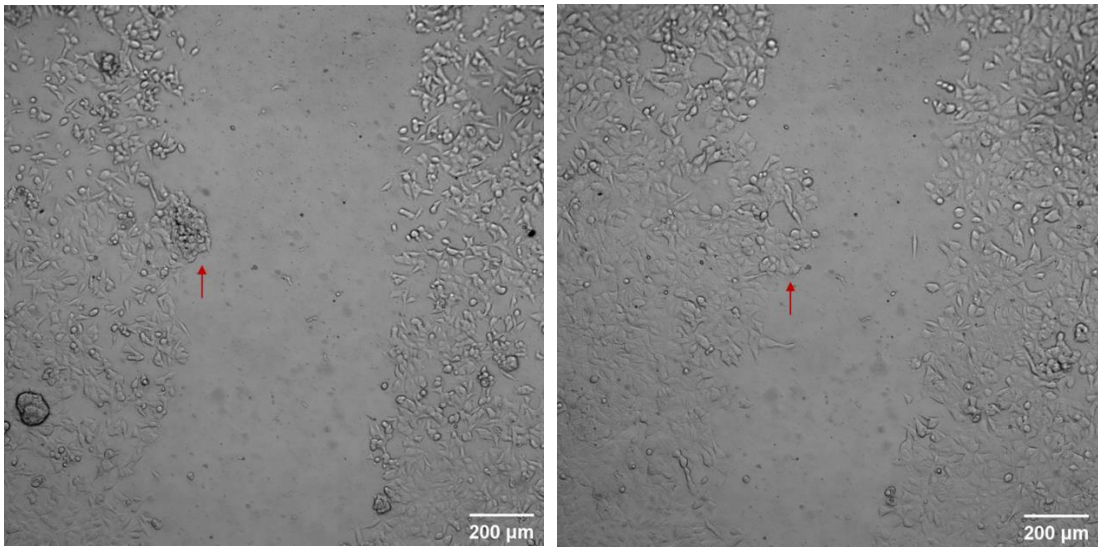


Figure S 5. Cell scratch and aggregation: the left-hand image shows the cell scratch at 0 hours, and on the right is the cell scratch at 3 hours, with red arrows indicating cell aggregates.

The edge of the cell scratch is uneven and the cell aggregates have an impact on the recovery rate; it is clear that after 3 hours the cell aggregate has spread, resulting in a greater recovery of the scratch than elsewhere.

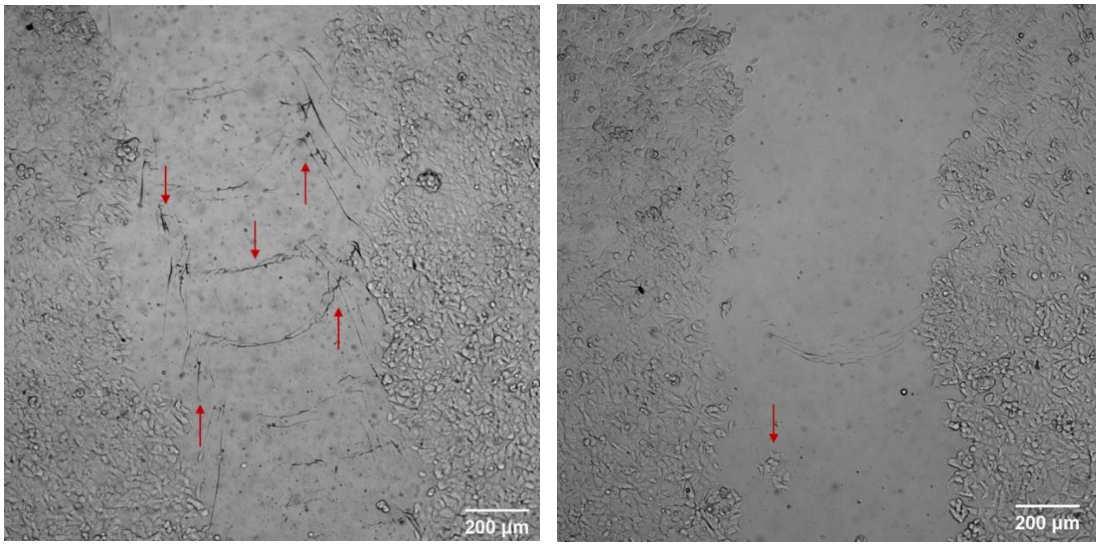


Figure S 6. Problems with manual cell scratches on soft PDMS surfaces.

The red arrows in the left-hand image indicate damage to the surface and show that a strong scratch can damage the PDMS surface, causing inconsistencies in the surface morphology and structure and affecting the experimental results. The right-hand image shows that less vigorous scratching can leave cells in the scratch, which also affects the results; the red arrow indicates remaining cells.

## Mesh sensitivity validation

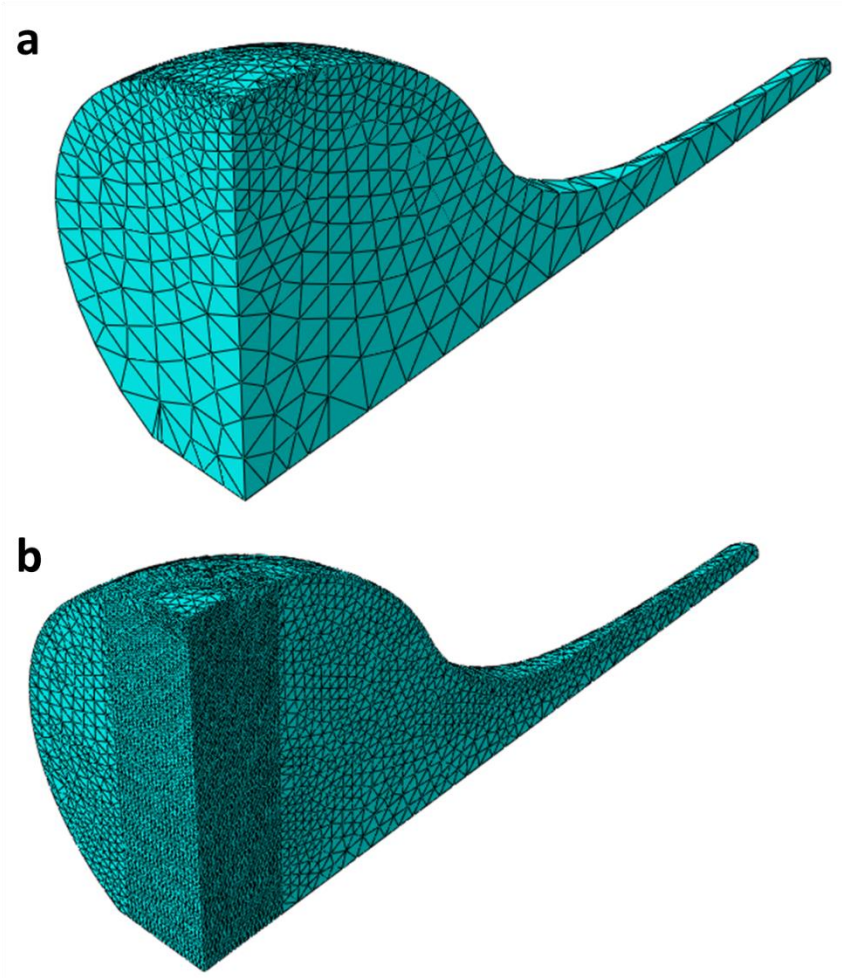


Figure S 7. Models with (a) coarse mesh of 9175 elements and (b) fine mesh of 88551 elements was used for mesh sensitivity verification. More results are shown in Figure S 8

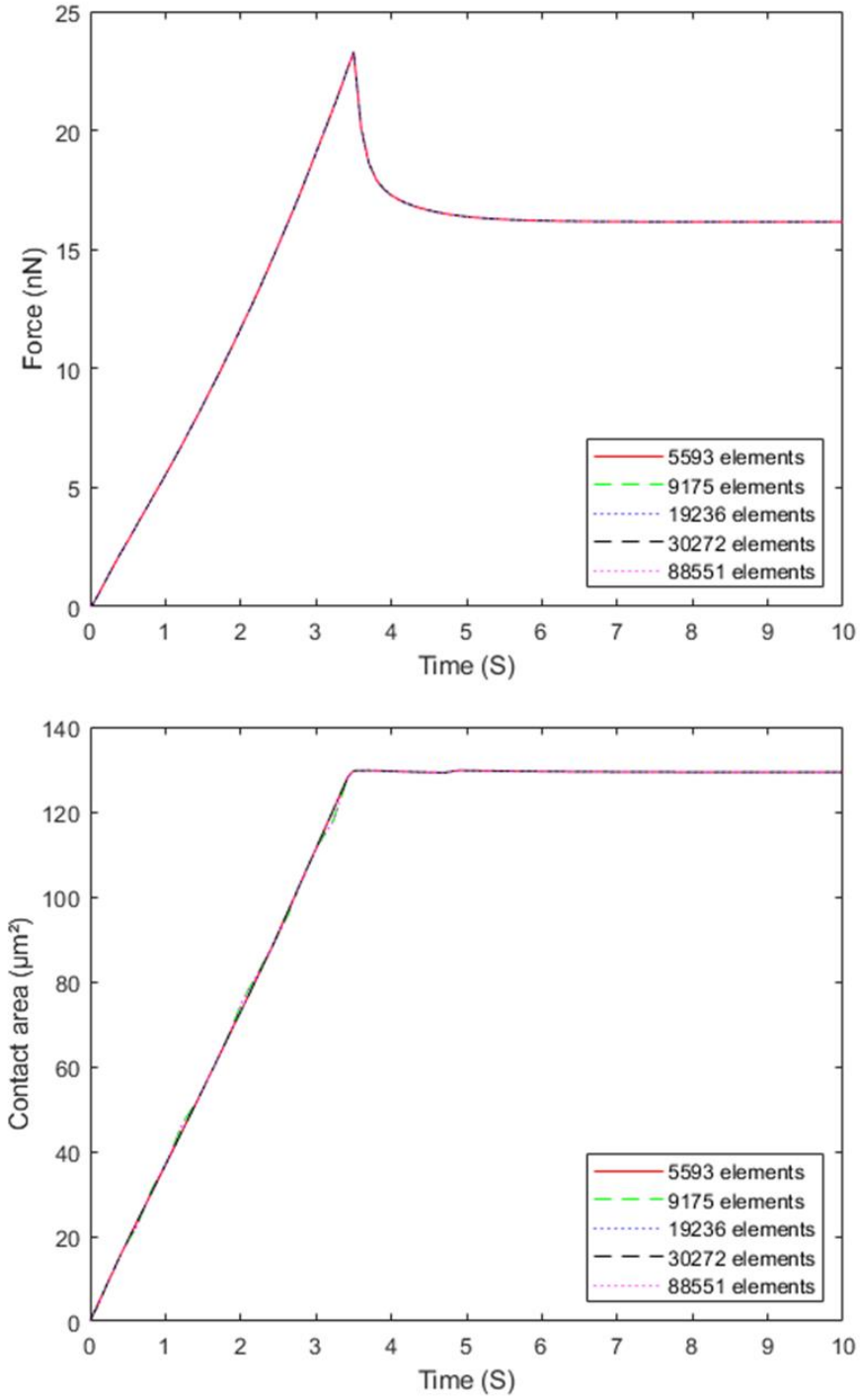


Figure S 8. Simulation results of different mesh models for indenter force and contact area. The numbers in the legend indicate the number of elements in the model part.

Results shown in Figure S 8 validate that the model has good mesh sensitivity.

## Curve fitting sampling validation

In FluidFM experiments, when the relaxation exceeds 5s, encounter large vibrations of the cell are encountered (see below). Therefore, in this study, 3s relaxation was choose consistently for the curve fitting to determine the viscoelastic properties.

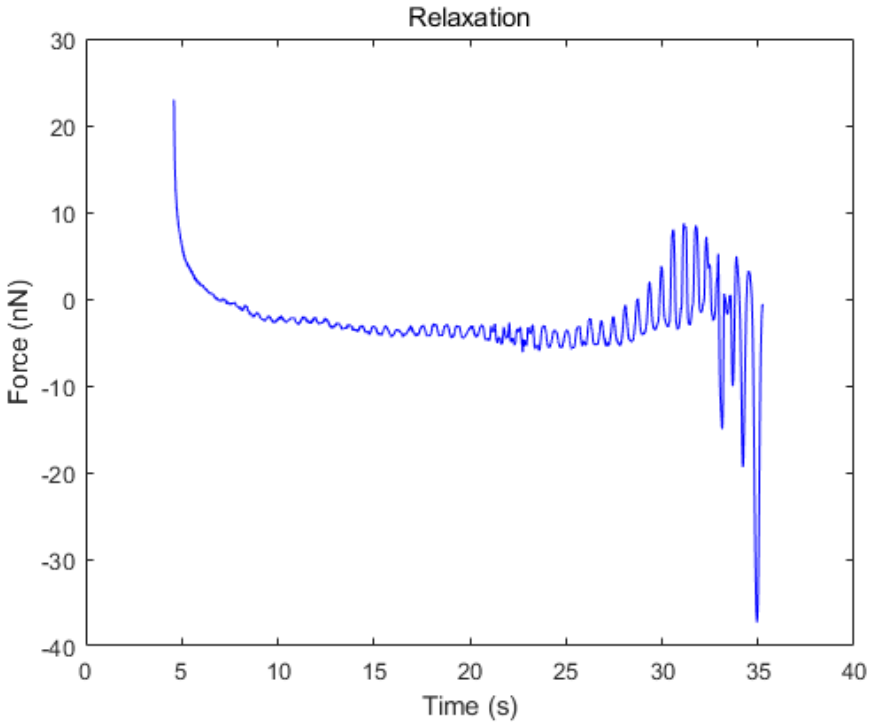


Figure S 9. Vibration of cantilever during longer stress relaxation period.

Furthermore, a finite element simulation was run, using the viscoelastic properties presented in Table 1, to examine the effect of duration of stress relaxation on the determination of the viscoelastic properties such as time constants. For example, the time constants determined have been presented by using the first 3s relaxation and the whole 30s period (fully relaxed) in Figure S 10. It can be seen that the difference is very small (<5%).

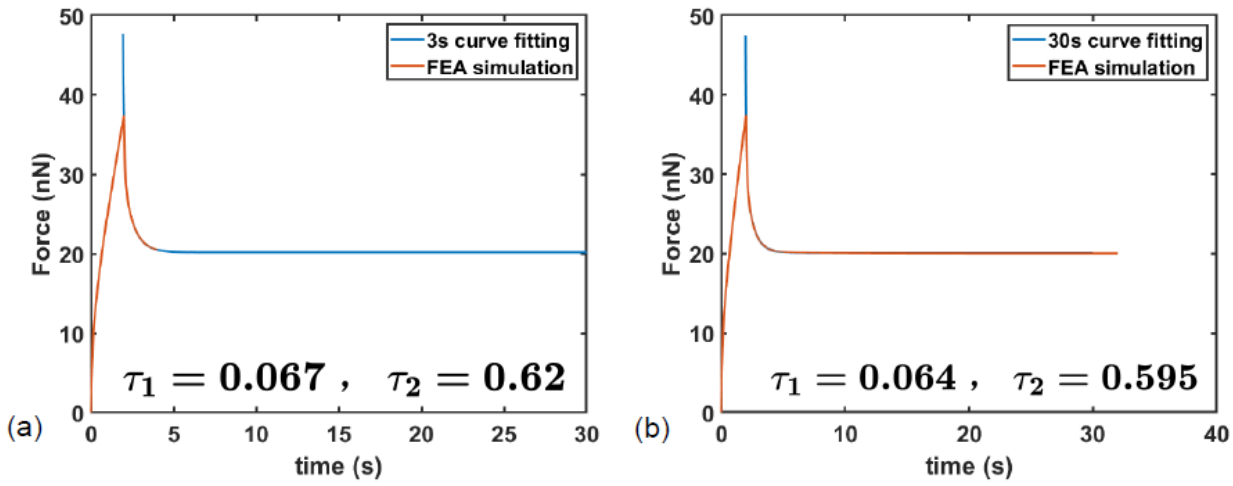


Figure S 10. The curve fitting of the first 3s relaxation (a) and the whole 30s period (fully relaxed; b) on the stress relaxation curve of the cell determined by FE simulations.